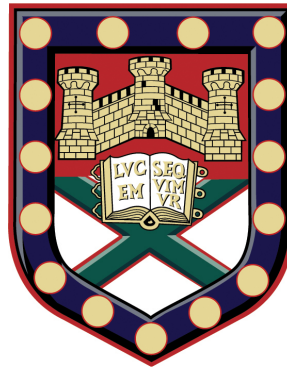


Electromechanical Properties Of Atomically Thin Materials



Alexander James Pearce

School of Physics

University of Exeter

A thesis submitted for the degree of

Doctor of Philosophy in Physics

June 2014

Electromechanical Properties Of Atomically Thin Material

Submitted by Alexander James Pearce to the University of Exeter as a thesis for the
degree of Doctor of Philosophy in Physics.

June 2014

This thesis is available for library use on the understanding that it is copyright material and that no
quotation from the thesis may be published without proper acknowledgement.

I certify that all material in this thesis which is not my own work has been identified and
that no material has previously submitted and approved for the award of a degree by this or any
other university.

Alexander James Pearce

June 2014

Abstract

We discuss the effect of elastic deformations on the electronic properties of atomically thin materials, with a focus on bilayer graphene and MoS₂ membranes. In these materials distortions of the lattice translate into fictitious gauge fields in the electronic Dirac Hamiltonian that are explicitly derived here for arbitrary elastic deformations, including in-plane as well as flexural (out-of-plane) distortions. We consider bilayer graphene, where a constant fictitious gauge field causes a dramatic reconstruction of the low energy trigonally warped electronic spectrum inducing topological transitions in the Fermi surface. We then present results of ballistic transport in trigonally warped bilayer graphene with and without strain, with particular focus on noise and the Fano factor. With the inclusion of trigonal warping the Fano factor at the Dirac point is still $F = 1/3$, but the range of energies which show pseudo diffusive transport increases by orders of magnitude compared to the results stemming out of a parabolic spectrum and the applied strain acts to increase this energy range further. We also consider arbitrary deformations of another two-dimensional membrane, MoS₂. Distortions of this lattice also lead to a fictitious gauge field arising within the Dirac Hamiltonian, but with a distinct structure than seen in graphene. We present the full form of the fictitious gauge fields that arise in MoS₂. Using the fictitious gauge fields we study the coupling between electronic and mechanical degrees of freedom, in particular the coupling between electrons and excited vibrational modes, or vibrons. To understand whether these effects may have a strong influence on electronic transport in MoS₂ we calculate the dimensionless electron-vibron coupling constant for all vibron modes relevant for electronic transport. We find that electron-vibron coupling constant is highly sample specific and that the longitudinal stretching mode is the vibron with the dominant coupling. This however reaches maximum values which are lower than those observed in carbon nanostructures.

Contents

1	Introduction	8
2	Electronic Properties of Graphene	16
2.1	Introduction	16
2.2	Electronic Properties of Monolayer Graphene	20
2.2.1	Massless Dirac Fermions	25
2.2.2	Trigonal Warping	27
2.3	Electronic Properties of Bilayer Graphene	28
2.3.1	Band Gap	32
2.3.2	Effective Low-Energy Theory	33
2.3.3	Massive Dirac Fermions	34
2.3.4	Trigonal Warping	35
2.4	Conclusion	38
3	Electromechanical Properties of Graphene	44
3.1	Introduction	44
3.2	Continuum Elasticity Theory for Two Dimensional Membranes	45
3.3	Fictitious Gauge Fields in Monolayer Graphene	50
3.3.1	Deformation Potential	52
3.3.2	Monolayer Graphene Band Structure With Deformations	53
3.3.3	Pseudo Magnetic Fields	54
3.4	Fictitious Gauge Fields in Bilayer Graphene	54
3.5	Bilayer Graphene Band Structure With Deformations	60

3.6	Conclusion	65
4	Conductance and Shot Noise In Strained Bilayer Graphene	71
4.1	Introduction	71
4.2	Model of Bilayer Graphene	73
4.3	Uniaxial Strain in Bilayer Graphene	75
4.4	Scattering Matrix	77
4.5	Results and discussion	81
4.6	Conclusion	87
5	Electron-Vibron Coupling in MoS₂	93
5.1	Electronic Structure of MoS ₂	95
5.2	Vibrational Properties of MoS ₂	102
5.3	Fictitious Gauge Fields In MoS ₂	105
5.4	Electron-Vibron Coupling Constants	107
5.5	Conclusion	114
6	Conclusions	121
6.1	Further work	122
7	Appendix A: Full Form of Fictitious Gauges fields in MoS₂ to Second Order	124

List of Figures

1.1	Examples of graphene and MoS ₂ suspended devices.	10
2.1	Examples of graphene devices and their conductivity and quantum Hall characteristics.	18
2.2	Monolayer Graphene crystal lattice and 1st Brillouin zone.	21
2.3	Monolayer Graphene Band Structure.	22
2.4	Pseudo-Spin Winding In Both Monolayer And Bilayer Graphene.	27
2.5	Trigonal Warping in Monolayer Graphene.	28
2.6	Bilayer graphene crystal lattice.	29
2.7	Bilayer graphene Band Structure.	30
2.8	Gapped Bilayer Graphene Band Structure.	32
2.9	Trigonal Warped Bilayer Graphene Band Structure.	36
3.1	Scanning tunnelling microscopy measurements on graphene nano bubbles.	55
3.2	Schematic description of the effect of deformations on bond lengths	58
3.3	Electronic band structure in the wavevector space and equipotential lines for different values of strain	62
3.4	The electronic DOS and Fermi surface at a fixed electron density for different values of strain	64
4.1	Electronic spectrum of trigonally warped bilayer graphene	74
4.2	Electronic spectrum of trigonally warped bilayer graphene under uniaxial strain along the x -axis	75
4.3	Schematic of the bilayer graphene device setup	78

4.4	Transmission probability of bilayer graphene as a function of the transverse wavevector and energy in both the presence and absence of strain	81
4.5	Conductivity and Fano factor as a function of energy for strained and unstrained trigonally warped bilayer graphene	84
5.1	The atomic structure of perfect MoS ₂	97
5.2	Electronic Dispersion of MoS ₂	99
5.3	Electronic Dispersion of MoS ₂ with Spin Orbit Coupling.	101
5.4	The vibrational eigenmodes of MoS ₂	103
5.5	An example of Coulomb diamonds and a Diagram of the setup of a quantum dot device.	108
5.6	Diagram of vibronic oscillator states showing the shift of equilibrium coordinate of the vibronic wave function and experimental data showing Frank-Condon regime with vibrational sidebands.	109
5.7	Setup of MoS ₂ device.	111

Acknowledgements

There are a huge number of people I have to thank in helping me complete my PhD studies and also in making my time in Exeter some of the most enjoyable of my life.

Firstly I have to offer my thanks and gratitude to my supervisor Eros Mariani for introducing me to this fascinating subject and being patient with me over the years, giving invaluable advice and guidance throughout my studies and for essentially teaching me how to do physics.

My fellow PhD students on the 3rd floor who have kept me sane while at work with conversations both related and unrelated to physics Claire Woollacott, Charles Downing, Lachlan Marncham, Tom Sturges and Chinna Devarapu.

Also my excellent house mates across several flats over the years Dave Hudson, Thomas Haworth, Tom Bointon, Adam Snitch, and Thomas Sowerby who have provided me with innumerable great memories.

I also have to thank my other great friends in Exeter who have made my time here so enjoyable while I can't possibly name you all here I must particularly mention this consistent members of the monday night pub trip Alex Pettitt, Katrina Alaimo, Hannah Wakeford and David Amundsen amongst others.

Finally, but clearly not last, I have to thank my parents for their love and support throughout the years, it's clear to me that without them none of this would have been possible.

Thank you to all of you.

Alexander Pearce

Exeter, U.K.

13th June 2014

1

Introduction

The physics of two-dimensional electron systems is a mature subject with a history that stretches back to the 1960's. The first two-dimensional electron systems were realised in metal-oxide-semiconductor field effect transistors (MOSFET's). By creating an inversion layer in these structures the z -direction is frozen out by a finite sized quantisation gap. This creates a two-dimensional plane of conducting electrons within a larger three-dimensional heterostructure and opens a window into new physics made possible by the reduced dimensionality, most famously the quantum Hall effect which lead to two Nobel prizes. These systems represented huge leaps in our understanding of nature and paved the way for new technologies which now lie at the heart of modern microelectronics.

In recent years it has become possible to experimentally realise free standing two-dimensional crystal structures. These materials are two-dimensional membranes only one atom thick, the thinnest possible material. In 2004 Andrei Geim and Konstantin Novoselov were able to take bulk graphite, a material comprised of layers which are weakly bonded together via van der Waals

forces and for the first time were able to isolate a monolayer of this structure which is known as graphene.[1] This crystalline membrane has distinct properties compared to two-dimensional systems found in MOSFET's due to the interplay between electronic, mechanical, chemical and thermal characteristics. The coupling between the electronic and mechanical properties of these systems and its effect on electronic transport will be the focus of this thesis.

Graphene is a crystalline allotrope of carbon comprised of a monoatomic layer of atoms arranged in a honeycomb lattice. This lattice structure gives rise to a gapless electronic band structure. Moreover, the low energy electronic dispersion is linear and supports charge carriers which behave as massless Dirac fermions, a property that gives graphene several of its exceptional electronic characteristics. These Dirac fermions are chiral and possess strikingly different properties to Schrödinger electrons, such as a nontrivial Berry phase.[2] The particle's chiral nature underpins graphene's transport properties in a wide variety of regimes such as the Klein tunnelling through potential barriers[3, 4], a minimal conductivity at zero carrier density[5], anti weak localisation,[6, 7] the anomalous integer quantum Hall effect[8, 9] and the ability for ballistic transport over micrometer scales even at room temperatures.[10, 11]

The properties of graphene are dominated by its two-dimensional nature. Due to being atomically thin it is nearly transparent with only 2% absorption of visible light incident upon a graphene sheet.[12] Its chemical properties are also governed by this two-dimensional nature as graphene offers an exposed surface allowing for dramatic modifications of its electronic properties by chemical functionalisation.[13, 14]

The carbon-carbon bonds which make up graphene's honeycomb lattice are incredibly strong and make graphene the strongest known material with a Young's modulus of 1TPa.[15] While graphene is very stiff it is also highly flexible, a property that makes it an ideal material for mechanical devices such as nanoscale atomically thin resonators. Mechanical resonators consist of a beam of material that resonates in response to an externally applied force and have use in applications such as mass detectors and force sensors.[16] Graphene resonators have been fabricated with Q-factors reaching $\sim 10^5$ and their atomic thinness allows for the exploration of non-linearities in the dynamics and damping of suspended devices.[17] Altogether these properties have led to graphene receiving incredible levels of interest from the scientific community for studies of fundamental science and a wide range of potential applications in areas as diverse as flexible electronics and biomedical sensing.

One way to increase the electronic mobility of graphene is by reducing interactions with the substrate by creating suspended devices.[18, 16] This process involves removing the substrate in-between the electrical contacts allowing the graphene to hang freely in this portion of space. A scanning electron microscope image of such devices is shown in Fig. 1.1.a and Fig. 1.1.b. This technique has led to samples with the highest reported field effect mobilities and also brings to the fore the membrane properties of the two-dimensional crystal. Indeed, a close inspection of Fig 1.1.a will show the presence of wrinkles and ripples in the graphene, this is only one example of the deformations of the lattice which can form in suspended devices.

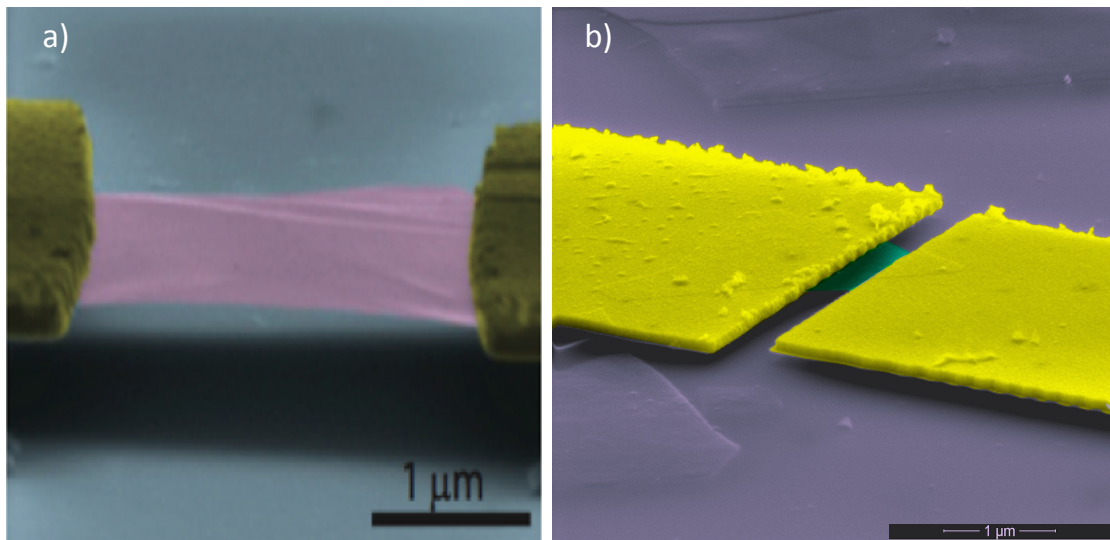


Figure 1.1: Examples of graphene and MoS₂ suspended devices. Panel a) shows a scanning electron microscope image of a graphene suspended device while panel b) shows a scanning electron microscope image of a suspended MoS₂ device. Both images have used false colours to highlight the contacts and the sample. (The images are provided courtesy of D. Hudson)

The effect of ripples and deformations of the membrane extends well beyond the mechanical properties of graphene. Indeed, the coupling of mechanical and electronic degrees of freedom have been observed to have a strong influence on the electronic transport in many other nanostructures such as molecular junctions[19] and carbon nanotubes.[20] In graphene it has been understood that the coupling between electrical degrees of freedom and smooth deformations of the membrane leads to a fictitious gauge field in the electronic Hamiltonian which is analogous to an electromagnetic vector potential.[21] This occurs due to strains and ripples creating modifications of the lengths of the carbon-carbon bonds which make up the honeycomb lattice leading to direct

effects on the electronic structure and transport properties of graphene. The electromechanical properties of graphene are crucial to the understanding of electronic transport in suspended samples where the membrane nature of the crystal is prominent. There already has been much interest in using strain in graphene as a way of controlling its electronic properties,[22, 23, 24, 25] but there are still many open questions particularly in the area of multilayer graphene flakes and other atomically thin materials beyond graphene. These questions will be the main focus of the present thesis.

While graphene is the best known two-dimensional material, it is not the only one to exist. Several other two-dimensional crystals have been isolated and they all have honeycomb lattice structures in common with graphene. One of the first of these materials to be used in electronic devices was hexagonal boron nitride, a band insulator with a large band gap of 5.2eV.[26] The most common use of hexagonal boron nitride is as a substrate or for encapsulating graphene, which has been shown to screen out charge traps and impurities in the substrate giving a route to high quality devices. In recent years the transition metal dichalcogenides have gained prominence and received much interest. Examples of this family of materials are MoS_2 , WS_2 and NbSe_2 . These two-dimensional materials in contrast to graphene are semiconductors with band gaps which are often in the visible energy range making them highly attractive for optoelectronic applications.[27, 28] Their semiconducting properties make them highly suited for low power transistors with on/off ratios which vastly improve on any device currently reported in graphene although these systems at present are always very disordered and show rather low electron mobilities.[29] Considering all these materials together we see that there is a large family of two-dimensional crystals with a wide range of electronic structures offering a variety of ways in which the physics of membranes and soft matter physics could manifest itself in a range of different electronic systems.

In this thesis we seek to address the electromechanical properties and the role of fictitious gauge fields in novel two-dimensional materials. We will focus on bilayer graphene and on transition metal dichalcogenides. We will present the full form of the fictitious gauge fields due to any arbitrary elastic deformation in these materials and then use this very general formalism to tackle more specific problems. Bilayer graphene shows a complicated electronic spectrum at low energies due to an effect known as trigonal warping and we will show that strain can completely reconstruct this spectrum with dramatic consequences on ballistic transport in high quality suspended devices. We will also look at vibrational effects in suspended MoS_2 , focusing on a trans-

port regime dominated by localised states and resonant tunnelling where electron-vibron coupling can be important.

This thesis will be organised as follows: chapter two will consist of an introduction to the electronic properties of graphene, discussing both the monolayer and the bilayer cases. Chapter three concerns the electromechanical properties of graphene and will include a discussion of the elastic theory of membranes and the electromechanical properties of both monolayer and bilayer graphene. In chapter four we discuss the electronic quantum transport of ballistic bilayer graphene under the application of uniaxial strain. Chapter five consists of a discussion of the electromechanical properties of transition metal dichalcogenides with a focus on electron-vibron coupling in these systems. Finally in chapter six we will conclude and discuss remaining questions and possible extensions of this work.

Bibliography

- [1] K. S. Novoselov, A. K. Geim, S. V. Morozov, D. Jiang, Y. Zhang, S. V. Dubonos, I. V. Grigorieva, and A. A. Firsov, “Electric field effect in atomically thin carbon films,” *Science*, vol. 306, pp. 666–669, 10 2004.
- [2] T. Ando, T. Nakanishi, and S. R., “Berry’s phase and absence of back scattering in carbon nanotubes,” *Journal of the Physical Society of Japan*, vol. 67, no. 8, pp. 2857–2862, 1998.
- [3] M. I. Katsnelson, K. S. Novoselov, and A. K. Geim, “Chiral tunnelling and the klein paradox in graphene,” *Nat Phys*, vol. 2, pp. 620–625, 09 2006.
- [4] A. F. Young and P. Kim, “Quantum interference and klein tunnelling in graphene heterojunctions,” *Nat Phys*, vol. 5, pp. 222–226, 03 2009.
- [5] M. I. Katsnelson, “Zitterbewegung, chirality, and minimal conductivity in graphene,” vol. 51, no. 2, pp. 157–160, 2006.
- [6] F. V. Tikhonenko, D. W. Horsell, R. V. Gorbachev, and A. K. Savchenko, “Weak localization in graphene flakes,” *Physical Review Letters*, vol. 100, pp. 056802–, 02 2008.
- [7] F. V. Tikhonenko, A. A. Kozikov, A. K. Savchenko, and R. V. Gorbachev, “Transition between electron localization and antilocalization in graphene,” *Physical Review Letters*, vol. 103, pp. 226801–, 11 2009.
- [8] Y. Zhang, Y. W. Tan, H. L. Stormer, and P. Kim, “Experimental observation of the quantum hall effect and berry’s phase in graphene,” *Nature*, vol. 438, pp. 201–204, 11 2005.

- [9] K. S. Novoselov, A. K. Geim, S. V. Morozov, D. Jiang, M. I. Katsnelson, I. V. Grigorieva, S. V. Dubonos, and A. A. Firsov, “Two-dimensional gas of massless dirac fermions in graphene,” *Nature*, vol. 438, pp. 197–200, 11 2005.
- [10] A. K. Geim and K. S. Novoselov, “The rise of graphene,” *Nat Mater*, vol. 6, pp. 183–191, 03 2007.
- [11] A. H. Castro Neto, F. Guinea, N. M. R. Peres, K. S. Novoselov, and A. K. Geim, “The electronic properties of graphene,” *Reviews of Modern Physics*, vol. 81, pp. 109–162, 01 2009.
- [12] A. B. Kuzmenko, E. van Heumen, F. Carbone, and D. van der Marel, “Universal optical conductance of graphite,” *Physical Review Letters*, vol. 100, pp. 117401–, 03 2008.
- [13] D. C. Elias, R. R. Nair, T. M. G. Mohiuddin, S. V. Morozov, P. Blake, M. P. Halsall, A. C. Ferrari, D. W. Boukhvalov, M. I. Katsnelson, A. K. Geim, and K. S. Novoselov, “Control of graphene’s properties by reversible hydrogenation: Evidence for graphane,” *Science*, vol. 323, no. 5914, pp. 610–613, 2009.
- [14] I. Khrapach, F. Withers, T. H. Bointon, D. K. Polyushkin, W. L. Barnes, S. Russo, and M. F. Craciun, “Novel highly conductive and transparent graphene-based conductors,” *Advanced Materials*, vol. 24, no. 21, pp. 2844–2849, 2012.
- [15] C. Lee, X. Wei, J. W. Kysar, and J. Hone, “Measurement of the elastic properties and intrinsic strength of monolayer graphene,” *Science*, vol. 321, pp. 385–388, 07 2008.
- [16] J. S. Bunch, A. M. van der Zande, S. S. Verbridge, I. W. Frank, D. M. Tanenbaum, J. M. Parpia, H. G. Craighead, and P. L. McEuen, “Electromechanical resonators from graphene sheets,” *Science*, vol. 315, pp. 490–493, 01 2007.
- [17] A. Eichler, J. Moser, J. Chaste, M. Zdrojek, I. Wilson-Rae, and A. Bachtold, “Nonlinear damping in mechanical resonators made from carbon nanotubes and graphene,” *Nat Nano*, vol. 6, pp. 339–342, 06 2011.
- [18] J. C. Meyer, A. K. Geim, M. I. Katsnelson, K. S. Novoselov, T. J. Booth, and S. Roth, “The structure of suspended graphene sheets,” *Nature*, vol. 446, pp. 60–63, 03 2007.

- [19] H. Park, J. Park, A. K. L. Lim, E. H. Anderson, A. P. Alivisatos, and P. L. McEuen, “Nanomechanical oscillations in a single-c60 transistor,” *Nature*, vol. 407, pp. 57–60, 09 2000.
- [20] R. Leturcq, C. Stampfer, K. Inderbitzin, L. Durrer, C. Hierold, E. Mariani, M. G. Schultz, F. von Oppen, and K. Ensslin, “Franck-condon blockade in suspended carbon nanotube quantum dots,” *Nat Phys*, vol. 5, pp. 327–331, 05 2009.
- [21] M. A. H. Vozmediano, M. I. Katsnelson, and F. Guinea, “Gauge fields in graphene,” *Physics Reports*, vol. 496, pp. 109–148, 11 2010.
- [22] V. M. Pereira and A. H. Castro Neto, “Strain engineering of graphene’s electronic structure,” *Physical Review Letters*, vol. 103, pp. 046801–, 07 2009.
- [23] V. M. Pereira, A. H. Castro Neto, and N. M. R. Peres, “Tight-binding approach to uniaxial strain in graphene,” *Physical Review B*, vol. 80, pp. 045401–, 07 2009.
- [24] F. Guinea, M. I. Katsnelson, and A. K. Geim, “Energy gaps and a zero-field quantum hall effect in graphene by strain engineering,” *Nat Phys*, vol. 6, pp. 30–33, 01 2010.
- [25] N. Levy, S. A. Burke, K. L. Meaker, M. Panlasigui, A. Zettl, F. Guinea, A. H. C. Neto, and M. F. Crommie, “Strain-induced pseudo-magnetic fields greater than 300 tesla in graphene nanobubbles,” *Science*, vol. 329, no. 5991, pp. 544–547, 2010.
- [26] C. R. Dean, A. F. Young, M. I., L. C., W. L., S. S., W. K., T. T., K. P., S. K. L., and H. J., “Boron nitride substrates for high-quality graphene electronics,” *Nat Nano*, vol. 5, pp. 722–726, 10 2010.
- [27] A. Splendiani, L. Sun, Y. Zhang, T. Li, J. Kim, C. Y. Chim, G. Galli, and F. Wang, “Emerging photoluminescence in monolayer mos2,” *Nano Letters*, vol. 10, pp. 1271–1275, 2014/04/10 2010.
- [28] K. F. Mak, C. Lee, J. Hone, J. Shan, and T. F. Heinz, “Atomically thin mos2: A new direct-gap semiconductor,” *Physical Review Letters*, vol. 105, pp. 136805–, 09 2010.
- [29] B. Radisavljevic, A. Radenovic, J. Brivio, V. Giacometti, and A. Kis, “Single-layer mos2 transistors,” *Nat Nano*, vol. 6, pp. 147–150, 03 2011.

2

Electronic Properties of Graphene

2.1 Introduction

The theoretical study of graphene started with interest in the electronic properties of graphite in the late 1940's and early 1950's.[1, 2, 3] Indeed in 1947 P. R. Wallace calculated the band structure of a graphite monolayer and showed its unusual gapless bands and low energy conical dispersion. Since this time the monolayer honeycomb lattice was seen as an interesting curiosity which received some attention due to its unique properties in a condensed matter context.[4, 5, 6] By the time of the experimental realisation and isolation of graphene monolayers in 2004 many of the key features of graphene which are discussed within this chapter were well understood and could finally be observed and confirmed.

Graphene was first isolated by a process called mechanical exfoliation. This process involves shearing the layered bulk graphite apart with common sticky tape creating two thinner graphite flakes. Each time this is repeated it generates thinner and thinner graphite layers. Once

this process has been diligently performed a great many times amongst the many flakes produced there will be one atom thick layers, graphene monolayers. The key insight was to use optical techniques to identify the monolayer flakes. It was found that the number of layers which comprise thin graphite flakes could be found by studying the interference induced contrast shifts of flakes deposited on a SiO₂ wafer in optical images.[7] This can be seen in Fig. 2.1.a which shows a graphite flake with regions of differing thickness ranging from bulk graphite to monolayer which are shown by their colour contrast and are marked in the optical image. Flake thickness can also be determined by using Raman spectroscopy or by electrical transport measurements in the quantum Hall regime but these techniques are far more involved and cannot be automated.

Once graphene flakes have been isolated they are used in the fabrication of electronic devices which utilise graphene's rich properties. The field effect transistor is a widely used device design that uses electric fields to control charge density within a semiconductor sample. A graphene field effect transistor consists of a graphene flake placed upon a substrate with a back gate and two electrical contacts, a schematic of this setup is shown in Fig. 2.1.b. The two contacts allow for a voltage V_{sd} to be applied across the sample and are called the source and drain, while the chemical potential can be modulated via a back gate which is located below the SiO₂ dielectric substrate. By charging the back gate with a voltage V_{bg} the effective capacitor with the SiO₂ dielectric induces a charge density in the device.

Graphene field effect transistors allow for the charge carriers responsible for electrical transport to be continuously tuned between electrons and holes. This unusual behaviour is known as the ambipolar electric field effect and can be seen in conductivity measurements performed as function of back gate voltage. Experimental data showing this effect can be seen in Fig. 2.1.c. For positive back gate voltages $V_{bg} > 0$ the graphene sample is electron doped. Reducing the back gate voltage leads to a reduced carrier concentration and a decreased conductivity until $V_{bg} = 0$ which corresponds to the chemical potential lying at the Dirac point. Continuing to change the back gate voltage to negative values $V_{bg} < 0$ leads the sample to become hole doped and increasing the doping and carrier concentration increases the conductivity. This gives the conductivity in graphene a distinct symmetric behaviour around the Dirac point.

One of the most striking features of graphene is that it never becomes insulating, despite a vanishing density of states at the Fermi level in undoped pristine graphene. As shown in the electrical transport data presented in Fig. 2.1.c the conductivity never vanishes, instead it approaches

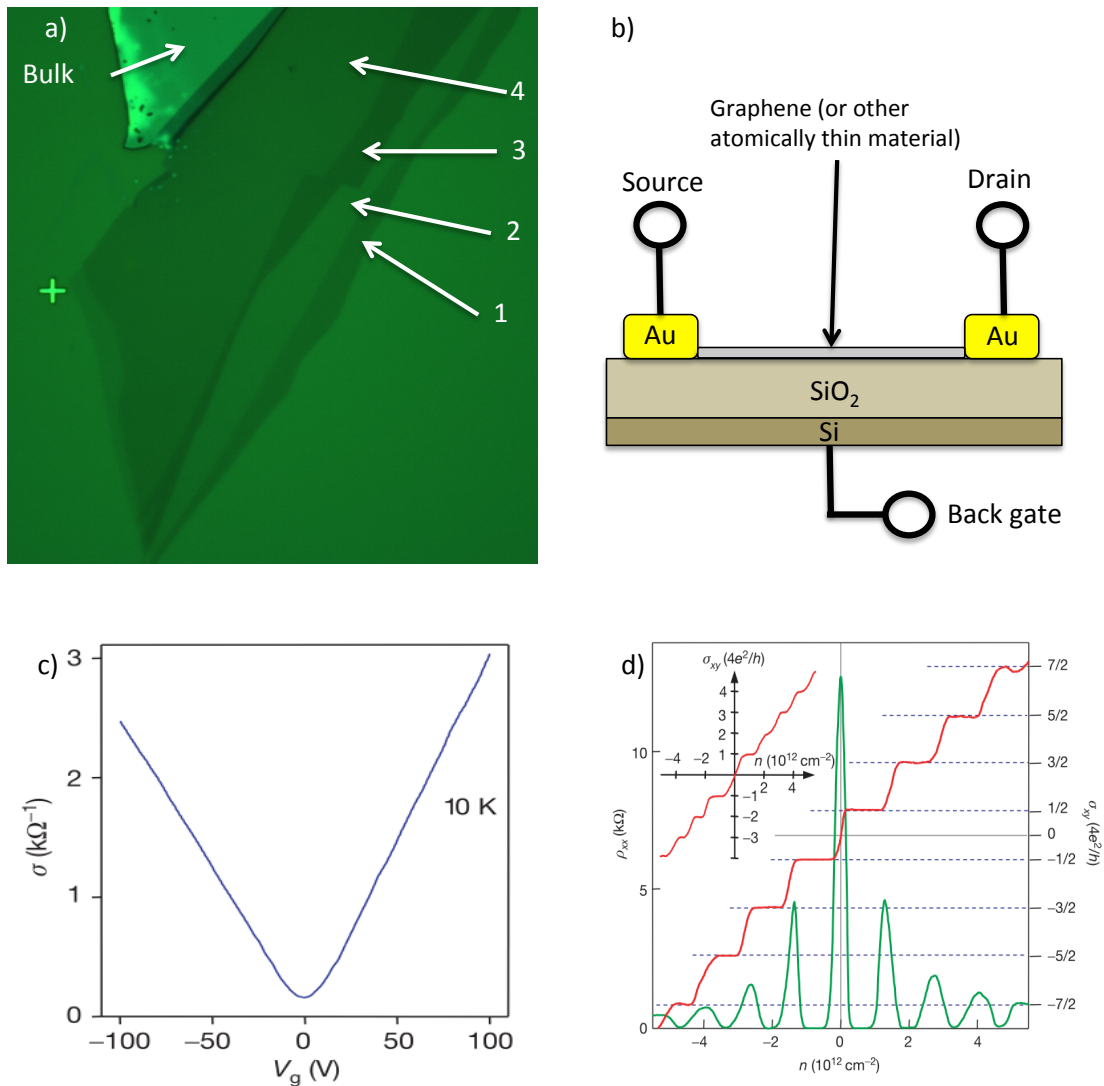


Figure 2.1: Examples of graphene devices and their conductivity and quantum Hall characteristics. Panel a) shows an optical image of a graphene flake where the contrast of the image taken under green light allows for the identification of the flake thickness, which has been marked on the image (The image is provided courtesy of T.H Bointon). Panel b) shows a schematic of a design for a field effect transistor. Panel c) shows the change in graphene conductivity as a function of back gate voltage while panel d) shows the anomalous quantum Hall effect for Dirac fermions with the Hall conductivity in red and longitudinal resistivity in green, both as functions of carrier density for monolayer graphene. The measurements here are performed at $B = 14\text{T}$ and $T = 4\text{K}$. The insert in the panel d) shows the Hall conductivity for bilayer graphene. Both panels c) and d) are taken from Novoselov et al, Nature, 438, 11, (2005).[8]

a finite minimal value at the Dirac point which corresponds to the energy at which the density of states vanishes. This finite minimal conductivity has a theoretically predicted universal value of $\sigma = 4e^2/\pi h$ for graphene monolayers.[9] The physics of electrical transport at the Dirac point can be probed further in shot noise experiments in extremely clean samples. These find a univer-

sal value of the Fano factor of $1/3$ which corresponds to that expected of a disordered conductor even though these measurements are performed on high quality clean graphene in the ballistic regime.[10] The electrical transport experiments on graphene at the Dirac point highlights the unusual properties of the charge carriers in graphene, behaving as massless Dirac fermions, in stark contrast to what expected in normal semiconductor systems.

The role of the chiral Dirac fermions is also seen at energy scales away from the Dirac point, this becomes most clear across regions of varying doping such as p-n junctions. The chirality manifests itself when massless Dirac fermions approaching a potential step at normal incidence cross the barrier with transmission probability of one. This anomalous effect is known as Klein tunnelling.[11] The opposite situation occurs in graphene bilayers where the chiral massive Dirac fermions incident at normal incidence have their transmission suppressed to zero. In both cases away from normal incidence there will be angles which will allow perfect transmission, these angles depend on the details of the potential step and wave vector of the incident Dirac electron. This behaviour means that Dirac fermions in graphene are highly insensitive to smooth disorder, a crucial factor that ultimately leads to the high electrical quality of graphene. The details of these ideas and concepts will be thoroughly discussed within this chapter.

Another consequence of the Dirac physics present in graphene is the anomalous quantum Hall effect. Under a large perpendicular magnetic field at low temperatures the electronic spectrum of two-dimensional electronic systems form Landau levels, entering the quantum Hall regime which is characterised by a quantised Hall resistivity $\sigma_{xy} = \nu e^2/h$. Here ν is known as the filling factor and represents the ratio between the densities of electrons and magnetic flux quanta in the system. Graphene shows quantitatively different behaviour in this regime compared to normal Schrödinger electrons, having Hall plateaus quantised at anomalous half integer values and a Landau level spectrum with the $n = 0$ Landau level being pinned at zero energy. In Fig. 2.1.d we show experimental data of transport measurements in the quantum Hall regime for monolayer graphene, while the insert shows bilayer graphene. Here in monolayer graphene we see the anomalous quantisation of σ_{xy} at half integer values with $\nu = 4(n + 1/2)$ where n refers to the n th Landau level and the positions of the Landau levels can be identified by peaks in the longitudinal resistivity ρ_{xx} . These measurements reveal a Landau level spectrum given by $\epsilon \sim \pm \sqrt{|nB|}$ with the associated $n = 0$ Landau level at zero energy. We also see that bilayer graphene has its own distinct Landau level spectrum with a quantised Hall resistivity given by filling factors $\nu = 4(n + 1)$ and an energy

dependence of $\epsilon \sim \pm \sqrt{|n(n-1)B|}$. This unusual spectrum gives a zero energy Landau level which is doubly degenerate in the orbital quantum number n . As a consequence of the quantisation of the Hall resistivity being unique to the number of layers which comprise the graphene flake, quantum Hall measurements make an incredibly accurate probe of the number of layers in a graphene device. The quantum Hall effect is very robust in graphene due to the large Landau level spacing. In fact in monolayers the $\nu = \pm 2$ state has been observed at room temperature and at fields as low as 1T, making graphene an ideal material to study the rich physics which can arise in quantum Hall regime.[12]

In this chapter we will introduce the tight binding approach to the study of the electronic properties of graphene. First we will pedagogically present the electronic properties of monolayer graphene, focusing first on the electronic dispersion followed by the effective theory of the massless Dirac fermions, including the effects due to pseudo spin, the electron's Berry phase and trigonal warping. Then we shall turn our attention to bilayer graphene following a similar structure. We will present the electronic dispersion of both the four-band model and the two-band effective low-energy model, followed by a discussion of the effective theory of massive chiral Dirac fermions, with particular focus on the electron's Berry phase and the peculiar form of trigonal warping which arises in bilayer graphene.

2.2 Electronic Properties of Monolayer Graphene

Graphene consists of a monoatomic layer of carbon atoms arranged in a honeycomb lattice. The carbon atoms are bonded together by sp^2 hybridisation between one s orbital and the p_x and p_y orbitals. This leads to the formation of in-plane carbon-carbon σ bonds which create the honeycomb structure of the lattice with the unaffected p_z orbital which lies perpendicular to the planar structure. This can bind covalently with neighbouring carbon atoms, leading to the formation of a π band. The σ bands form a deep valence band, however as each p orbital has one extra electron the π band is half filled. Here we present the tight binding analysis which describes the low energy electronic spectrum of the π bands.

The honeycomb structure is not a Bravais lattice, and can be seen as a triangular lattice with a two atoms basis. The crystal structure can be seen in Fig. 2.2.a, with one sublattice coloured red, which we label A, and the other blue, which we label B. The lattice vectors can be written as

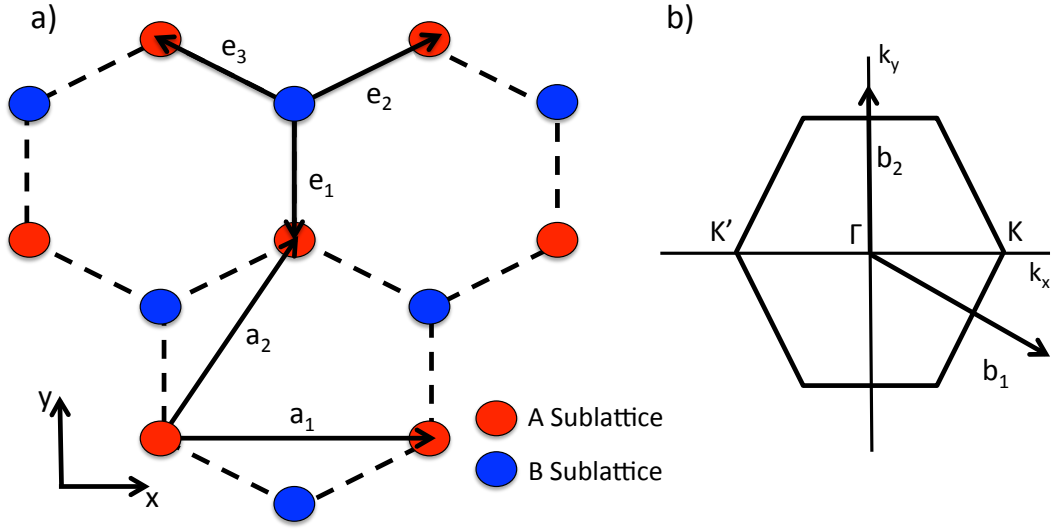


Figure 2.2: The crystal lattice of monolayer graphene is shown in a) with the A sublattice shown in red and the B sublattice shown in blue. The lattice vectors for each sublattice \mathbf{a}_i are shown as well as the nearest neighbour vectors \mathbf{e}_j . The corresponding Brillouin zone is shown in b) with the reciprocal lattice vectors \mathbf{b}_i , the Dirac points \mathbf{K} and \mathbf{K}' and the Γ point marked.

$$\mathbf{a}_1 = a(\sqrt{3}, 0), \quad \mathbf{a}_2 = \frac{a}{2}(\sqrt{3}, 3), \quad (2.1)$$

where $a = 1.42 \text{ \AA}$, is the carbon-carbon distance. From this the reciprocal lattice vectors are obtained as

$$\mathbf{b}_1 = \frac{2\pi}{3\sqrt{3}a}(3, -\sqrt{3}), \quad \mathbf{b}_2 = \frac{4\pi}{3\sqrt{3}a}(0, \sqrt{3}), \quad (2.2)$$

and are depicted in fig 2.2.b which also shows the 1st Brillouin zone of the honeycomb structure.

To perform a tight binding analysis we consider the nearest neighbour vectors connecting the A and B lattice sites which are $\mathbf{e}_1 = a(0, -1)$, $\mathbf{e}_2 = a/2(\sqrt{3}, 1)$ and $\mathbf{e}_3 = a/2(-\sqrt{3}, 1)$. We write the tight binding Hamiltonian for electrons in a honeycomb lattice considering hopping between nearest neighbour atoms as

$$H = -t \sum_{\mathbf{R}_B} \sum_{j=1}^3 |\mathbf{R}_B\rangle \langle \mathbf{R}_B + \mathbf{e}_j| + h.c. \quad (2.3)$$

where \mathbf{R}_s is the position of an atom in the sublattice s ($s = A/B$), and $|\mathbf{R}_s\rangle$ is the ket associated with the corresponding localised orbital. Here we used the identities $\mathbf{R}_A = \mathbf{R}_B + \mathbf{e}_j$. In the tight

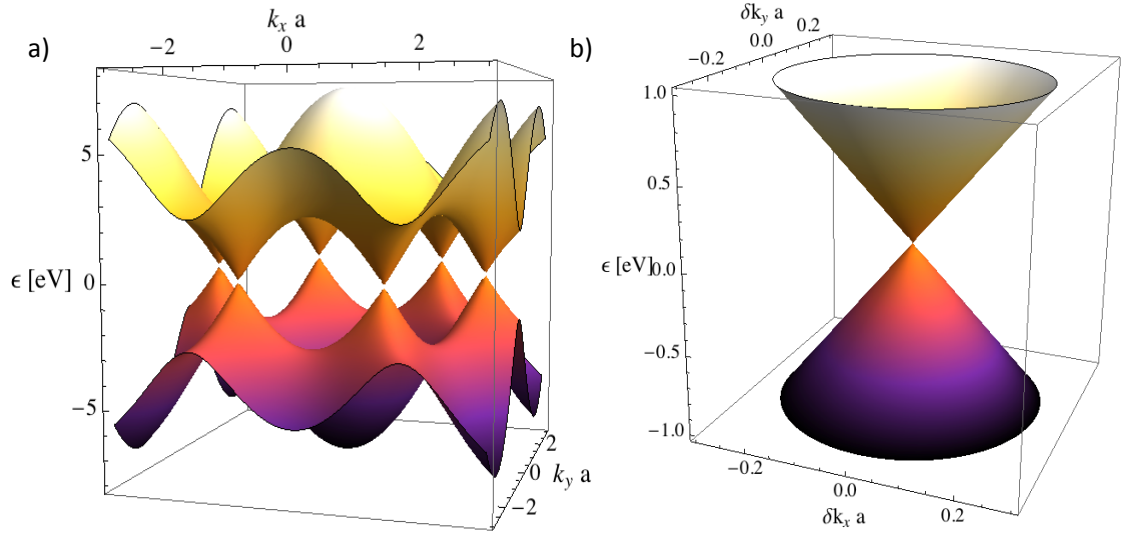


Figure 2.3: The electronic dispersion of monolayer graphene. Panel a) shows the whole dispersion in which the two bands only meet at $\epsilon_{\mathbf{k}} = 0$ at the so called Dirac points. Panel b) shows the low energy sector in the vicinity of the Dirac points revealing the conical dispersion.

binding approximation t is the energy scale associated with electrons hopping between the two neighbouring sites \mathbf{R}_s and $\mathbf{R}_{s'}$ and in monolayer graphene it is $t = 2.6$ eV.[13]

Electronic eigenstates in monolayer graphene are described by Bloch states of the form

$$|\psi_{\mathbf{k}}\rangle = \sum_{\mathbf{R}_A} u_{\mathbf{k}}^{(A)} e^{i\mathbf{k}\cdot\mathbf{R}_A} |\mathbf{R}_A\rangle + \sum_{\mathbf{R}_B} u_{\mathbf{k}}^{(B)} e^{i\mathbf{k}\cdot\mathbf{R}_B} |\mathbf{R}_B\rangle \quad (2.4)$$

where $u_{\mathbf{k}}^{(s)}$ is the amplitude of the wavefunction in the sublattice s at wavevector \mathbf{k} . Therefore acting with the tight binding Hamiltonian Eq. 2.3 upon the Bloch states in Eq. 2.4 we may rewrite the Hamiltonian in the 2×2 space of the Bloch amplitudes $(u_{\mathbf{k}}^{(A)}, u_{\mathbf{k}}^{(B)})$ with the Hamiltonian in the matrix form

$$H = \begin{pmatrix} 0 & -t f_{\mathbf{k}}^* \\ -t f_{\mathbf{k}} & 0 \end{pmatrix} \quad (2.5)$$

where $f_{\mathbf{k}} = \sum_{j=1}^3 \exp[i\mathbf{k} \cdot \mathbf{e}_j]$. By explicit calculation with the vectors \mathbf{e}_j above we may now diagonalise this Hamiltonian and obtain two bands with the electronic dispersion

$$\epsilon_{\mathbf{k}} = \pm t \sqrt{1 + 4 \cos \frac{\sqrt{3}k_x a}{2} \cos \frac{3k_y a}{2} + 4 \cos^2 \frac{\sqrt{3}k_x a}{2}}. \quad (2.6)$$

This is the electronic spectrum of the π bands in monolayer graphene and is shown in Fig. 2.3. The bandstructure is gapless with the two bands touching at $\epsilon_{\mathbf{k}} = 0$ at the \mathbf{K} and \mathbf{K}' points

at the edge of the Brillouin zone. The points at which the bands touch are called Dirac points or valleys, and this terminology will be used interchangeably for the rest of this work. By solving Eq. 2.6 for $\epsilon_{\mathbf{k}} = 0$ we find that there are two inequivalent Dirac points within the 1st Brillouin zone. They are given by

$$\mathbf{K} = \left(\frac{4\pi}{3\sqrt{3}a}, 0 \right), \quad \mathbf{K}' = -\left(\frac{4\pi}{3\sqrt{3}a}, 0 \right). \quad (2.7)$$

As $\mathbf{K} = -\mathbf{K}'$ we introduce a valley index $\tau = \pm 1$ which allows us to write the two Dirac points in the compact form $\mathbf{K}_\tau = \tau(4\pi/3\sqrt{3}a, 0)$. In undoped graphene the Fermi level will lie exactly at $\epsilon_{\mathbf{k}} = 0$. The electronic spectrum we have shown in Fig. 2.3 spans a wide range of energy reaching an energy scale of ≈ 8 eV at the Γ point, which corresponds to a temperature of $3 \cdot 10^4$ K. In this work we are primarily interested in the electronic transport properties of graphene which concerns only low energy processes, therefore the only relevant physics is that which occurs in the vicinity of the Dirac points. To study this low energy sector of our tight binding model we expand the Hamiltonian close to the \mathbf{K} (or \mathbf{K}') point with $\mathbf{k} = \mathbf{K}_\tau + \delta\mathbf{k}$ in the small parameter $|\delta\mathbf{k}|a \ll 1$.

Upon expanding around the Dirac point to the leading non-vanishing order the function $f_{\mathbf{k}}$ becomes

$$f_{\mathbf{k}} = \sum_{j=1}^3 \exp[i\mathbf{K}_\tau \cdot \mathbf{e}_j] \exp[i\delta\mathbf{k} \cdot \mathbf{e}_j] \approx \sum_{j=1}^3 \exp[i\mathbf{K}_\tau \cdot \mathbf{e}_j] (1 + i\delta\mathbf{k} \cdot \mathbf{e}_j). \quad (2.8)$$

Using this expansion in Eq 2.5 we find the effective Hamiltonian in the vicinity of one Dirac point, which can be written in the 2×2 space of the Bloch amplitudes $(u_{\mathbf{k}}^{(A,\tau)}, u_{\mathbf{k}}^{(B,\tau)})$ as

$$H^{(\tau)} = v\hbar \begin{pmatrix} 0 & \tau\delta k_x - i\delta k_y \\ \tau\delta k_x + i\delta k_y & 0 \end{pmatrix} \quad (2.9)$$

where we have introduced the Fermi velocity $v = 3ta/2\hbar = 8 \times 10^5 \text{ms}^{-1}$. From this point on we will assume we always work near the Dirac points and use \mathbf{k} to refer to the small momentum $\delta\mathbf{k}$. We may also write the Hamiltonian Eq. 2.9 in the language of Pauli matrices as

$$H^{(\tau)} = v\hbar (\tau\sigma_x k_x + \sigma_y k_y) \quad (2.10)$$

where the Pauli matrices σ_i take their usual definition, which we give here for clarity

$$\sigma_0 = \begin{pmatrix} 1 & 0 \\ 0 & 1 \end{pmatrix}, \sigma_x = \begin{pmatrix} 0 & 1 \\ 1 & 0 \end{pmatrix}, \sigma_y = \begin{pmatrix} 0 & -i \\ i & 0 \end{pmatrix}, \sigma_z = \begin{pmatrix} 1 & 0 \\ 0 & -1 \end{pmatrix}. \quad (2.11)$$

Diagonalising the effective Hamiltonian $H^{(\tau)}$ we find the electronic spectrum around one Dirac cone

$$\epsilon_{\mathbf{k}} = \pm v\hbar|k| \quad (2.12)$$

where $k = \tau k_x + ik_y$. This gives the celebrated linear dispersion of graphene. This differs greatly from that used to describe most materials, where usually electrons are effectively described by the massive quasiparticle dispersion $\epsilon_{\mathbf{k}} = \hbar^2|\mathbf{k}|^2/2m$, as the Fermi velocity of the linear dispersion does not depend on energy or momentum. Indeed, this result is equivalent to solving the two dimensional massless Dirac equation with the speed of light c replaced by the Fermi velocity $v \approx c/300$. As a consequence the charge carriers in graphene are called massless Dirac fermions. The electronic density of states close to zero energy is linear as we have 2D massless charge carriers, and is given by $\nu(\epsilon) = 3\sqrt{3}a^2|\epsilon|/\pi v^2$.

The Hamiltonians in the two valleys are related by the symmetry $H^{(+)} = H^{(-)\dagger}|_{k \rightarrow -k}$, which indeed shows that taking the time reversal of the Hamiltonian is equivalent to exchanging the two valleys. The two valleys are separated by a large wavevector scale of order $1/a$ therefore inter-valley scattering is usually sharply suppressed, except for atomic scatterers. We can write a Hamiltonian which describes both valleys within a low energy Hamiltonian which contains both of the inequivalent Dirac points. In the 4×4 space of the Bloch amplitudes $(u_{\mathbf{k}}^{(A,+)}, u_{\mathbf{k}}^{(B,+)}, u_{\mathbf{k}}^{(B,-)}, u_{\mathbf{k}}^{(A,-)})$ this takes the form

$$H = v\hbar \begin{pmatrix} 0 & k_x - ik_y & 0 & 0 \\ k_x + ik_y & 0 & 0 & 0 \\ 0 & 0 & 0 & -k_x + ik_y \\ 0 & 0 & -k_x - ik_y & 0 \end{pmatrix} \quad (2.13)$$

which usefully allows us to write the whole Hamiltonian for both valleys in the language of Pauli

matrices as

$$H = v\hbar\Sigma_z \otimes (\sigma_x k_x + \sigma_y k_y). \quad (2.14)$$

Here the Pauli matrices σ_i act in the A/B sublattice space and the Pauli matrices Σ_j act in the $\tau = \pm 1$ valley space.

2.2.1 Massless Dirac Fermions

As we have just shown, graphene is a gapless semiconductor and while that is interesting in itself it is the properties of the massless Dirac fermions that give graphene its wealth of remarkable qualities.

Now that we have a clear idea of the electronic dispersion we need to study the electronic eigenstates of monolayer graphene. Using the Hamiltonian Eq. 2.10 with the dispersion in Eq. 2.12, we can determine the plane wave eigenstate with a wavevector \mathbf{k} . In the $\tau = +1$ valley we find

$$|\psi_{\mathbf{k},s}^{(+)}\rangle = \frac{1}{\sqrt{2}} \begin{pmatrix} 1 \\ s e^{i\phi_{\mathbf{k}}} \end{pmatrix} e^{i\mathbf{k}\cdot\mathbf{r}} = u_{\mathbf{k},s}^{(+)} e^{i\mathbf{k}\cdot\mathbf{r}} \quad (2.15)$$

where $\phi_{\mathbf{k}} = \arctan(k_y/k_x)$ and $s = \text{sign}(\epsilon_{\mathbf{k}})$. Here $s = +1$ refers of the upper band (electrons) and $s = -1$ refers to the lower band (holes). Similarly in the $\tau = -1$ valley we find

$$|\psi_{\mathbf{k},s}^{(-)}\rangle = \frac{1}{\sqrt{2}} \begin{pmatrix} 1 \\ -s e^{-i\phi_{\mathbf{k}}} \end{pmatrix} e^{i\mathbf{k}\cdot\mathbf{r}} = u_{\mathbf{k},s}^{(-)} e^{i\mathbf{k}\cdot\mathbf{r}}. \quad (2.16)$$

The spinor $u_{\mathbf{k},s}^{(\tau)}$ of the eigenstates shown in Eq. 2.15 and Eq. 2.16 do not in this case refer to the real spin degree of freedom and is therefore called pseudo-spin. This new internal degree of freedom arises due to the two sublattices A and B and describes the distribution of the electronic wave function across the sublattices, so 'up' refers to the A sublattice and 'down' to the B sublattice. This pseudo-spin degree of freedom is related to some special properties of the Dirac fermions as we can see by the following argument. First we consider the eigenvalue equation in the form

$$\tau v\hbar\boldsymbol{\sigma} \cdot \mathbf{k} |\psi_{\mathbf{k},s}^{(\tau)}\rangle = s v\hbar k |\psi_{\mathbf{k},s}^{(\tau)}\rangle \quad (2.17)$$

where $\boldsymbol{\sigma} = (\sigma_x, \sigma_y, \sigma_z)$ and $\mathbf{k} = (k_x, k_y, 0)$. We can rewrite this in terms of the pseudo-spin vector, giving a new eigenvalue equation which defines a new operator, the chirality operator

$$\tau \boldsymbol{\sigma} \cdot \frac{\mathbf{k}}{|\mathbf{k}|} = s \mathbf{1} . \quad (2.18)$$

where $\mathbf{1}$ is the 2×2 unit matrix. It follows that the chirality operator $\boldsymbol{\sigma} \cdot \hat{\mathbf{k}}$ can only have the eigenvalues ± 1 . From this we see that in the $\tau = +1$ valley for the electrons ($s = +1$) the pseudo-spin σ must lie in the same direction as the momentum, whereas for holes ($s = -1$) the pseudo-spin σ must lie in the opposite direction. Therefore massless Dirac fermions in graphene are characterised by a well defined chirality, which has important implications for electronic transport.

The chirality eigenvalue is a good quantum number of the eigenstates in graphene described by the Hamiltonian 2.9 is valid and therefore is conserved. One of the most remarkable effects due to the conservation of chirality is the absence of elastic backscattering off smooth potentials. This can be seen by considering the matrix element due to a smooth impurity potential $\hat{V} = \mathbf{1}V_0$ between two electron states with opposite wave vectors $\langle \psi_{\mathbf{k}',s'} | \hat{V} | \psi_{\mathbf{k},s} \rangle$. Due to the spinor components this is proportional to $V_0(1 + ss'e^{i\pi})$ as $\mathbf{k}' = -\mathbf{k}$ implies $\phi_{\mathbf{k}'} = \phi_{\mathbf{k}} + \pi$, meaning the overlap will vanish for $s = s'$, which is the case for elastic backscattering with $\epsilon_{-\mathbf{k}} = \epsilon_{\mathbf{k}}$. In fact the only way for back scattering processes to occur is by inter-valley scattering which is highly suppressed for smooth potentials due to the large momentum scales involved. This has important consequences for the calculations of the electrical resistivity of graphene as any smooth potential such as Coulomb scatterers will be unable to cause elastic back scattering, which can only be caused by sharp impurities such as vacancies in the atomic lattice. From this line of argument we see that the low electrical resistivity of graphene is not directly due to any inherent high quality of the graphene sample or a lack of impurities but is an intrinsic property stemming from the nature of electrons as massless Dirac fermions.

Another consequence of the chiral nature of Dirac fermions is that they possess a nontrivial Berry phase of $\varphi_B = \pi$. [14] Berry phase is a geometric phase that is accumulated by a particle which is transported adiabatically over a closed loop in momentum space. [15] In graphene due to the chirality condition forcing a coupling between pseudo-spin and momentum a nontrivial geometric phase will be accumulated around a closed loop around the Dirac cone. We can write the Berry phase in terms of the graphene two component spinors as

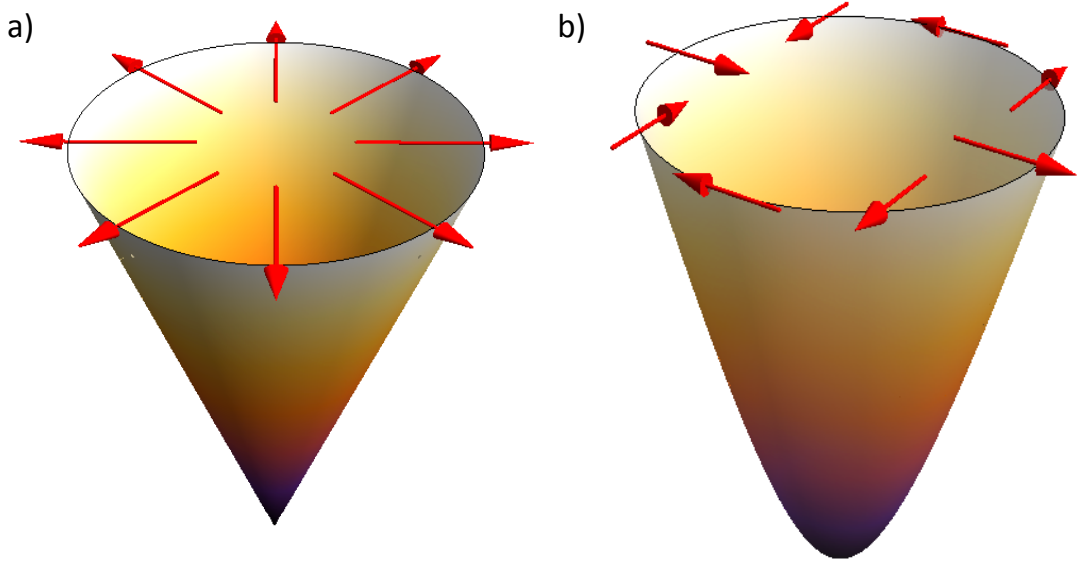


Figure 2.4: The winding of the pseudo-spin around a closed loop encircling the Dirac point. Panel a) shows the winding of the pseudo-spin around the dispersion of monolayer graphene, panel b) shows the winding of the pseudo-spin around the dispersion of bilayer graphene where in contrast to the monolayer case it winds twice around a closed loop.

$$\varphi_B = i \oint d\phi u_{\mathbf{k},s}^{(\tau)\dagger} \partial_\phi u_{\mathbf{k},s}^{(\tau)} = \tau\pi \quad (2.19)$$

where π arises as we consider an anti-clockwise path around the Dirac point. This is shown more clearly in Fig. 2.4.a which shows the linear dispersion in the vicinity of the Dirac point and pseudo-spin vectors along a closed loop around the Dirac point. Fig. 2.4.a highlights the 2π solid angle enclosed as the pseudo-spin winds once around the loop. The appearance of a non-zero Berry phase can be directly probed by a shift in the de Haas-van Alphen and Shubnikov-de Haas oscillations[16, 17] and the peculiar form of the electronic spectrum of Landau levels created in graphene can be seen as a direct consequence of the Berry phase.[18]

2.2.2 Trigonal Warping

When calculating the Hamiltonian close to the Dirac points we expanded up to leading order in the small parameter $|k|a \ll 1$, this procedure gives the very recognisable conical dispersion around the Dirac points. This approximation holds well for low energies, but we may also consider the second order correction to it, adding a parabolic component to the electronic dispersion. Keeping second order terms we obtain

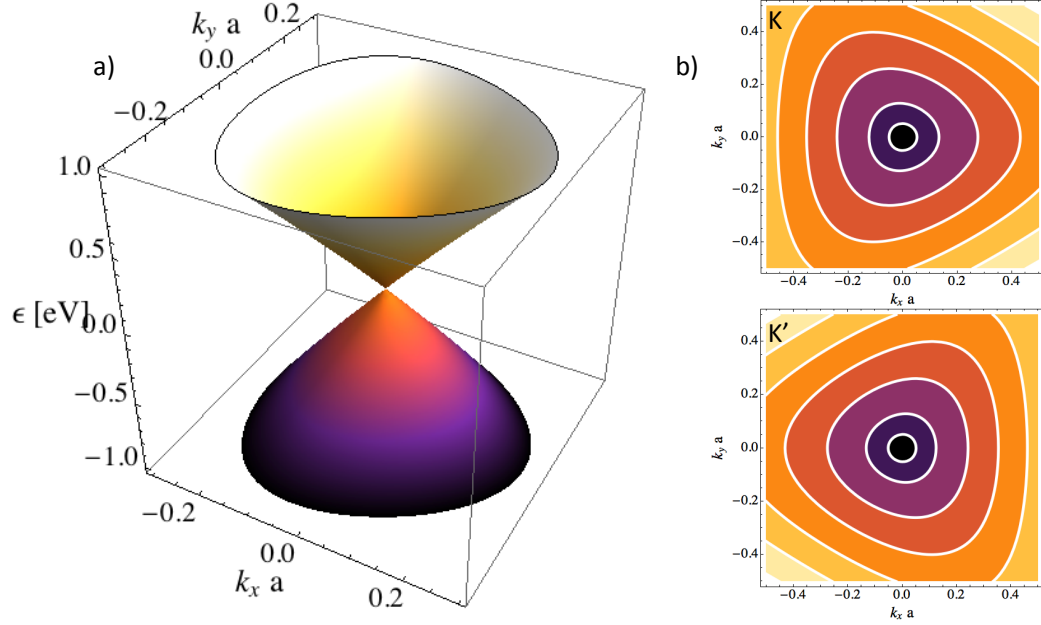


Figure 2.5: The trigonal warping in monolayer graphene is shown. Panel a) shows a Dirac cone warped by trigonal warping while panel b) shows equipotential lines of the trigonally warped dispersion around the \mathbf{K} and \mathbf{K}' points. Here dark areas correspond to states close to zero energy while light ones are for higher energies. The white contours occur at energies $\epsilon_{\mathbf{k}} = 0.2$ eV, and then $\epsilon_{\mathbf{k}} = 0.5$ eV then following in steps of 0.5 eV.

$$H^{(\tau)} = v\hbar(\tau\sigma_x k_x + \sigma_y k_y) + \tau \frac{3ta^2}{8} (\sigma_x(k_x^2 - k_y^2) + 2\sigma_y k_x k_y) \quad (2.20)$$

and the electronic dispersion this Hamiltonian gives is shown in Fig. 2.5. The electronic spectrum with the second order corrections is called a trigonally warped dispersion as the introduction of second order corrections above lowers the rotational symmetry of the conical dispersion to a 'trigonal' three fold rotational symmetry. We also see in Fig. 2.5 that the shape of the equipotential lines are different in each of the valleys, with the trigonal warping at the \mathbf{K}' point being rotated by an angle π with respect to the \mathbf{K} point.

2.3 Electronic Properties of Bilayer Graphene

Bilayer graphene consists of two coupled monolayer crystals of graphene. The monolayer graphene layers are stacked in the Bernal configuration shown in Fig. 2.6 and they are separated by an interlayer distance $c = 3.34\text{\AA}$. The carbon atoms in the two layers are identified by a layer index, $l = 1, 2$ for the bottom and top layer respectively. The Bernal stacking configuration involves the atoms on layer 2 and sublattice A (i.e. of type A2) being located directly above those of type B1.

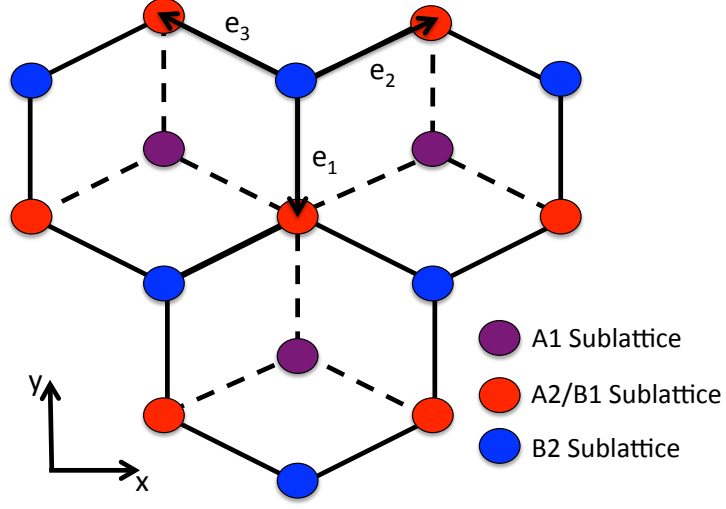


Figure 2.6: The crystal lattice of bilayer graphene in Bernal stacking shown in a top down view. The honeycomb lattice with the solid (dashed) lines corresponding to the upper (lower) layer $l = 2$ ($l = 1$). The atomic sites A2 and B1 coincide once projected onto the plane. The three nearest neighbour vectors \mathbf{e}_j which connect the A and B sublattice are shown.

In contrast the B2 atoms are not located above the A1 atoms, in fact the A1-A2, B1-B2 and A1-B2 bonds are separated by the non-vertical skew distance $\tilde{c} = \sqrt{a^2 + c^2} \simeq 3.63\text{\AA}$.

We can perform a tight binding analysis to study the electronic properties of bilayer graphene in analogy to the monolayer case.[19, 20, 21] We begin with the tight binding Hamiltonian for electrons in a bilayer Bernal stacked honeycomb lattice considering all hopping terms between nearest neighbours which gives

$$\begin{aligned}
 H = & -t_{A1,B1} \sum_{\mathbf{R}_{B1}} \sum_{j=1}^3 |\mathbf{R}_{B1}\rangle \langle \mathbf{R}_{B1} + \mathbf{e}_j| \\
 & -t_{A2,B2} \sum_{\mathbf{R}_{B2}} \sum_{j=1}^3 |\mathbf{R}_{B2}\rangle \langle \mathbf{R}_{B2} + \mathbf{e}_j| \\
 & -t_{A2,B1} \sum_{\mathbf{R}_{B1}} |\mathbf{R}_{B1}\rangle \langle \mathbf{R}_{B1} + c\hat{\mathbf{z}}| \\
 & -t_{A1,B2} \sum_{\mathbf{R}_{B2}} \sum_{j=1}^3 |\mathbf{R}_{B2}\rangle \langle \mathbf{R}_{B2} - \mathbf{e}_j - c\hat{\mathbf{z}}| \\
 & -t_{A1,A2} \sum_{\mathbf{R}_{A2}} \sum_{j=1}^3 |\mathbf{R}_{A2}\rangle \langle \mathbf{R}_{A2} + \mathbf{e}_j - c\hat{\mathbf{z}}| \\
 & -t_{B1,B2} \sum_{\mathbf{R}_{B2}} \sum_{j=1}^3 |\mathbf{R}_{B2}\rangle \langle \mathbf{R}_{B2} + \mathbf{e}_j - c\hat{\mathbf{z}}| + h.c.
 \end{aligned} \tag{2.21}$$

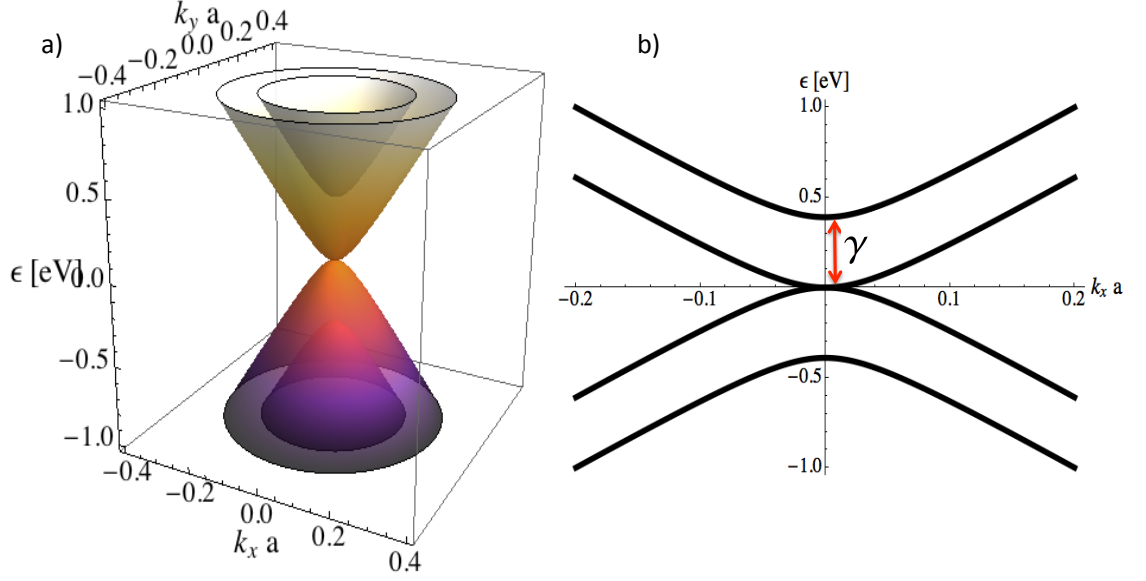


Figure 2.7: The band structure of bilayer graphene, neglecting the γ_3 and γ_4 hopping parameters. Panel a) shows the 4 parabolic bands, while panel b) shows a cut along the axis where $k_y = 0$, in which the splitting of the bands by the energy scale γ is marked with a red arrow.

where \mathbf{R}_{sl} is the position of an atom in the sublattice s ($s = A/B$) and layer l , and $|\mathbf{R}_{sl}\rangle$ is the ket associated with the corresponding localised orbital. Here we used the identities $\mathbf{R}_{A1} = \mathbf{R}_{B1} + \mathbf{e}_j$ and $\mathbf{R}_{A2} = \mathbf{R}_{B2} + \mathbf{e}_j$ for the intralayer terms and for the interlayer terms $\mathbf{R}_{A2} = \mathbf{R}_{B1} + c\hat{\mathbf{z}}$, $\mathbf{R}_{A1} = \mathbf{R}_{B2} - \mathbf{e}_j - c\hat{\mathbf{z}}$, $\mathbf{R}_{A1} = \mathbf{R}_{A2} + \mathbf{e}_j - c\hat{\mathbf{z}}$ and $\mathbf{R}_{B1} = \mathbf{R}_{B2} + \mathbf{e}_j - c\hat{\mathbf{z}}$. In this tight binding approximation $t_{sl,s'l'}$ is the energy scale for electrons hopping between the two neighbouring sites \mathbf{R}_{sl} and $\mathbf{R}_{s'l'}$. In bilayer graphene the hopping parameters are given by $t_{A_j,B_j} \equiv t_j = 2.6 \text{ eV}$ with ($j = 1, 2$), [13] $t_{A2,B1} \equiv \gamma = 0.39 \text{ eV}$, [22] $t_{A1,B2} \equiv \gamma_3 = 0.315 \text{ eV}$, [23] and $t_{A1,A2} = t_{B1,B2} \equiv \gamma_4 = 0.044 \text{ eV}$. [24] For the sake of generality, we allow for the interlayer hopping terms t_1 and t_2 to be different. This can be of relevance in supported bilayer samples, where the contact with the substrate may lead to differing hopping energy in one layer with respect to the other.

Electronic eigenstates in bilayer graphene are described by Bloch states of the form

$$|\psi_{\mathbf{k}}\rangle = \sum_{\mathbf{R}_{A1}} u_{\mathbf{k}}^{(A1)} e^{i\mathbf{k}\cdot\mathbf{R}_{A1}} |\mathbf{R}_{A1}\rangle + \sum_{\mathbf{R}_{B1}} u_{\mathbf{k}}^{(B1)} e^{i\mathbf{k}\cdot\mathbf{R}_{B1}} |\mathbf{R}_{B1}\rangle + \sum_{\mathbf{R}_{A2}} u_{\mathbf{k}}^{(A2)} e^{i\mathbf{k}\cdot\mathbf{R}_{A2}} |\mathbf{R}_{A2}\rangle + \sum_{\mathbf{R}_{B2}} u_{\mathbf{k}}^{(B2)} e^{i\mathbf{k}\cdot\mathbf{R}_{B2}} |\mathbf{R}_{B2}\rangle \quad (2.22)$$

where $u_{\mathbf{k}}^{(sl)}$ is the amplitude of the wavefunction in the sublattice s on layer l with wavevector \mathbf{k} . Similarly to the monolayer case, in the 4×4 space of the Bloch amplitudes $(u_{\mathbf{k}}^{(A1)}, u_{\mathbf{k}}^{(B2)}, u_{\mathbf{k}}^{(A2)}, u_{\mathbf{k}}^{(B1)})$

the Hamiltonian takes the matrix form

$$H = \begin{pmatrix} 0 & -\gamma_3 f_{\mathbf{k}} & -\gamma_4 f_{\mathbf{k}}^* & -t_1 f_{\mathbf{k}}^* \\ -\gamma_3 f_{\mathbf{k}}^* & 0 & -t_2 f_{\mathbf{k}} & -\gamma_4 f_{\mathbf{k}} \\ -\gamma_4 f_{\mathbf{k}} & -t_2 f_{\mathbf{k}}^* & 0 & -\gamma \\ -t_1 f_{\mathbf{k}} & -\gamma_4 f_{\mathbf{k}}^* & -\gamma & 0 \end{pmatrix}. \quad (2.23)$$

where $f_{\mathbf{k}} = \sum_{j=1}^3 \exp[i\mathbf{k} \cdot \mathbf{e}_j]$. In the same way as was shown in the case of the monolayer Hamiltonian we can now expand about the Dirac points, which gives the effective Hamiltonian

$$H^{(\tau)} = \tau \begin{pmatrix} 0 & v_3 \hbar k & v_4 \hbar k^* & v_1 \hbar k^* \\ v_3 \hbar k^* & 0 & v_2 \hbar k & v_4 \hbar k \\ v_4 \hbar k & v_2 \hbar k^* & 0 & -\tau \gamma \\ v_1 \hbar k & v_4 \hbar k^* & -\tau \gamma & 0 \end{pmatrix} \quad (2.24)$$

where $\tau = \pm 1$ is the valley index. Here $v_j = 3at_j/2\hbar$ for $j = 1, 2$ and $v_j = 3a\gamma_j/2\hbar$ for $j = 3, 4$. The values of the intralayer group velocities are $v_1 = v_2 = 8 \cdot 10^5 \text{ ms}^{-1}$ while for the interlayer group velocities $v_3 \simeq 10^5 \text{ ms}^{-1}$ and $v_4 \simeq 1.4 \cdot 10^4 \text{ ms}^{-1}$.

Let us first ignore the small γ_3 and γ_4 hopping processes, the effect of the smaller energy hopping processes γ_3 and γ_4 will be discussed in section 2.3.4. Diagonalising $H^{(\tau)}$ above we obtain

$$\epsilon_{\mathbf{k}} = \pm \frac{\gamma}{2} \mp \sqrt{v^2 \hbar^2 |\mathbf{k}|^2 + \frac{\gamma^2}{4}} \quad (2.25)$$

from which we see that the electronic dispersion is made of four bands. Expanding the dispersion of the bands for $v^2 \hbar^2 |\mathbf{k}|^2 / \gamma^2 \ll 1$ and introducing the effective mass $m = \gamma / 2v^2$ we obtain

$$\epsilon_{\mathbf{k}} = \pm \frac{\gamma}{2} \mp \frac{\gamma}{2} \pm \frac{\hbar^2 |\mathbf{k}|^2}{2m}. \quad (2.26)$$

Here we see that two of the four bands touch at $\epsilon_{\mathbf{k}} = 0$ and two are offset by an energy $\epsilon_{\mathbf{k}} = \pm \gamma$ due to the vertical B1-A2 interlayer hopping, as shown in fig 2.7. This electronic dispersion is associated with 2D massive particles with parabolic dispersion, leading to a constant density of states.

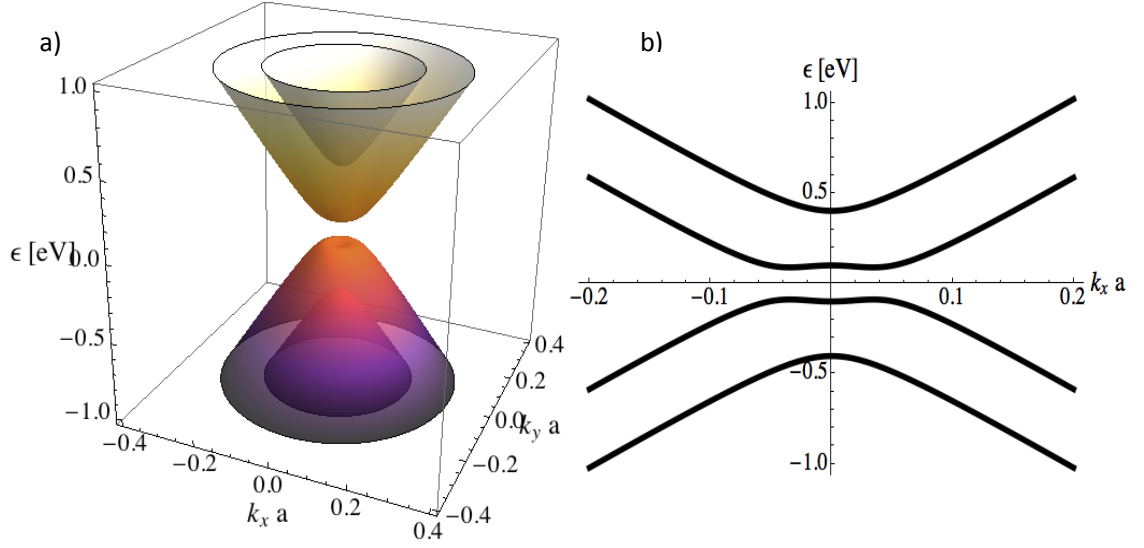


Figure 2.8: The band structure of gapped bilayer graphene, neglecting the γ_3 and γ_4 hopping parameters, with $\Delta = 0.2$ eV. Panel a) shows the 4 parabolic bands in 3D while panel b) shows the same in 2D along the axis where $k_y = 0$. Note the "mexican hat" shaped dispersion at the lowest energy bands.

2.3.1 Band Gap

One of the most promising properties of bilayer graphene for technological applications is the possibility to induce a tuneable band gap.[25] In pristine graphene the gapless spectrum is protected by inversion symmetry of the carbon lattice, as both the A and B sublattices are formed of identical carbon atoms. In bilayer graphene we may break this symmetry with an electric field perpendicular to the bilayer graphene sheet, which creates a different electrostatic potential to be felt by each layer. We parameterise the energy difference between the layers by the energy Δ . This setup can be realised in a transistor device with both a top and a bottom gate.

We can therefore write the full Hamiltonian of the bilayer in a perpendicular electric field as $H^{(\tau)} + H_\Delta$, where

$$H_\Delta = \begin{pmatrix} \frac{\Delta}{2} & 0 & 0 & 0 \\ 0 & -\frac{\Delta}{2} & 0 & 0 \\ 0 & 0 & -\frac{\Delta}{2} & 0 \\ 0 & 0 & 0 & \frac{\Delta}{2} \end{pmatrix} = \frac{\Delta}{2} \tau_z \otimes \sigma_z. \quad (2.27)$$

We can now find the eigenvalues of perpendicularly biased bilayer graphene, using the

Hamiltonian $H^{(\tau)} + H_{\Delta}$, where for simplicity we set $\gamma_3 = \gamma_4 = 0$. The eigenvalues are

$$\epsilon_{\mathbf{k}} = \pm \sqrt{v^2|\mathbf{k}|^2 + \frac{\gamma^2}{2} + \frac{\Delta^2}{4}} \mp \sqrt{v^2|\mathbf{k}|^2\gamma^2 + \frac{\gamma^4}{4} + v^2|\mathbf{k}|^2\Delta^2}. \quad (2.28)$$

This gives the minima of the higher energy bands at the \mathbf{K} point to be $|\epsilon_{\mathbf{k}=0}| = [\gamma^2 + \Delta^2/4]^{1/2}$ and for the lower energy band $|\epsilon_{\mathbf{k}=0}| = |\Delta|/2$. Neglecting γ_3 and γ_4 we find there is a "mexican hat" like electronic dispersion for the low energy section of each band as shown in Fig. 2.8.[21] Experimental studies have observed this gap opening in biased bilayer graphene in transport,[26, 27, 28] infra-red spectroscopy[29] and ARPES experiments.[30]

2.3.2 Effective Low-Energy Theory

The electronic transport properties of bilayer graphene will be primarily concerned with the two lowest energy bands which in the absence of a gap ($\Delta = 0$) touch at zero energy. Therefore it is convenient to create a new effective Hamiltonian which captures the relevant physics of the two low energy bands.[19] We do this by producing an effective 2×2 Hamiltonian in the A1-B2 subspace. This treatment is equivalent to the Schrieffer-Wolf transformation.[31]

We consider the original 4×4 Hamiltonian Eq. 2.24 and we split this into four 2×2 blocks $H_{ij}^{(\tau)}$, with $(i, j \in \{1, 2\})$ where the upper left block $H_{11}^{(\tau)}$ describes the low energy sector. We can introduce the matrix Green's function $G^{(\tau)} = (H^{(\tau)} - \epsilon_{\mathbf{k}}\mathbf{1})^{-1}$, where $\mathbf{1}$ is the identity matrix, and using this we find

$$G^{(\tau)} = (H^{(\tau)} - \epsilon_{\mathbf{k}}\mathbf{1})^{-1} = \begin{pmatrix} H_{11}^{(\tau)} - \epsilon_{\mathbf{k}} & H_{12}^{(\tau)} \\ H_{21}^{(\tau)} & H_{22}^{(\tau)} - \epsilon_{\mathbf{k}} \end{pmatrix}^{-1} = \begin{pmatrix} G_{11}^{(\tau)-1} & H_{12}^{(\tau)} \\ H_{21}^{(\tau)} & G_{22}^{(\tau)-1} \end{pmatrix}^{-1}. \quad (2.29)$$

By matrix inversion we identify $G_{11}^{(\tau)} = [G_{11}^{(\tau)-1}G_{22}^{(\tau)-1} - H_{12}^{(\tau)}H_{21}^{(\tau)}]^{-1}G_{22}^{(\tau)-1}$, and therefore we can obtain $G_{11}^{(\tau)-1} + \epsilon_{\mathbf{k}}\mathbf{1} = H_{11}^{(\tau)} - H_{12}^{(\tau)}G_{22}^{(\tau)}H_{21}^{(\tau)}$. Identifying the Hamiltonian for the low energy sector as $G_{11}^{(\tau)-1} - \epsilon_{\mathbf{k}}\mathbf{1} = H_{\text{eff}}^{(\tau)}$ we can write the eigenvalue equation for this Hamiltonian as

$$H_{\text{eff}}^{(\tau)}|\psi_{\mathbf{k}}\rangle = \epsilon_{\mathbf{k}}|\psi_{\mathbf{k}}\rangle \Rightarrow [H_{11}^{(\tau)} - H_{12}^{(\tau)}G_{22}^{(0)}H_{21}^{(\tau)}]|\psi_{\mathbf{k}}\rangle = \epsilon_{\mathbf{k}}|\psi_{\mathbf{k}}\rangle. \quad (2.30)$$

If we now expand the expression for $H_{\text{eff}}^{(\tau)}$ in the small parameters $\epsilon_{\mathbf{k}}/\gamma$ and Δ/γ , collecting the lowest order non vanishing terms we find

$$H_{\text{eff}}^{(\tau)} = \begin{pmatrix} \frac{\Delta}{2} & v_3 \hbar k \\ v_3 \hbar k^* & -\frac{\Delta}{2} \end{pmatrix} + \frac{1}{\gamma} \begin{pmatrix} 2v_1 v_4 |k|^2 & v_4^2 k^{*2} + v_1 v_2 k^{*2} \\ v_4^2 k^2 + v_1 v_2 k^2 & 2v_2 v_4 |k|^2 \end{pmatrix}. \quad (2.31)$$

This gives the low energy Hamiltonian of bilayer graphene, and will be the Hamiltonian we will focus on when discussing the electronic properties of bilayer graphene for the rest of this work. This effective theory will only be valid up to energies $|\epsilon_{\mathbf{k}}| \leq \gamma/4$.

2.3.3 Massive Dirac Fermions

We can find the electronic eigenstates for bilayer graphene by solving the eigenvalue equation using the low energy effective Hamiltonian shown in Eq. 2.31. For the simplest case in which $v_3 = v_4 = \Delta = 0$ and $v_1 = v_2 = v$ the electronic eigenstates in bilayer graphene for $\tau = +1$ are given by

$$|\psi_{\mathbf{k},s}^{(+)}\rangle = \frac{1}{\sqrt{2}} \begin{pmatrix} 1 \\ s e^{i2\phi_{\mathbf{k}}} \end{pmatrix} e^{i\mathbf{k}\cdot\mathbf{r}} = u_{\mathbf{k},s}^{(+)} e^{i\mathbf{k}\cdot\mathbf{r}} \quad (2.32)$$

where, once again we use $\phi_{\mathbf{k}} = \arctan(k_y/k_x)$, $s = \text{sign}(\epsilon_{\mathbf{k}})$ and where $s = +1$ refers of the upper band (electrons) and $s = -1$ refers to the lower band (holes). Similarly in the $\tau = -1$ valley we find

$$|\psi_{\mathbf{k},s}^{(-)}\rangle = \frac{1}{\sqrt{2}} \begin{pmatrix} 1 \\ -s e^{-i2\phi_{\mathbf{k}}} \end{pmatrix} e^{i\mathbf{k}\cdot\mathbf{r}} = u_{\mathbf{k},s}^{(-)} e^{i\mathbf{k}\cdot\mathbf{r}}. \quad (2.33)$$

While we have disregarded the effects of the v_3, v_4 terms and the bandgap Δ as these eigenstates capture all the important differences between electrons in bilayer graphene as compared to monolayers. The effect of these smaller hopping terms on the form of the electronic eigenstates will be addressed in much more detail in chapter 4.

The two component spinor again refers to a pseudo spin and in the two band form it relates to the relative electron density on the A1 and B2 lattice sites. The parabolic character of the low energy bands leads to a factor two in the exponent of the phase factor in the spinor which means that in contrast to monolayer graphene the pseudo spin winds twice along a closed loop around the Dirac point as shown in Fig 2.4.b. This leads to several important differences in the properties of massive Dirac fermions.

As the pseudo spin winds at twice the rate about the Dirac point, electronic states with opposite momenta will have the same pseudo spin, meaning that the chirality condition can be met for scattering between state with momentum $|\mathbf{k}|$ and $-|\mathbf{k}|$. This means that in complete contrast to the case of monolayer graphene, back scattering is allowed in bilayer systems.

Another important consequence of the increase of the winding of the pseudo spin is on the Berry phase, which in bilayer graphene is 2π , leading to a unique electronic spectrum of Landau levels created in bilayer graphene in a large perpendicular magnetic field.[19]

2.3.4 Trigonal Warping

The inclusion of the smaller energy hopping processes in the tight binding analysis associated with the γ_3 and γ_4 hopping terms leads to new structures arising in the low energy electronic spectrum.[19] In this section we will systematically introduce these new terms and discuss their effects. We work within the effective low-energy two-band Hamiltonian derived in Eq. 2.31. First we introduce the hopping parameter γ_3 related to the hopping between lattice sites of the type A1 and B2, which creates terms linear in momentum and proportional to the group velocity $v_3 = 10^5 \text{ms}^{-1}$. The inclusion of these terms in the Hamiltonian gives

$$H^{(\tau)} = \begin{pmatrix} 0 & v_3 \hbar \mathbf{k} + \frac{\hbar^2 \mathbf{k}^{\dagger 2}}{2m} \\ v_3 \hbar \mathbf{k}^{\dagger} + \frac{\hbar^2 \mathbf{k}^2}{2m} & 0 \end{pmatrix} \quad (2.34)$$

which can be diagonalised to give the electronic dispersion

$$\epsilon_{\mathbf{k}} = \pm \left| v_3 \hbar \mathbf{k}^{\dagger} + \frac{\hbar^2 \mathbf{k}^2}{2m} \right|. \quad (2.35)$$

The two bands touch at zero energy, but in contrast with the $v_3 = 0$ case they now meet at four points in momentum space given by $|\mathbf{k}| = 0$ and $|\mathbf{k}| = 2mv_3/\hbar$ with $\phi = \pi(2n + 1)/3$, where $n = 0, 1, 2$, due to the underlying symmetry of the honeycomb lattice.[32] This creates a new low energy structure characterised by four mini Dirac points around which the dispersion is massless, which are shown in Fig. 2.9. The four cones meet at energy $\epsilon^* = \gamma v_3^2/4v^2 = mv_3/2 \simeq 1.6 \text{meV}$ and at higher energies the spectrum is essentially parabolic.

Interestingly, in this low-energy trigonally warped structure the topology of the Fermi surface changes as a function of carrier density (i.e. the Fermi energy ϵ_F). For $|\epsilon_F| > \epsilon^*$, corresponding to a concentration of electrons (or holes) larger than $(2/\pi^2)(mv_3/\hbar)^2 \simeq 2 \times 10^{10} \text{cm}^{-2}$, the Fermi

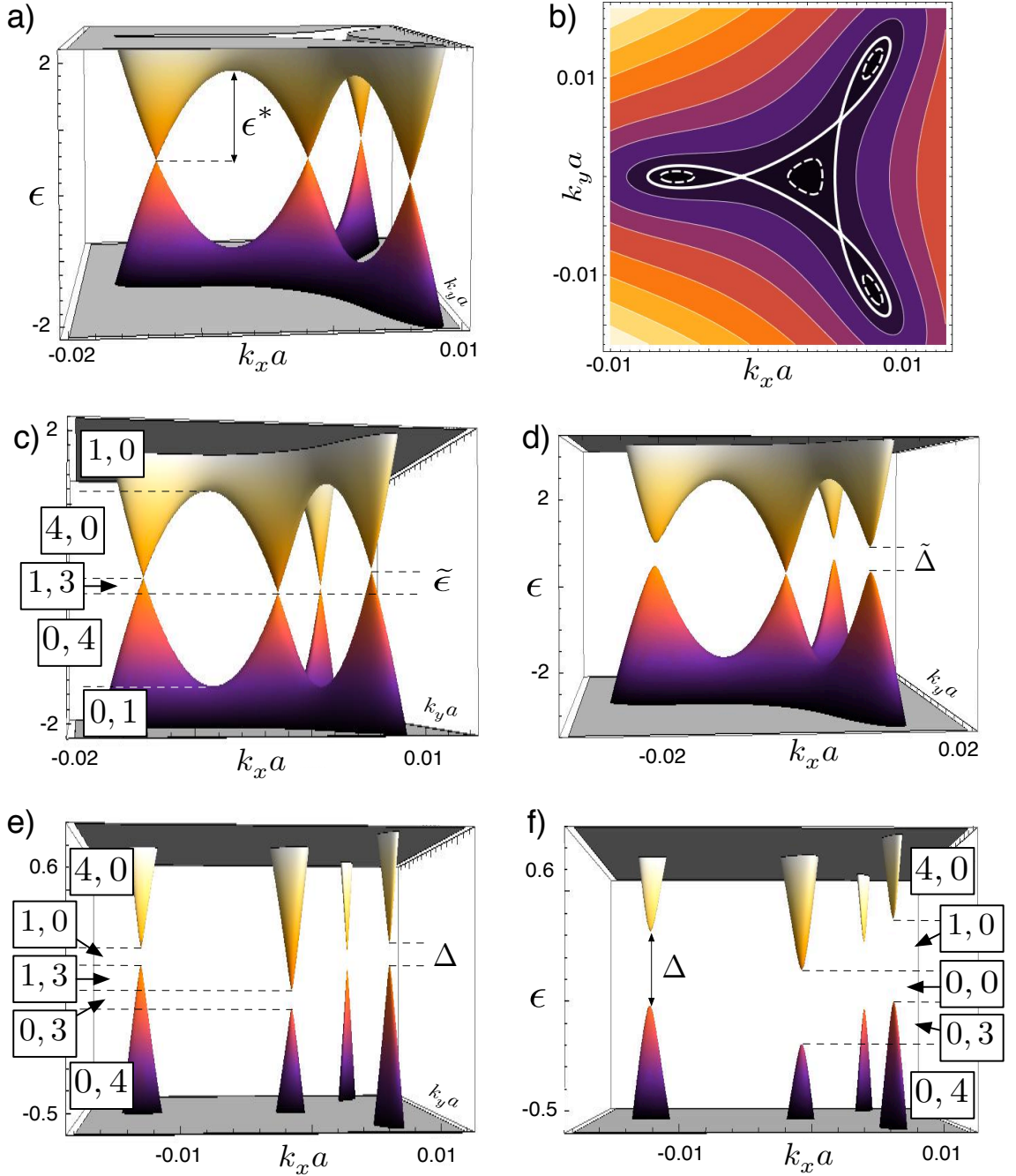


Figure 2.9: Electronic band structure of bilayer graphene. All energy scales ϵ are in meV. Panel a) The low-energy spectrum neglecting terms in v_4 . Four massless cones touch at zero energy. Panel b) Equipotential lines for the panel a). Dashed lines correspond to $\epsilon < \epsilon^*$, yielding four disconnected electron pockets. The thick line corresponds to $\epsilon = \epsilon^*$ where the Lifshitz transition occurs. All other continuous lines are at $\epsilon > \epsilon^*$, yielding a singly connected electron pocket in the Fermi surface. Dark areas correspond to states close to zero energy while light ones are for higher energies. Panel c) Band structure including v_4 . The central Dirac cone touches at zero energy, while the other three touch at $\tilde{\epsilon}$. The boxes $[N_e, N_h]$ in different energy windows indicate that the Fermi surface is made out of N_e electron pockets and N_h hole pockets. Panel d) Same as c), but with asymmetric intralayer velocities, corresponding to $t_2 = t_1/4 = 1$ eV. This large asymmetry is used to stress the formation of the minigaps $\tilde{\Delta}$. Panel e) Magnification of the low energy spectrum in c), but with a small interlayer gap $\Delta < \tilde{\epsilon}$. Panel f) Same as in e), but with a larger interlayer gap $\Delta > \tilde{\epsilon}$.

surface in each valley is connected and topologically equivalent to a circle. At $|\epsilon_F| = \epsilon^*$ a Lifshitz transition occurs[33] and the Fermi surface shows knots that develops into four disconnected electron (hole) pockets at $0 < |\epsilon_F| < \epsilon^*$. In this regime the single-particle density of states vanishes linearly as it approaches zero doping and exhibits a peak due to a Van Hove singularity at the Lifshitz transition, that should lead to observable features, e.g., in compressibility measurements or in the transport properties as a function of the carrier density.

It has to be pointed out that ϵ^* is a rather small energy scale. The physics of the Lifshitz transition can thus be observed only in extremely clean samples at low density, so that the smearing due to disorder does not obscure the pertinent features. An alternative possibility to overcome this difficulty would be to tune the Lifshitz transition to higher energies, which will be discussed in great detail in chapters 3 and 4.

Next in the series of approximations is to include the γ_4 hopping term which creates the terms in the Hamiltonian proportional to the group velocity $v_4 \simeq 1.4 \times 10^4 \text{ ms}^{-1}$, leading to the full Hamiltonian shown in Eq. 2.31 with $\Delta = 0$. This Hamiltonian can be diagonalised and gives the electronic dispersion

$$\epsilon_{\mathbf{k}} = \frac{2v_4}{v} \frac{\hbar^2 |\mathbf{k}|^2}{2m} \pm \left| v_3 \hbar \mathbf{k}^\dagger + \frac{\hbar^2 \mathbf{k}^2}{2m} \left(1 + \frac{v_4^2}{v^2} \right) \right|. \quad (2.36)$$

We see that the main consequence of the v_4 terms is that, while we still find four massless mini Dirac cones at low energy, they no longer meet at the same energy, as shown in Fig. 2.9.c. The four Dirac points are found at $|\mathbf{k}| = 0$, where the bands touch at zero energy, as well as $|\mathbf{k}| = 2mv_3/[\hbar(1+v_4^2/v^2)]$ with $\phi = \pi(2n+1)/3$, where the bands touch at energy $\tilde{\epsilon} = 2\gamma v v_3^2 v_4 / (v^2 + v_4^2)^2 = 4mv_3^2 v_4 / [v(1 + v_4^2/v^2)^2]$. Since $v_4/v \ll 1$, we have $\tilde{\epsilon} \simeq 8\epsilon^* v_4/v \simeq 0.2 \text{ meV}$.

We can explicitly expand the Hamiltonian around the different mini Dirac points, described by the complex momenta k_D , by considering $k = k_D + \delta k$. Around $k_D = 0$ the linearised Hamiltonian is given by

$$H_{\text{eff}}^{(\tau)} \simeq v_3 \hbar \begin{pmatrix} 0 & \delta k \\ \delta k^\dagger & 0 \end{pmatrix} \quad (2.37)$$

and describes massless chiral fermions with Berry phase $-\pi$, due to the clockwise winding of the spinor for an anticlockwise loop of δk . A similar expansion near the outer Dirac cone at the momentum $k_D = -2mv_3/[\hbar(1 + v_4^2/v^2)]$ yields

$$H_{\text{eff}}^{(\tau)} \simeq \tilde{\epsilon} \mathbf{1} - v_3 \hbar \begin{pmatrix} 0 & \tau \delta k_x - 3i \delta k_y \\ \tau \delta k_x + 3i \delta k_y & 0 \end{pmatrix} \quad (2.38)$$

and describes massless Dirac fermions with a Berry phase π and elliptical equipotential lines, notice though that a electron transported in loop enclosing all four massless cone will give a Berry phase 2π . Due to the massless Dirac cones touching at different energies, the density of states will never vanish. For $0 < \epsilon_F < \tilde{\epsilon}$ the Fermi surface will be formed by four pockets, one electron like and three hole like. At energies larger than $\tilde{\epsilon}$ but less than the Lifshitz transition ϵ^* the spectrum remains unaffected. The critical energy at which the Lifshitz transition occurs is slightly renormalised to $\epsilon_+^* \simeq \epsilon^*(1 + 2v_4/v)$ for electron doping and $\epsilon_-^* \simeq -\epsilon^*(1 - 2v_4/v)$ for hole doping.

It is interesting to notice that a finite value of interlayer electric field corresponding to $0 < \Delta \leq \tilde{\epsilon}$ does not induce a global gap in the spectrum, but rather opens a gap in each individual Dirac cone. A global gap opens up only for $\Delta > \tilde{\epsilon}$.

Finally, we can analyse the general case in which v_3 and v_4 are present in Eq. 2.31, with $v_1 \neq v_2$. This can be of relevance for bilayer samples on a substrate, as the latter may induce an asymmetry in the two intralayer hopping energies t_1 and t_2 . In this case, for $\Delta = 0$, the low energy spectrum is given by

$$\epsilon_{\mathbf{k}} = \frac{v_4(v_1 + v_2)}{\gamma} \hbar^2 |\mathbf{k}|^2 \pm \sqrt{\left(\frac{v_4(v_1 - v_2)}{\gamma}\right)^2 \hbar^4 |\mathbf{k}|^4 + \left|v_3 \hbar \mathbf{k}^\dagger + \frac{v_1 v_2 + v_4^2}{\gamma} \hbar^2 \mathbf{k}^2\right|^2}, \quad (2.39)$$

as illustrated in Fig. 2.9.d. The two bands touch only at $|\mathbf{k}| = 0$, where a single massless Dirac point survives while the other three disappear. In the experimentally relevant regime $v_1 - v_2 \ll \sqrt{v_1 v_2} \simeq v$ the spectrum shows the opening of a minigap $\tilde{\Delta} \simeq \tilde{\epsilon} |v_1 - v_2|/v$ at each of the three satellite Dirac points. Notice that no interlayer term Δ is required in order to open these minigaps. As a consequence a new regime appears for $\tilde{\epsilon} - \tilde{\Delta}/2 < \epsilon_F < \tilde{\epsilon} + \tilde{\Delta}/2$, characterised by a Fermi surface comprised of one electron pocket.

2.4 Conclusion

In this chapter we have introduced all the important ideas concerning the electronic properties of graphene that are necessary to understand the rest of the work contained in this thesis. This has included the electronic spectrum of both monolayer and bilayer graphene, and a discussion of the

properties of Dirac fermions. We have paid particular attention to the effect of trigonal warping in bilayer graphene and the unique electronic dispersion it creates. The dramatic effects of strain on the trigonally warped electronic spectrum will be discussed in chapter three while role of trigonal warping on electrical transport will be explored in great detail in chapter four.

Bibliography

- [1] P. R. Wallace, “The band theory of graphite,” *Physical Review*, vol. 71, pp. 622–634, 05 1947.
- [2] J. W. McClure, “Band structure of graphite and de haas-van alphen effect,” *Physical Review*, vol. 108, pp. 612–618, 11 1957.
- [3] J. C. Slonczewski and P. R. Weiss, “Band structure of graphite,” *Physical Review*, vol. 109, pp. 272–279, 01 1958.
- [4] G. W. Semenoff, “Condensed-matter simulation of a three-dimensional anomaly,” *Physical Review Letters*, vol. 53, pp. 2449–2452, 12 1984.
- [5] D. P. Di Vincenzo and E. J. Mele, “Self-consistent effective-mass theory for intralayer screening in graphite intercalation compounds,” *Physical Review B*, vol. 29, pp. 1685–1694, 02 1984.
- [6] F. D. M. Haldane, “Model for a quantum hall effect without landau levels: Condensed-matter realization of the ”parity anomaly”,” *Physical Review Letters*, vol. 61, pp. 2015–2018, 10 1988.
- [7] P. Blake, E. W. Hill, A. H. Castro Neto, K. S. Novoselov, D. Jiang, R. Yang, T. J. Booth, and A. K. Geim, “Making graphene visible,” *Applied Physics Letters*, vol. 91, no. 6, pp. –, 2007.
- [8] K. S. Novoselov, A. K. Geim, S. V. Morozov, D. Jiang, M. I. Katsnelson, I. V. Grigorieva, S. V. Dubonos, and A. A. Firsov, “Two-dimensional gas of massless dirac fermions in graphene,” *Nature*, vol. 438, pp. 197–200, 11 2005.

- [9] M. I. Katsnelson, “Zitterbewegung, chirality, and minimal conductivity in graphene,” vol. 51, no. 2, pp. 157–160, 2006.
- [10] R. Danneau, F. Wu, M. F. Craciun, S. Russo, M. Y. Tomi, J. Salmilehto, A. F. Morpurgo, and P. J. Hakonen, “Shot noise in ballistic graphene,” *Physical Review Letters*, vol. 100, pp. 196802–, 05 2008.
- [11] M. I. Katsnelson, K. S. Novoselov, and A. K. Geim, “Chiral tunnelling and the klein paradox in graphene,” *Nat Phys*, vol. 2, pp. 620–625, 09 2006.
- [12] K. S. Novoselov, Z. Jiang, Y. Zhang, S. V. Morozov, H. L. Stormer, U. Zeitler, J. C. Maan, G. S. Boebinger, P. Kim, and A. K. Geim, “Room-temperature quantum hall effect in graphene,” *Science*, vol. 315, pp. 1379–1379, 03 2007.
- [13] W. W. Toy, M. S. Dresselhaus, and G. Dresselhaus, “Minority carriers in graphite and the h-point magnetoreflexion spectra,” *Physical Review B*, vol. 15, pp. 4077–4090, 04 1977.
- [14] T. Ando, T. Nakanishi, and R. Saito, “Berry’s phase and absence of back scattering in carbon nanotubes,” *J. Phys. Soc. Jpn.*, vol. 67, no. 8, pp. 2857–2862, 1998.
- [15] M. V. Berry, “Quantal phase factors accompanying adiabatic changes,” *Proceedings of the Royal Society of London. A. Mathematical and Physical Sciences*, vol. 392, no. 1802, pp. 45–57, 1984.
- [16] G. P. Mikitik and Y. V. Sharlai, “Manifestation of berry’s phase in metal physics,” *Physical Review Letters*, vol. 82, pp. 2147–2150, 03 1999.
- [17] S. G. Sharapov, V. P. Gusynin, and H. Beck, “Magnetic oscillations in planar systems with the dirac-like spectrum of quasiparticle excitations,” *Physical Review B*, vol. 69, pp. 075104–, 02 2004.
- [18] Y. Zhang, Y. W. Tan, H. L. Stormer, and P. Kim, “Experimental observation of the quantum hall effect and berry’s phase in graphene,” *Nature*, vol. 438, pp. 201–204, 11 2005.
- [19] E. McCann and V. I. Fal’ko, “Landau-level degeneracy and quantum hall effect in a graphite bilayer,” *Physical Review Letters*, vol. 96, pp. 086805–, 03 2006.

- [20] F. Guinea, A. H. Castro Neto, and N. M. R. Peres, “Electronic states and Landau levels in graphene stacks,” *Physical Review B*, vol. 73, pp. 245426–, 06 2006.
- [21] J. Nilsson, A. H. Castro Neto, F. Guinea, and N. M. R. Peres, “Electronic properties of bilayer and multilayer graphene,” *Physical Review B*, vol. 78, pp. 045405–, 07 2008.
- [22] L. G. Johnson and G. Dresselhaus, “Optical properties of graphite,” *Physical Review B*, vol. 7, pp. 2275–2285, 03 1973.
- [23] R. E. Doezema, W. R. Datars, H. Schaber, and A. Van Schyndel, “Far-infrared magnetospectroscopy of the Landau-level structure in graphite,” *Physical Review B*, vol. 19, pp. 4224–4230, 04 1979.
- [24] E. Mendez, A. Misu, and M. S. Dresselhaus, “Magnetoreflexion study of graphite under pressure,” *Physical Review B*, vol. 21, pp. 827–836, 01 1980.
- [25] E. McCann, “Asymmetry gap in the electronic band structure of bilayer graphene,” *Physical Review B*, vol. 74, pp. 161403–, 10 2006.
- [26] J. B. Oostinga, H. B. Heersche, X. Liu, A. F. Morpurgo, and L. M. K. Vandersypen, “Gate-induced insulating state in bilayer graphene devices,” *Nat Mater*, vol. 7, pp. 151–157, 02 2008.
- [27] Y. Zhang, T. T. Tang, C. Girit, Z. Hao, M. C. Martin, A. Zettl, M. F. Crommie, Y. R. Shen, and F. Wang, “Direct observation of a widely tunable bandgap in bilayer graphene,” *Nature*, vol. 459, pp. 820–823, 06 2009.
- [28] L. Jing, J. Velasco Jr., P. Kratz, G. Liu, W. Bao, M. Bockrath, and C. N. Lau, “Quantum transport and field-induced insulating states in bilayer graphene pnp junctions,” *Nano Letters*, vol. 10, pp. 4000–4004, 2013/11/24 2010.
- [29] K. F. Mak, C. H. Lui, J. Shan, and T. F. Heinz, “Observation of an electric-field-induced band gap in bilayer graphene by infrared spectroscopy,” *Physical Review Letters*, vol. 102, pp. 256405–, 06 2009.
- [30] A. Bostwick, T. Ohta, J. L. McChesney, E. K. V., T. Seyller, K. Horn, and E. Rotenberg, “Symmetry breaking in few layer graphene films,” *New Journal of Physics*, vol. 9, no. 10, p. 385, 2007.

-
- [31] J. R. Schrieffer and P. A. Wolff, "Relation between the anderson and kondo hamiltonians," *Physical Review*, vol. 149, pp. 491–492, 09 1966.
- [32] G. P. Mikitik and Y. V. Sharlai, "Electron energy spectrum and the berry phase in a graphite bilayer," *Physical Review B*, vol. 77, pp. 113407–, 03 2008.
- [33] E. M. Lifshitz *Sov. Phys. JETP*, vol. 11, no. 1130, 1960.

3

Electromechanical Properties of Graphene

3.1 Introduction

Graphene is an atomically thin crystalline membrane, in fact it represents the only monoatomic conducting membrane known in nature. Many of the possible technological uses of graphene lie in the area of flexible electronics,[1, 2] which could open the door to an unprecedented level of integration of electronics with everyday objects.[3] As a 2D lattice of carbon atoms, graphene allows for ripples and corrugations out of the 2D plane and therefore to understand these mechanical distortions of graphene it is crucially important to study its properties as a membrane.[4, 5] Indeed one of the most fruitful methods to increase the charge carrier mobility of graphene devices is to create a suspended sample by etching away the substrate supporting the graphene flake.[6, 7, 8] This process leads to a reduction of substrate induced disorder in the sample, but the process induces strain and allows for out-of-plane flexural motion of the suspended graphene lattice, and these effects have important consequences for electronic transport in these systems. Most interestingly on a

fundamental level, deformations of the honeycomb lattice structure lead to changes in bond length between atoms creating a coupling between the mechanical and electronic degrees of freedom. It can be shown that deformations of the graphene lattice induce fictitious gauge fields arising within the electronic Dirac Hamiltonian which are analogous to the gauge fields in a electromagnetic field.[9, 10, 11, 12, 13] These fictitious gauges fields lead to a wealth of observable signatures in electronic transport, ranging from the effect of uniform strain across a sample[14, 15], the role of out-of-plane fluctuations, ripples and local deformations in the graphene membrane leading to an increase of scattering of electrons[13, 16, 17] and Aharanov-Bohm interferences[18], the creation of large pseudo magnetic fields[19, 20] or in some regimes leading to the suppression of weak localisation.[21, 22, 23, 24]

In this chapter we will first provide an introduction to continuum elasticity theory, which will provide the formalism needed to study the electromechanical properties of graphene and introduce a model for 2D membranes. Then we introduce the effect of strain on a monolayer graphene lattice, discussing the fictitious gauge fields which arise from variations of the bond lengths and the deformation potential which arises from dilations of the lattice. We shall discuss the gauge field's effect on the band structure in graphene for common strain configurations and the manifestation of pseudo magnetic fields. Next, we will extend this analysis to study strain effects in a bilayer graphene membrane starting with the fictitious gauge fields which arise from variations of the bond lengths and the deformation potential which arises from dilations of the size of the lattice. In bilayers we study the dramatic effect these fictitious gauges fields have on the low energy electronic spectrum of bilayer graphene which can lead to a complete reconstruction of the electronic spectrum.

3.2 Continuum Elasticity Theory for Two Dimensional Membranes

When a body is deformed, the distance between any two points on the body changes. The displacement of a point initially at position \mathbf{r} due to a deformation is given by the vector $\mathbf{r}' - \mathbf{r}$, where in 2D membrane we write the position of the displaced point \mathbf{r}' as $\mathbf{r}' = \mathbf{r} + \mathbf{u}(\mathbf{r}) + \hat{\mathbf{z}}h(\mathbf{r})$. Here we have introduced the two component vector $\mathbf{u}(\mathbf{r})$ describing in-plane deformations and the scalar function $h(\mathbf{r})$ describing out-of-plane deformations.

If we consider two points close to each other and denote as dx_i the components of the

vector joining them before a deformation, the vector joining them after the deformation is $dx'_i = dx_i + du_i$, where $x_i \in \{x, y\}$ and where u_i contains both in-plane and out-of-plane deformations, $u_i = (u_x(\mathbf{r}), u_y(\mathbf{r}), h(\mathbf{r}))$. Using these quantities we can write the new length between two points under a deformation as

$$dl^{2'} = dl^2 + 2\partial_j u_i dx_i dx_j + \partial_j u_i \partial_l u_i dx_j dx_l \quad (3.1)$$

where $\partial_i \equiv \partial/\partial x_i$ and using the substitution $du_i = \partial_k u_i dx_k$. As in the second term we sum over both indices i and j we may replace $\partial_j u_i dx_i dx_j$ with its more symmetric form $1/2(\partial_j u_i dx_i dx_j + \partial_i u_j dx_j dx_i)$. We thus can write

$$dl^{2'} = dl^2 + 2u_{ij} dx_i dx_j \quad (3.2)$$

where the tensor u_{ij} is defined as

$$u_{ij} = \frac{1}{2}(\partial_i u_j + \partial_j u_i + \partial_i h \partial_j h) . \quad (3.3)$$

This tensor is known as the strain tensor[25] and gives the change in elements of length of the body under deformations, here let $u_l = h(\mathbf{r})$ be the out-of-plane displacement of a 2D membrane. Notice that the strain tensor is symmetric $u_{ij} = u_{ji}$. We also notice that in-plane terms enter the strain tensor linearly while out-of-plane deformations enter quadratically as expected from symmetry considerations.

We now use the strain tensor to build up an understanding of the continuum elasticity theory of 2D membranes. To do this we will construct the elastic Lagrangian density for a 2D membrane. We do this by splitting the problem into two parts, one concerning the stretching of the membrane and another one considering the bending of the membrane

$$\mathcal{L} = \mathcal{L}_{\text{stretch}} + \mathcal{L}_{\text{bend}} . \quad (3.4)$$

First we will look at the contribution arising from stretching of the membrane. We assume the deformations are small with $u_{ij} \ll 1$ and write the free energy as an expansion in powers of u_{ij} , which we may use as the potential in our Lagrangian density. If the internal stress of the membrane is zero then there must be no terms linear in u_{ij} , this also satisfies a symmetry to reflections in the

$x-y$ plane. As the free energy must be a scalar quantity, we consider the lowest order scalar terms which are allowed. Two independent scalars of second order can be formed from the components of the symmetrical strain tensor u_{ij} , the sum of the diagonal components u_{kk}^2 and the sum of the squares of all the components u_{ij}^2 . The term u_{kk}^2 concerns bulk dilations of the membrane, whereas u_{ij}^2 accounts for shear deformations of the membrane.

Therefore including a kinetic energy term we find the stretching Lagrangian density to be

$$\mathcal{L}_{\text{stretch}} = \int d\mathbf{r} \left[\frac{\rho}{2} \dot{\mathbf{u}}^2 - \mu u_{ij}^2 - \frac{\lambda}{2} u_{kk}^2 \right] \quad (3.5)$$

where λ and μ are the Lamé coefficients, which for graphene have typical values $\mu \simeq 4\lambda = 9\text{eV}\text{\AA}^{-2}$ and ρ is the mass density of graphene which has a typical value of $\rho \simeq 7.6 \cdot 10^{-7} \text{kg m}^{-2}$. [26, 27, 28]

Now we turn our attention to the part of the Lagrangian density which concerns itself with out-of-plane motion of a membrane, of which we consider two parts: one that considers the energy cost to bend the membrane and another energy associated with sample specific tension induced at the edges of the sample, typically by the supporting metallic contacts.

The bending energy cost can be calculated by considering the variation of the vector normal to the surface of the membrane. This can be written as

$$\mathbf{n}(\mathbf{r}) = \frac{(-\partial_x h, -\partial_y h, 1)}{\sqrt{1 + (\nabla h)^2}}. \quad (3.6)$$

In a flat graphene configuration all the normal vectors are aligned and therefore $\nabla \mathbf{n}(\mathbf{r}) = 0$. Deviations from the flat configuration require misalignment of the normal vectors with some associated energy cost. We could for instance consider a lattice model by partitioning the membrane into segments such that one can consider the vectors normal to the surface at each lattice site. Upon doing this we may write the free energy as

$$F = -\kappa \sum_{\langle i,j \rangle} \mathbf{n}_i \cdot \mathbf{n}_j \quad (3.7)$$

where κ is the bending energy, \mathbf{n}_i is the normal associated with the i -th segment, and here $\langle \dots \rangle$ represents nearest neighbours. This free energy is analogous to the 2D classical Heisenberg ferromagnet in which the normals act like spin vectors and the bending energy takes the role of the exchange energy.

Looking at the low energy physics we may write this in the continuum limit as

$$F = \frac{1}{2}\kappa \int d\mathbf{r}(\nabla\mathbf{n})^2 . \quad (3.8)$$

By inserting Eq. 3.6 and considering $|\nabla h| \ll 1$ such that we can neglect the denominator in Eq. 3.6 yields

$$F = \frac{1}{2}\kappa \int d\mathbf{r}[(\partial_x^2 h)^2 + 2(\partial_x \partial_y h)^2 + (\partial_y^2 h)^2] = \frac{1}{2}\kappa \int d\mathbf{r}[(\nabla^2 h)^2 - 2\det(\partial_i \partial_j h)] . \quad (3.9)$$

Of the two terms in the final equation of Eq. 3.10 the first corresponds to the mean curvature and the second corresponds to the Gaussian curvature. The Gaussian curvature term will lead to some integral over the edges of the membrane, which will have no effect on the equation of motion of the membrane. This surface integral, due to the Gauss-Bonnet theorem, relates to a topological invariant that is not changed during smooth deformations of the membrane and plays no role unless we consider membranes with a more complex topology than is required for study graphene membranes. Thus we may ignore the Gaussian curvature, and write the free energy as

$$F = \frac{1}{2}\kappa \int d\mathbf{r}(\nabla^2 h)^2 \quad (3.10)$$

where the typical value for the bending energy κ in graphene is $\simeq 1\text{eV}$. [26, 27] The free energy is symmetric under $h \rightarrow -h$ as well under global translations and rotations of the membrane.

The tension induced by the edges of the sample acts as a surface tension which flattens the out-of-plane distortions of the membrane. The energy cost is the sample specific tension Γ multiplied by the change in area, which may be written as

$$F = \Gamma \int d\mathbf{r} \sqrt{g} \quad (3.11)$$

where $g = \det[g_{ij}]$ is the determinant of the metric of the surface describing the membrane. The metric for a 2D membrane is often discussed using what is known as Monge representation in which it takes the form

$$g_{ij} = \begin{pmatrix} 1 + (\partial_x h)^2 & \partial_x h \partial_y h \\ \partial_x h \partial_y h & 1 + (\partial_y h)^2 \end{pmatrix} . \quad (3.12)$$

Therefore within the Monge representation $\sqrt{g} = \sqrt{1 + (\nabla h)^2}$. Inserting this into Eq. 3.11 and again assuming $|\nabla h| \ll 1$ we expand, Eq 3.11 to get

$$F \approx F_0 + \frac{\Gamma}{2} \int d\mathbf{r} (\nabla h)^2. \quad (3.13)$$

Notice that while this free energy still respects the symmetry under $h \rightarrow -h$ as well under global translations, it does not respect the symmetry under global rotations. This is expected, as introducing tension at the edges of the membrane breaks the symmetry with respect to rotations away from the $x - y$ plane.

Including a kinetic energy term and combining Eq 3.10 and Eq 3.13 we find the bending Lagrangian density to be

$$\mathcal{L}_{\text{bend}} = \frac{1}{2} \int d\mathbf{r} \left[\rho \dot{h}^2 - \kappa (\nabla^2 h(\mathbf{r}))^2 - \Gamma (\nabla h(\mathbf{r}))^2 \right]. \quad (3.14)$$

It is energetically favourable for membranes to screen out elastic stress by buckling into the third dimension. Above we saw the close analogy between a membrane and a 2D classical Heisenberg ferromagnet shown in Eq. 3.7. It has been understood for some time that long range order is destroyed at any finite temperature in two dimensional systems. This manifests in the Heisenberg model as spin wave fluctuations which destroy the ferromagnetic phase.[29, 30] Similarly it was shown that any finite temperature will destroy long range crystalline order in a two dimensional membrane, causing the membrane to crumple.[31] However, experimentally graphene membranes are observed in the flat phase at room temperature[7]: what is the source of this contradiction?

If we present the whole elastic Lagrangian density, including both the stretching and bending contributions we find the final Lagrangian density that we will work with

$$\mathcal{L} = \frac{1}{2} \int d\mathbf{r} \left[\rho (\dot{\mathbf{u}}^2 + \dot{h})^2 - 2\mu u_{ij}^2 - \lambda u_{kk}^2 - \kappa (\nabla^2 h(\mathbf{r}))^2 - \Gamma (\nabla h(\mathbf{r}))^2 \right] \quad (3.15)$$

which captures all the physics of mechanical distortions of graphene membranes, and is known as the Lagrangian for a crystalline membrane. This Lagrangian includes a coupling between in-plane deformations and out-of-plane fluctuations via the terms containing the square of the strain tensor, which is not present when only considering the bending Lagrangian density. This coupling to in-plane deformations introduces non-linearities in the out of plane sector. While the quadratic in-plane terms may be integrated out of the partition function of the crystalline membrane problem,

these non-linear terms lead to a renormalisation of the bending rigidity which effectively stiffens the membrane making the fluctuations finite at finite temperature. This mechanism stabilises the flat phase at sufficiently low temperatures.[32, 33, 34]

3.3 Fictitious Gauge Fields in Monolayer Graphene

A generic elastic deformation in a monolayer graphene membrane induces a displacement of the atomic positions which in general results in the modification of bond lengths between neighbouring atoms.[11, 35] The corresponding change in the hopping energies results in corrections to the matrix elements of the 2×2 Hamiltonian $H_0^{(\tau)}$ as shown in Eq. 2.9, yielding a shift of electronic momenta analogous to that stemming from a vector potential. As a result, mechanical deformations translate into fictitious gauge fields in the Dirac Hamiltonian.

We start by considering the effect of the modifications of the bond lengths in graphene within the tight binding model. We do this with the same formalism developed in the earlier sections of this chapter, so in-plane deformations are described by the two-dimensional displacement vector field $\mathbf{u}(\mathbf{r})$, while out-of-plane distortions are associated to the scalar field $h(\mathbf{r})$, so that the atom at position \mathbf{r} is shifted to $\mathbf{r} + \mathbf{u}(\mathbf{r}) + \hat{\mathbf{z}}h(\mathbf{r})$. Therefore in the tight-binding Hamiltonian the hopping term between $|\mathbf{R}_s\rangle$ and $|\mathbf{R}_{s'}\rangle$ undergoes the change $t_{s,s'} \rightarrow t_{s,s'} + \delta t_{s,s'}$. Here we write $\delta t_{s,s'} \simeq (\partial t_{s,s'} / \partial l_{s,s'}) \delta l_{s,s'}$ with $\delta l_{s,s'} = |\mathbf{R}_{s'} - \mathbf{R}_s + \mathbf{u}(\mathbf{R}_{s'}) - \mathbf{u}(\mathbf{R}_s) + \hat{\mathbf{z}}[h(\mathbf{R}_{s'}) - h(\mathbf{R}_s)]| - |\mathbf{R}_{s'} - \mathbf{R}_s|$ being the variation of the corresponding bond length. This derivative in monolayer graphene is estimated to be $\partial t_{s,s'} / \partial l_{s,s'} = \partial t / \partial a = t/a \partial \ln t / \partial \ln a$, where $\partial \ln t / \partial \ln a$ is the electron Grüneisen parameter describing the dependence of the nearest neighbour hopping on the interatomic distance and is numerically calculated as $\partial \ln t / \partial \ln a \simeq -3$. [9]

We now perform a Bloch band analysis of the deformation-induced corrections to the tight binding problem which allows us to obtain the contribution to the electronic Hamiltonian associated with elastic distortions. The correction to the Hamiltonian will be

$$\delta H = - \sum_{j=1}^3 \frac{\partial t}{\partial a} \delta l |\mathbf{R}_B\rangle \langle \mathbf{R}_B + \mathbf{e}_j| + h.c. . \quad (3.16)$$

We can now obtain δl , and assuming that the deformations are small with respect to the lattice spacing a we may write

$$\delta l = \frac{1}{a} e_j^\alpha (u_\alpha(\mathbf{R}_B + \mathbf{e}_j^\beta) - u_\alpha(\mathbf{R}_B)) + \frac{1}{2a} (h(\mathbf{R}_B + \mathbf{e}_j^\beta) - h(\mathbf{R}_B))^2 \quad (3.17)$$

where e_j^α is the α -th component of the nearest neighbour vector \mathbf{e}_j , with indices $\alpha, \beta \in \{x, y\}$ and again the Einstein summation convention is implied. We now expand the function δl about the position \mathbf{R}_B which for the in-plane displacements gives

$$u_\alpha(\mathbf{R}_B + \mathbf{e}_j^\beta) \simeq u_\alpha(\mathbf{R}_B) + \partial_\beta u_\alpha(\mathbf{R}_B) e_j^\beta \quad (3.18)$$

and similarly for the out-of-plane displacements

$$h(\mathbf{R}_B + \mathbf{e}_j^\beta) \simeq h(\mathbf{R}_B) + \partial_\beta h(\mathbf{R}_B) e_j^\beta. \quad (3.19)$$

Now we take the first order correction to the Hamiltonian using the wave function on each sublattice given by

$$|\psi_{\mathbf{k}}^{(A)}\rangle = \sum_{\mathbf{R}_A} e^{i\mathbf{K}_\tau \cdot \mathbf{R}_A} |\mathbf{R}_A\rangle, \quad |\psi_{\mathbf{k}}^{(B)}\rangle = \sum_{\mathbf{R}_B} u_{\mathbf{k}}^{(B)} e^{i\mathbf{K}_\tau \cdot \mathbf{R}_B} |\mathbf{R}_B\rangle. \quad (3.20)$$

For example when considering the correction to hopping from an A sublattice site to a B sublattice site, we find

$$\langle \psi_{\mathbf{k}}^{(B)} | \delta H | \psi_{\mathbf{k}}^{(A)} \rangle = - \sum_{j=1}^3 \frac{\partial t}{\partial a} \delta l e^{i\mathbf{K}_\tau \cdot \mathbf{e}_j}. \quad (3.21)$$

Now we can expand out the summation across the indices and find the correction in terms of displacement fields using Eq 3.17, Eq. 3.18 and Eq. 3.19. This yields

$$\langle \psi_{\mathbf{k}}^{(B)} | \delta H | \psi_{\mathbf{k}}^{(A)} \rangle = \sum_{j=1}^3 e_j^\alpha e_j^\beta \partial_\beta u_\alpha e^{i\mathbf{K}_\tau \cdot \mathbf{e}_j} = M_{\alpha\beta}^{(\tau)} \partial_\beta u_\alpha \quad (3.22)$$

with $M_{\alpha\beta}^{(\tau)} = \sum_{j=1}^3 e_j^\alpha e_j^\beta \exp[i\mathbf{K}_\tau \cdot \mathbf{e}_j]$ which gives $M_{yy}^{(\tau)} = -M_{xx}^{(\tau)} = 3a^2/4$ and $M_{xy}^{(\tau)} = M_{yx}^{(\tau)} = i\tau 3a^2/4$. This leads to the final result, which we may write in terms of components of the strain tensor as

$$F^{(\tau)} = \frac{3a}{4} \frac{\partial t}{\partial a} (u_{yy} - u_{xx} + i\tau 2u_{xy}). \quad (3.23)$$

Calculating the entire correction to the matrix Hamiltonian including $F^{(\tau)}$ we obtain

$$H_0^{(\tau)} + \delta H^{(\tau)} = \begin{pmatrix} 0 & v\hbar k^\dagger + F^{(\tau)\dagger} \\ v\hbar k + F^{(\tau)} & 0 \end{pmatrix} \quad (3.24)$$

with $k = \tau k_x + ik_y$. The form of the corrections due to changes in bond lengths then appears to be analogous to a vector potential created by an electromagnetic field. We call terms of this type fictitious gauge fields. We find that the fictitious gauge field $F^{(\tau)}$ couples linearly to in-plane deformations, whereas the symmetry with respect to the x-y plane causes the coupling to out-of-plane deformations to be quadratic. The electronic Hamiltonians for each valley are related by the time reversal symmetry $H^{(+)} = H^{(-)\dagger}|_{k \rightarrow -k}$ just as in the case without lattice deformations as elastic deformation will not break time invariance, this distinguishes the fictitious gauge field from a real electromagnetic field which in general will not respect this symmetry between the valleys.

3.3.1 Deformation Potential

Additionally deformations of the membrane couple to the electronic degrees of freedom due to local changes of area. This effect is known as the deformation potential. As this potential arises due to local dilations and contractions in area it takes the form of the scalar potential

$$D(\mathbf{r}) = g\text{Tr}[u_{ij}] = g(u_{xx} + u_{yy}) \quad (3.25)$$

and appears in the diagonal element of the matrix Hamiltonian. We need to estimate the energy scale of the coupling constant g , which we will do using the following argument with the nearly free electron model.[11]

We consider a square area $a \times a$. If the membrane is subjected to a deformation the area changes from S to $S + \delta S(\mathbf{r})$ where $\delta S(\mathbf{r}) = a^2(u_{xx} + u_{yy})$. Therefore we can say that the ion density locally changes from n_0 to $n_0[1 - (u_{xx} + u_{yy})]$. Now we assume the electron density will change in such a way as to minimise the energy by meeting the charge neutrality condition. Considering the potential energy of a two dimensional electron gas $\delta\epsilon(\mathbf{r})$ which corresponds to a density change it satisfies the relation $\delta\epsilon(\mathbf{r})\nu(\epsilon_F) = n_0(u_{xx} + u_{yy})$, where $\nu(\epsilon_F)$ is the density of states at the Fermi level. For a two dimensional electron gas we may write $n_0 = \nu(\epsilon_F)\epsilon_F$. This gives

$$\delta\epsilon(\mathbf{r}) = \epsilon_F(u_{xx} + u_{yy}) \quad (3.26)$$

and by comparing Eq. 3.25 and Eq. 3.26 we may equate $g = \epsilon_F$ where ϵ_F is measured from the bottom of the valence band formed by the σ bands. In graphene the bare value of g is estimated to be around 20 – 30eV. This coupling constant is reduced by screening so that it effectively depends on the electron density.[36, 37] In contrast, the fictitious gauge fields are not affected by screening.[38] As a result, one expects that the vector potential dominates in (significantly strongly) doped graphene, while the deformation potential would be dominant in the immediate vicinity of the Dirac point.

3.3.2 Monolayer Graphene Band Structure With Deformations

The introduction of the fictitious gauge fields into the electronic Dirac Hamiltonian due to distortions of the lattice leads to consequences in the electronic spectrum which gives measurable effects in transport properties of graphene.

For instance the simplest deformation that can be considered is uniaxial in-plane strain along a direction $\hat{\theta} = (\cos \theta, \sin \theta)$ and is described by the vector $\mathbf{u}(\mathbf{r}) = \beta_{\parallel} r_{\parallel} \hat{\theta} + \beta_{\perp} r_{\perp} \hat{\theta}_{\perp}$ with $r_{\parallel} = \mathbf{r} \cdot \hat{\theta}$, $r_{\perp} = \mathbf{r} \cdot \hat{\theta}_{\perp}$ and $\hat{\theta}_{\perp} = \hat{z} \times \hat{\theta}$. Here β_{\parallel} and β_{\perp} represent the values of the strain along the two principal directions. Uniaxial strain represents one of the most common deformations that would be expected in a suspended graphene device, due either to out-of-plane displacement due to capacitive coupling to a back gate or strain induced by the device fabrication techniques. This distortion will create a uniform deformation potential which can be reabsorbed in a global shift of the zero energy. The corresponding gauge field for this strain is $F^{(\tau)} = 3a/4(\partial t/\partial a)(\beta_{\parallel} - \beta_{\perp}) \exp[-i\tau 2\theta]$. Introducing this term into the electronic Dirac Hamiltonian causes the position of the Dirac points to move in momentum space. Notice that in each valley the Dirac point will shift in opposite directions, with two Dirac points moving towards each other in momentum space. Therefore there exists a critical value of strain at which point the two Dirac points will meet and annihilate, creating a gapped electronic spectrum triggering a quantum phase transition from a semi-metal to a semiconductor.[39, 40, 41] Works by different authors suggest that this critical strain is quite large, of the order of 20%, although the critical value will depend of the crystallographic direction the strain is applied in. We could also consider a deformation consisting of pure in-plane shear of amplitude ζ which can be described by an in-plane deformation vector of $\mathbf{u}(\mathbf{r}) = \zeta r_{\parallel} \hat{\theta}_{\perp}$. This results in no contribution from the deformation potential as there is no change in area in a pure shear distortion and gives the resulting gauge field $F^{(\tau)} = 3a/4(\partial t/\partial a)i\zeta\tau \exp[-i\tau 2\theta]$. From this

we conclude that it is hard to open a gap in monolayer graphene with uniaxial strain due to the large strain needed which reaches values close to the elastic limit of graphene. We will see that in bilayer graphene much smaller strain is needed to cause dramatic modifications to the band structure.

3.3.3 Pseudo Magnetic Fields

The most dramatic effect of strain in graphene is the appearance of pseudo magnetic fields. This effect occurs when we consider fictitious gauge fields with a non-zero curl, which is analogous to real magnetic fields in graphene and leads to the creation of Landau levels in the electronic spectrum. The striking difference between real magnetic fields and pseudo magnetic fields is that pseudo magnetic fields do not break time reversal symmetry. In the valley \mathbf{K}' the sign of the effective magnetic field is opposite to that in the valley \mathbf{K} . This means that locally displacements of the atoms can break time reversal symmetry at each valley, but globally over the whole Brillouin zone time reversal symmetry is protected. Indeed, scanning tunnelling microscopy measurements of strained bubbles formed when depositing graphene on a platinum substrate show pseudo magnetic fields as large as 300T as is shown in fig 3.1.[20]

At this point the question naturally becomes what realistic strain distributions can be experimentally created which induce large pseudo magnetic fields, and ideally might allow for tuneable control of the strain. It has been shown that, due to the underlying trigonal crystal symmetry of the lattice, a trigonal in-plane strain configuration will give rise to a uniform pseudo magnetic field which could easily reach 10T.[19] Additionally there have been suggestions for strain configurations made of in-plane shear fan like deformation which lead to a uniform pseudo magnetic field.[42] As pseudo magnetic fields do not break time reversal symmetry the formed Landau levels have been predicted to host distinct many-body states from Landau levels in real magnetic fields with unusual topological phases at certain filling factors.[43]

3.4 Fictitious Gauge Fields in Bilayer Graphene

Bilayer graphene has more mechanical degrees of freedom as the lattice is made of two layers. As we will see in this section this leads to fictitious gauge fields with a far richer structure than in the case of monolayer graphene.

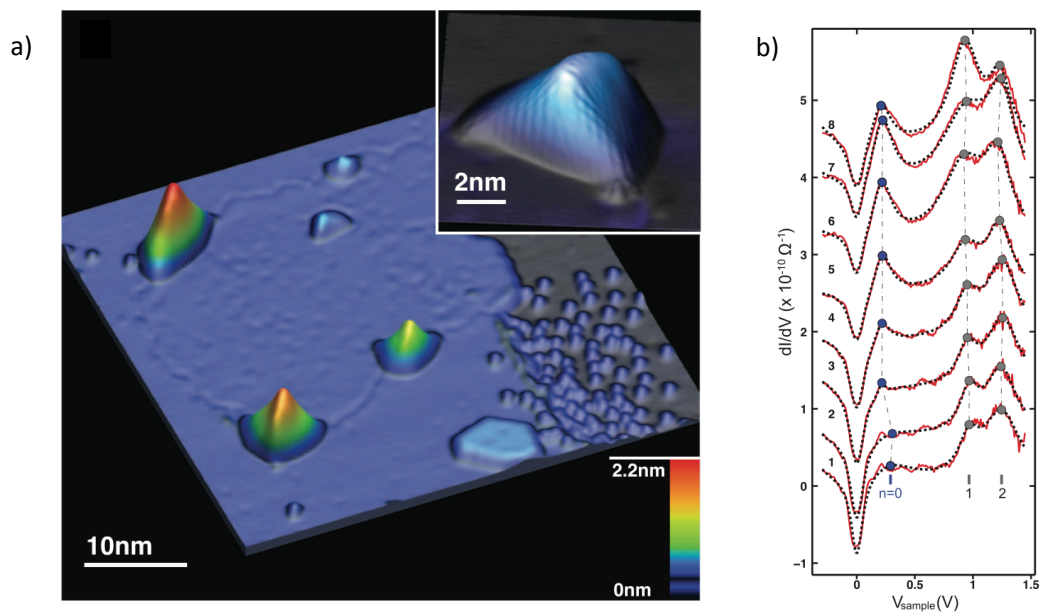


Figure 3.1: Scanning tunnelling microscopy measurements on graphene nano bubbles. Panel a) shows a Scanning tunnelling microscope image of the formation of nano bubbles in a graphene monolayer on a Pt(111) surface which locally strain the graphene the colour scale indicates the vertical displacement of the graphene, the insert shows a high resolution image of one nano bubble and the distorted honeycomb lattice resulting from strain in the bubble. Panel b) shows a sequence of eight dI/dV spectra taken across the a graphene nano bubble at $T \approx 7.5\text{K}$, this measures the local density of state revealing the Landau levels. Adapted from Levy et al, Science 329 (2010)[20]

Following the same formalism that was used to analyse the monolayer graphene problem, we consider a generic elastic deformation in the bilayer graphene membrane which induces a displacement of the atomic positions which in general results in the modification of bond lengths between neighbouring atoms. The corresponding change in the hopping energies results in corrections to the matrix elements of the 4×4 Hamiltonian $H_0^{(\tau)}$ in Eq. 2.32, yielding a shift of electronic momenta analogous to that stemming from a vector potential. As a result, mechanical deformations translate into fictitious gauge fields in the Dirac Hamiltonian.

In order to calculate the gauge fields, we analyse the shift of the atomic positions under a generic distortion. In-plane deformations in layer l are described by a two-dimensional vector field $\mathbf{u}^{(l)}(\mathbf{r})$, while out-of-plane (flexural) distortions are associated to a scalar field $h^{(l)}(\mathbf{r})$, so that the atom at position \mathbf{r} is shifted to $\mathbf{r} + \mathbf{u}^{(l)}(\mathbf{r}) + \hat{\mathbf{z}}h^{(l)}(\mathbf{r})$. Thus, in the tight-binding Hamiltonian, the hopping term between $|\mathbf{R}_{sl}\rangle$ and $|\mathbf{R}_{s'l'}\rangle$ undergoes the change $t_{sl,s'l'} \rightarrow t_{sl,s'l'} + \delta t_{sl,s'l'}$. Here $\delta t_{sl,s'l'} \simeq \left(\partial t_{sl,s'l'}/\partial \ell_{sl,s'l'}\right) \delta \ell_{sl,s'l'}$, with $\delta \ell_{sl,s'l'} = |\mathbf{R}_{s'l'} - \mathbf{R}_{sl} + \mathbf{u}^{(l)}(\mathbf{R}_{s'l'}) - \mathbf{u}^{(l)}(\mathbf{R}_{sl}) + \hat{\mathbf{z}}[h^{(l)}(\mathbf{R}_{s'l'}) - h^{(l)}(\mathbf{R}_{sl})]| - |\mathbf{R}_{s'l'} - \mathbf{R}_{sl}|$ the variation of the corresponding bond length. Among the derivatives $\partial t_{sl,s'l'}/\partial \ell_{sl,s'l'}$ only two are known, the intra-layer $\partial t_{Al,Bl}/\partial \ell_{Al,Bl} \simeq -3 t_{Al,Bl}/\ell_{Al,Bl}$ and the interlayer $\partial t_{A1,B2}/\partial \ell_{A1,B2} \simeq -6.7 \gamma_3/\tilde{c}$. [44] For all the other cases we will assume typical values $\partial t_{sl,s'l'}/\partial \ell_{sl,s'l'} \simeq -\eta_{sl,s'l'} t_{sl,s'l'}/\ell_{sl,s'l'}$, with $\eta_{sl,s'l'}$ the electron Grüneisen parameter to be of order one, the same order as observed for other carbon carbon bonds. Performing the Bloch band analysis of the deformation-induced corrections to the tight binding problem, we can thus obtain the Hamiltonian associated to elastic distortions. For this purpose it is convenient to introduce symmetric (S) and antisymmetric (A) combinations of the deformations in the two layers as follows

$$\begin{aligned} \mathbf{u}^{(S/A)}(\mathbf{r}) &= \frac{\mathbf{u}^{(2)}(\mathbf{r}) \pm \mathbf{u}^{(1)}(\mathbf{r})}{2} \\ h^{(S/A)}(\mathbf{r}) &= \frac{h^{(2)}(\mathbf{r}) \pm h^{(1)}(\mathbf{r})}{2}, \end{aligned} \quad (3.27)$$

where the upper/lower sign is associated with the symmetric/antisymmetric channel. In terms of these modes, and using a long-wavelength expansion of the variation of the bond lengths $\delta \ell_{sl,s'l'}$, we deduce the corrections to the Hamiltonian in the two valleys ($\tau = \pm$) in the Dirac matrix

formalism as

$$\delta H^{(\tau)} = \begin{pmatrix} D_1 & F_3^{(\tau)} & F_4^{(\tau)\dagger} & F_1^{(\tau)\dagger} \\ F_3^{(\tau)\dagger} & D_2 & F_2^{(\tau)} & F_4^{(\tau)} \\ F_4^{(\tau)} & F_2^{(\tau)\dagger} & D_2 & F_\gamma^{(\tau)} \\ F_1^{(\tau)} & F_4^{(\tau)\dagger} & F_\gamma^{(\tau)} & D_1 \end{pmatrix} \quad (3.28)$$

with

$$\begin{aligned} D_{l=1,2} &= g \operatorname{Tr}[u_{ij}^{(l)}] \\ F_{l=1,2}^{(\tau)} &= \frac{3}{4} a \frac{\partial t_l}{\partial a} \left[u_{xx}^{(l)} - u_{yy}^{(l)} - i\tau (u_{xy}^{(l)} + u_{yx}^{(l)}) \right] \\ F_3^{(\tau)} &= \frac{3}{2\tilde{c}} \frac{\partial \gamma_3}{\partial \tilde{c}} \mathcal{F}[\mathbf{u}^{(S)}, \mathbf{u}^{(A)}, h^{(S)}, h^{(A)}] \\ F_4^{(\tau)} &= \frac{3}{2\tilde{c}} \frac{\partial \gamma_4}{\partial \tilde{c}} \mathcal{F}[\mathbf{u}^{(S)}, -\mathbf{u}^{(A)}, -h^{(S)}, h^{(A)}] \\ F_\gamma &= -2 \frac{\partial \gamma}{\partial c} \left[h^{(A)} + \frac{\mathbf{u}^{(A)2}}{c} \right]. \end{aligned} \quad (3.29)$$

Here $u_{ij}^{(l)} = (\partial_i u_j^{(l)} + \partial_j u_i^{(l)} + \partial_i h^{(l)} \partial_j h^{(l)})/2$ is the strain tensor of a two-dimensional membrane in layer l and, in lowest order in the deformation fields, we find

$$\begin{aligned} \mathcal{F}[\mathbf{u}^{(S)}, \mathbf{u}^{(A)}, h^{(S)}, h^{(A)}] &= ac \left(\partial_y h^{(S)} - i\tau \partial_x h^{(S)} \right) \\ &+ \frac{a^2}{2} \left(\partial_x u_x^{(S)} - \partial_y u_y^{(S)} - i\tau (\partial_x u_y^{(S)} + \partial_y u_x^{(S)}) \right) \\ &+ 2a \left(u_y^{(A)} - i\tau u_x^{(A)} \right). \end{aligned} \quad (3.30)$$

Thus the correction terms in the two valleys $\tau = \pm$ are related by the symmetry $\delta H^{(-)} = \delta H^{(+)*}$. In Eq. 3.28 we also introduced the term D_l representing the deformation potential for the layer l associated with local variation of areas in a distorted elastic medium, [11] with g the deformation potential coupling constant. We treat the coupling constant g in the same manner as in the case of deformations in monolayer graphene in section 3.3.1, therefore again it will be affected by screening and its value depends on the electron density.[36, 37]

The terms $F_{l=1,2}^{(\tau)}$ are the same as those appearing in monolayer graphene, discussed in section 3.3. They are linear in the in-plane deformations which cause variations in the bond-lengths. However, the symmetry with respect to the $x - y$ plane forces the coupling with out-of-plane deformations to be quadratic.

In contrast, in the terms $F_3^{(\tau)}$ and $F_4^{(\tau)}$ it is interesting to notice the appearance of a linear

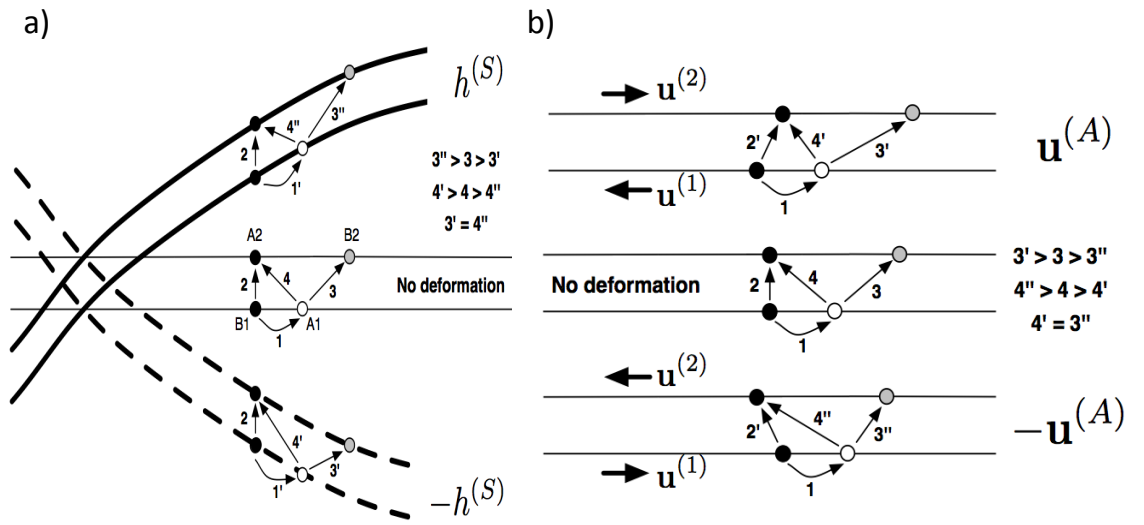


Figure 3.2: Schematic description of the effect of deformations on bond lengths. This side view, taken along the direction \mathbf{e}_j , shows the atoms involved in intra and interlayer hopping processes in a unit cell. Panel a) Bilayer under flexural deformations $h^{(S)}$ and $-h^{(S)}$. The difference between the hopping lengths $3'$ and $3''$ (as well as between $4'$ and $4''$) breaks the symmetry with respect to the plane and is responsible for the appearance of a linear coupling with $h^{(S)}$ in the gauge field $F_3^{(\tau)}$ (and $F_4^{(\tau)}$). The fact that $3' = 4''$ leads to the symmetry $h^{(S)} \rightarrow -h^{(S)}$ between $F_3^{(\tau)}$ and $F_4^{(\tau)}$. Panel b) same as in a), but for in-plane antisymmetric deformations $\mathbf{u}^{(A)}$ and $-\mathbf{u}^{(A)}$. The equality $4' = 3''$ accounts for the symmetry $\mathbf{u}^{(A)} \rightarrow -\mathbf{u}^{(A)}$ between $F_3^{(\tau)}$ and $F_4^{(\tau)}$.

coupling between electrons and symmetric flexural deformations ($h^{(S)}$) for the skewed interlayer hopping terms ($A1 - A2$, $B1 - B2$ and $A1 - B2$). This linear coupling in bilayers seems counterintuitive, but it can be understood by considering the bond lengths involved in the interlayer hopping terms different from the "vertical" $B1 - A2$ one. In Fig. 3.2 the interlayer skewed bonds are illustrated under a generic $h^{(S)}$ (and $-h^{(S)}$) deformation. The two are evidently different, due to the shift between the projected positions of the atoms involved. The analysis of the figure also reveals why the $F_3^{(\tau)}$ and $F_4^{(\tau)}$ terms differ by the replacements $h^{(S)} \rightarrow -h^{(S)}$ and $\mathbf{u}^{(A)} \rightarrow -\mathbf{u}^{(A)}$, as these preserve the bond lengths involved in the corresponding hopping terms.

A long wavelength antisymmetric flexural deformation $h^{(A)}$ corresponds to a local modulation of the interlayer distance which however preserves the structure of Bernal stacking. Its only effect is thus to induce a numerical renormalisation of the velocities v_3 and v_4 . In Eq. (3.30) this would lead to a sub-leading correction $\delta\mathcal{F} = (2ac)h^{(A)}(\tau k_x + ik_y)$ which can however be neglected.

Finally, as far as the term F_γ is concerned, it is associated with the vertical interlayer hopping $B1 - A2$, which does not involve any skewed bond. As a consequence it is not affected by symmetric deformations $h^{(S)}$ and $\mathbf{u}^{(S)}$. The variation of the bond length stems uniquely from antisymmetric deformations. It is linear in the flexural distortions ($h^{(A)}$) and quadratic in the in-plane ones ($\mathbf{u}^{(A)}$).

The 4×4 Hamiltonians $H_0^{(\tau)}$ and $\delta H^{(\tau)}$ in Eq. 2.25, and 3.28 contain the complete information concerning the properties of electrons and of their coupling to elastic deformations. We now wish to produce the low-energy effective theory which describes only the two lowest energy bands. To do this we follow the same procedure as outlined in section 2.3.2 and Ref. [45, 46] producing an effective 2×2 Hamiltonian in the $A1 - B2$ subspace and for complete clarity we briefly outline the scheme again. We consider the 4×4 original Hamiltonian $H^{(\tau)} = H_0^{(\tau)} + \delta H^{(\tau)}$ as made of four 2×2 blocks $H_{ij}^{(\tau)}$, ($i, j \in \{1, 2\}$) with the upper left block $H_{11}^{(\tau)}$ describing the low energy sector. We introduce the matrix Green's function $G^{(\tau)} = (H^{(\tau)} - \epsilon_{\mathbf{k}}\mathbf{1})^{-1}$, with $\mathbf{1}$ the unit matrix, and by direct matrix inversion we get $G_{11}^{(\tau)} = (H_{11}^{(\tau)} - \epsilon_{\mathbf{k}}\mathbf{1} - H_{12}^{(\tau)}(H_{22}^{(\tau)} - \epsilon_{\mathbf{k}}\mathbf{1})^{-1}H_{21}^{(\tau)})^{-1}$. Thus the effective low energy Hamiltonian is obtained as $H_{\text{eff}}^{(\tau)} = \epsilon_{\mathbf{k}}\mathbf{1} + G_{11}^{(\tau)-1} \simeq H_{11}^{(\tau)} - H_{12}^{(\tau)}(H_{22}^{(\tau)})^{-1}H_{21}^{(\tau)}$ in the limit $\epsilon_{\mathbf{k}} \ll \gamma$. By keeping only the lowest non-vanishing order in $F_j^{(\tau)}/\gamma \ll 1$ and $D_l/\gamma \ll 1$, we obtain the effective low-energy Hamiltonian

$$H_{\text{eff}}^{(\tau)} = \begin{pmatrix} \mathcal{D} + \mathcal{A} + \frac{\Delta}{2} & v_3 P_3^{(\tau)} \\ v_3 P_3^{(\tau)\dagger} & \mathcal{D} - \mathcal{A} - \frac{\Delta}{2} \end{pmatrix} + \frac{1}{\gamma} \begin{pmatrix} v_1 v_4 (P_4^{(\tau)\dagger} P_1^{(\tau)} + P_1^{(\tau)\dagger} P_4^{(\tau)}) & v_4^2 (P_4^{(\tau)\dagger})^2 + v_1 v_2 P_1^{(\tau)\dagger} P_2^{(\tau)\dagger} \\ v_4^2 (P_4^{(\tau)})^2 + v_1 v_2 P_2^{(\tau)} P_1^{(\tau)} & v_2 v_4 (P_2^{(\tau)} P_4^{(\tau)\dagger} + P_4^{(\tau)} P_2^{(\tau)\dagger}) \end{pmatrix}. \quad (3.31)$$

Here we introduced the kinetic momenta $P_j^{(\tau)} = \hbar k + F_j^{(\tau)}/v_j$ for $j \in \{1, \dots, 4\}$ as well as the symmetric and antisymmetric components of the deformation potential, $\mathcal{D} = (D_1 + D_2)/2$ and $\mathcal{A} = (D_1 - D_2)/2$, corresponding to a different variation of areas between the two layers.

In the effective Hamiltonian above we also included an on-site energy difference Δ between the two layers describing the effect of an interlayer electric field. This term, together with the antisymmetric component of the deformation potential \mathcal{A} has the physical effect of inducing a gap in the electronic spectrum. It is interesting to see that such a gap is in principle realisable, without any inter-layer electric field, under different variation of local areas for the two layers. Finally, as the term F_γ yields a small correction to the hopping energy γ , it affects the high energy bands but produces only sub-leading corrections to the low energy spectrum, which are neglected in the effective Hamiltonian (3.31).

The energy corrections $F_j^{(\tau)}$ in the kinetic momentum $P_j^{(\tau)}$ thus act as fictitious gauge fields on the electronic orbital degrees of freedom. The symmetry $H_{\text{eff}}^{(-)} = H_{\text{eff}}^{(+)*} \Big|_{k \rightarrow -k}$, together with $F_j^{(-)} = F_j^{(+)*}$ reveals that the fictitious gauge fields are opposite in the two valleys, as in the monolayer case. As a consequence, the fictitious magnetic field generated by a generic elastic deformation is also opposite in the two valleys, as requested by the fact that elastic deformations do not break time-reversal invariance.

3.5 Bilayer Graphene Band Structure With Deformations

In the presence of generic elastic deformations of the lattice, the induced fictitious gauge fields modify the electronic low-energy Hamiltonian as in Eq. (3.31). While our formalism allows us to treat arbitrary distortions, as a first application we consider specific lattice deformations which lead to uniform fictitious gauge fields. As we now show, these induce a shift in the electronic momenta that result in dramatic modifications to the band structure. The massless Dirac cones at low energy are shifted by deformations until they annihilate at a critical value of strain. This critical value of strain will be much smaller than is needed to open a gap in monolayer graphene

due to the small momentum scale separating the massless Dirac cones in the trigonally warped spectrum. Increasing the strain further leaves a low energy spectrum made of two massless Dirac cones only. The modification to the band structure changes the nature of the Lifshitz transition as well as the energy for its occurrence. Thus, controllable strain could be used to induce the Lifshitz transition at the Fermi level, with observable consequences in the electronic density of states. The deformations leading to uniform gauge fields are uniaxial strain along a certain direction, a rigid shift of one layer with respect to the other as well as a pure shear.[47, 48]

A uniaxial in-plane strain along the direction $\hat{\theta} = (\cos \theta, \sin \theta)$ is described by the vector $\mathbf{u}^{(A)} = h^{(S)} = h^{(A)} = 0$ and $\mathbf{u}^{(S)}(\mathbf{r}) = \beta_{\parallel} r_{\parallel} \hat{\theta} + \beta_{\perp} r_{\perp} \hat{\theta}_{\perp}$, with $r_{\parallel} = \mathbf{r} \cdot \hat{\theta}$, $r_{\perp} = \mathbf{r} \cdot \hat{\theta}_{\perp}$ and $\hat{\theta}_{\perp} = \hat{z} \times \hat{\theta}$. Here β_{\parallel} and β_{\perp} represent the values of the strain along the two principal directions. This distortion results in a uniform deformation potential \mathcal{D} which is reabsorbed in a global shift of the zero energy, while $\mathcal{A} = 0$. The corresponding gauge fields are given by $F_{l=1,2}^{(\tau)} = 3a/4(\partial t_l/\partial a)(\beta_{\parallel} - \beta_{\perp}) \exp[-i\tau 2\theta]$, $F_{\gamma} = 0$, $F_3^{(\tau)} = 3a^2/4\tilde{c}(\partial\gamma_3/\partial\tilde{c})(\beta_{\parallel} - \beta_{\perp}) \exp[-i\tau 2\theta]$ and $F_4^{(\tau)} = 3a^2/4\tilde{c}(\partial\gamma_4/\partial\tilde{c})(\beta_{\parallel} - \beta_{\perp}) \exp[-i\tau 2\theta]$.

Similarly, a pure in-plane shear of amplitude ζ can be described by the deformation vector $\mathbf{u}^{(A)} = h^{(S)} = h^{(A)} = 0$ and $\mathbf{u}^{(S)}(\mathbf{r}) = \zeta r_{\parallel} \hat{\theta}_{\perp}$, resulting in the gauge fields $F_{l=1,2}^{(\tau)} = 3a/4(\partial t_l/\partial a)(-i\tau\zeta) \exp[-i\tau 2\theta]$, $F_{\gamma} = 0$, $F_3^{(\tau)} = 3a^2/4\tilde{c}(\partial\gamma_3/\partial\tilde{c})(-i\tau\zeta) \exp[-i\tau 2\theta]$ and $F_4^{(\tau)} = 3a^2/4\tilde{c}(\partial\gamma_4/\partial\tilde{c})(-i\tau\zeta) \exp[-i\tau 2\theta]$.

Finally, a shift of the second layer with respect to the first one by the amount ξa along $\hat{\theta}$ is described by the deformation vector $\mathbf{u}^{(S)} = \mathbf{u}^{(A)} = \xi a \hat{\theta}$, $h^{(S)} = h^{(A)} = 0$, resulting in the gauge fields $F_{l=1,2}^{(\tau)} = 0$, $F_{\gamma} = -2(\partial\gamma/\partial c)(\xi a)^2/c$, $F_3^{(\tau)} = 3a^2/\tilde{c}(\partial\gamma_3/\partial\tilde{c})(i\tau\xi) \exp[i\tau\theta]$ and $F_4^{(\tau)} = 3a^2/\tilde{c}(\partial\gamma_4/\partial\tilde{c})(-i\tau\xi) \exp[i\tau\theta]$.

Quite generally, these different deformations translate into complex gauge fields in the Hamiltonian, which then affect the electronic band structure. The evolution of the electronic band structure under progressive strain is illustrated in Fig. 3.3. Here we show the effect of a uniaxial strain of amplitude $\beta = \beta_{\parallel} - \beta_{\perp}$ along $\theta = 0$, equivalent to a uniform shear of amplitude $\zeta = \beta$ along $\theta = \pi/4$. In Fig. 3.3 we choose $\eta_{A1,B2} = \eta_{A1,A2} = \eta_{B1,B2} = 1$ for illustration purposes. The electronic band structure in the wavevector space (k_x, k_y) is shown in panels a1) to a4) at different values of β . While increasing β two cones with chirality π and $-\pi$ approach each other until they annihilate at zero energy for a critical strain β_{c1} . Increasing β further induces the two fused cones to produce a local minimum at finite energy, until a second critical strain β_{c2} is reached. For $\beta > \beta_{c2}$ the local minimum disappears, leaving two massless Dirac cones at low energy.

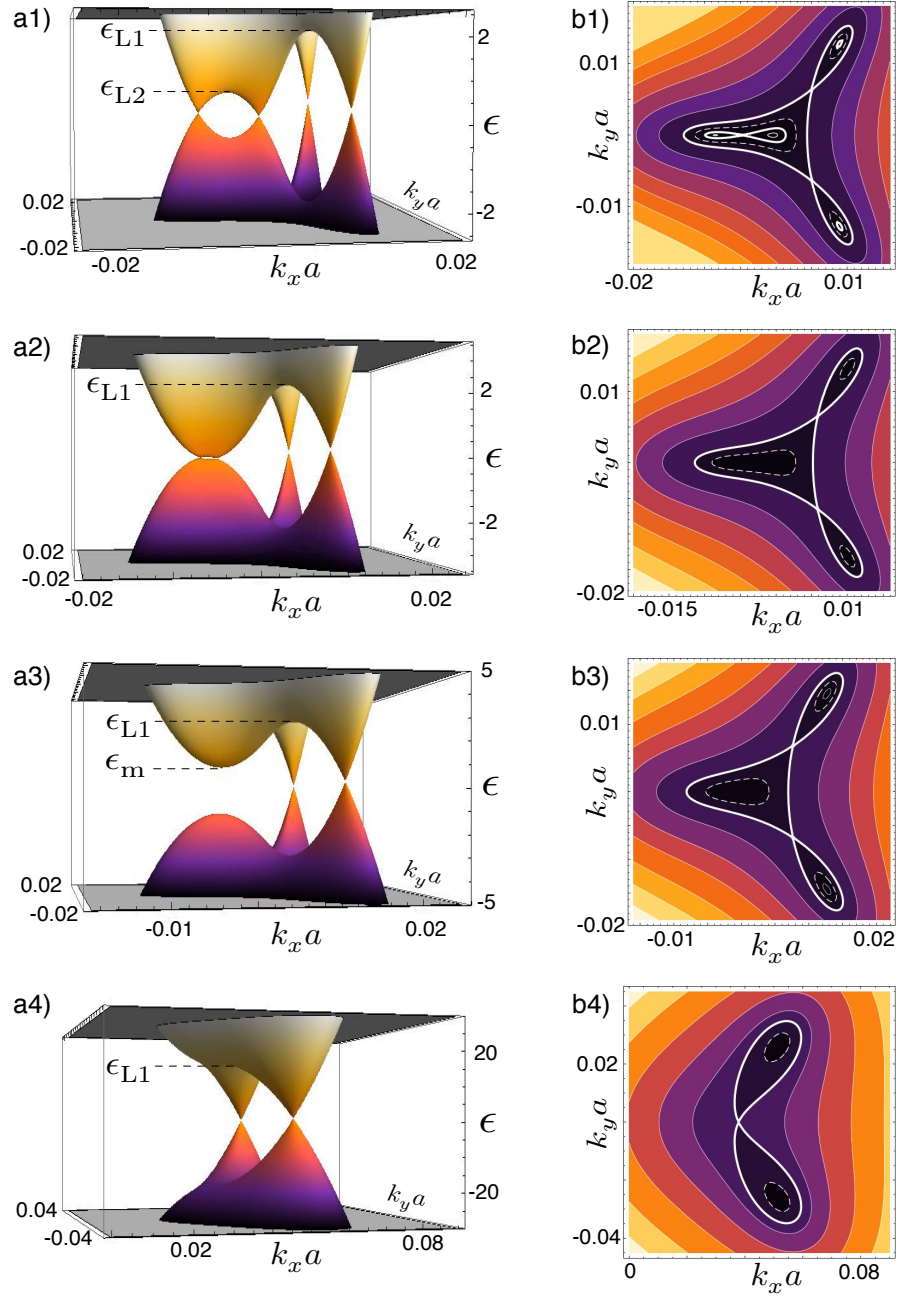


Figure 3.3: Electronic band structure in the wavevector space and equipotential lines for different values of strain β along $\theta = 0$, see text. Energy (ϵ) is expressed in meV and the plots are taken for $\eta_{A1,B2} = \eta_{A1,A2} = \eta_{B1,B2} = 1$. For these parameters we get $\beta_{c1} \approx 2.3 \cdot 10^{-3}$ and $\beta_{c2} \approx 2 \cdot 10^{-2}$. The notation $[N_e, N_h]$ indicates a Fermi surface made of N_e electron pockets and N_h hole pockets. Panel a1) Band structure for $\beta = 1.5 \cdot 10^{-3}$. Panel b1) Equipotential lines for a1), showing two Lifshitz transitions at ϵ_{L1} and ϵ_{L2} (thick lines). For $\epsilon > \epsilon_{L1}$ the Fermi surface is of type $[1,0]$ for this and all other panels. Dashed lines show the $[3,0]$ Fermi surface at an energy between the two Lifshitz transitions, while the thin lines exemplify a $[4,0]$ Fermi surface at $\epsilon < \epsilon_{L2}$. Panel a2) Band structure with critical strain β_{c1} . Panel b2) Equipotential lines for a2). One Lifshitz transition occurs at ϵ_{L1} , below which the Fermi surface is of type $[3,0]$. Panel a3) Band structure for $\beta = 4 \cdot 10^{-3}$. The corresponding equipotential lines are shown in panel b3). The dashed line shows the $[3,0]$ Fermi surface at $\epsilon_m < \epsilon < \epsilon_{L1}$, while thin lines show the $[2,0]$ Fermi surface at $0 < \epsilon < \epsilon_m$. Panel a4) Band structure for $\beta = 3 \cdot 10^{-2}$. The local minimum disappears. The corresponding equipotential lines are shown in panel b4). One Lifshitz transition occurs at ϵ_{L1} . The dashed line shows a $[2,0]$ Fermi surface for $0 < \epsilon < \epsilon_{L1}$.

In Fig 3.3, panel a1 illustrates the band structure in the regime $0 < \beta < \beta_{c1}$ and b1 the corresponding equipotential lines for electronic states at positive energy. Two Lifshitz transitions are visible at two different energies $\epsilon_{L1} > \epsilon^*$ and $\epsilon_{L2} < \epsilon^*$, where $\epsilon^* = 1.6\text{meV}$. Here for ease of discussion we reintroduce the notation $[N_e, N_h]$ which indicates a Fermi surface made of N_e electron pockets and N_h hole pockets. The Lifshitz transition at ϵ_{L1} separates a Fermi surface of type $[1,0]$ for $\epsilon > \epsilon_{L1}$ from a Fermi surface of type $[3,0]$ for $\epsilon_{L2} < \epsilon < \epsilon_{L1}$. Similarly, for $0 < \epsilon < \epsilon_{L2}$ the Fermi surface is of type $[4,0]$. Specular results are obtained for hole doping at negative energies. Panels a2) and b2) present the scenario for $\beta = \beta_{c1}$. Two Dirac cones fuse at zero energy and only one Lifshitz transition is left at ϵ_{L1} . Notice that the value of ϵ_{L1} grows while increasing the strain. The Lifshitz transition separates two Fermi surfaces of type $[3,0]$ and $[1,0]$ for $0 < \epsilon < \epsilon_{L1}$ and $\epsilon > \epsilon_{L1}$, respectively. Panels a3) and b3) illustrate the regime $\beta_{c1} < \beta < \beta_{c2}$ where a local minimum at finite energy ϵ_m survives. The Lifshitz transition separates two Fermi surfaces of type $[3,0]$ and $[1,0]$ for $\epsilon_m < \epsilon < \epsilon_{L1}$ and $\epsilon > \epsilon_{L1}$, respectively. A new regime with Fermi surface of type $[2,0]$ appears for $0 < \epsilon < \epsilon_m$. Finally, for $\beta > \beta_{c2}$ a single Lifshitz transition occurs separating Fermi surfaces of types $[2,0]$ from $[1,0]$ for $\epsilon < \epsilon_{L1}$ and $\epsilon > \epsilon_{L1}$, respectively. This is illustrated in panels a4) and b4). It has to be noticed that in this regime of strain, the value of ϵ_{L1} is significantly larger than ϵ^* . The ability to tune the energy of the Lifshitz transition allows us to explore it at different levels of doping and also to partially overcome the problems in resolution due to disorder.

The qualitative picture above is reproduced, essentially unaffected, once the strain distribution is applied at different angles θ . The precise values of the critical strains β_{c1} and β_{c2} depend on θ and on the values of the parameters $\partial t_{sl,s'l'}/\partial \ell_{sl,s'l'} \simeq -\eta_{sl,s'l'} t_{sl,s'l'}/\ell_{sl,s'l'}$. Since all relevant derivatives are not known it is not possible to give a quantitative estimate of the critical strains. However, as shown in Fig. 3.3, for $\eta_{A1,B2} = \eta_{A1,A2} = \eta_{B1,B2} = 1$ the typical order of magnitude for them is around $0.2\% - 2\%$. This is easily achieved in realistic suspended graphene samples. These parameters suggest that the low energy spectrum in conventional bilayer samples is probably characterised by two massless cones per valley, instead of four. As a consequence, in the presence of an external magnetic field, the degeneracy of the Landau Level at zero energy is expected to be eight, due to two massless cones and two spins in each valley.[48] This picture is compatible with the recently observed integer quantum Hall effect at filling factors $\nu = \pm 4$ in bilayer graphene at low magnetic fields.[49, 50] Similar consequences, although in a different context, have been analysed

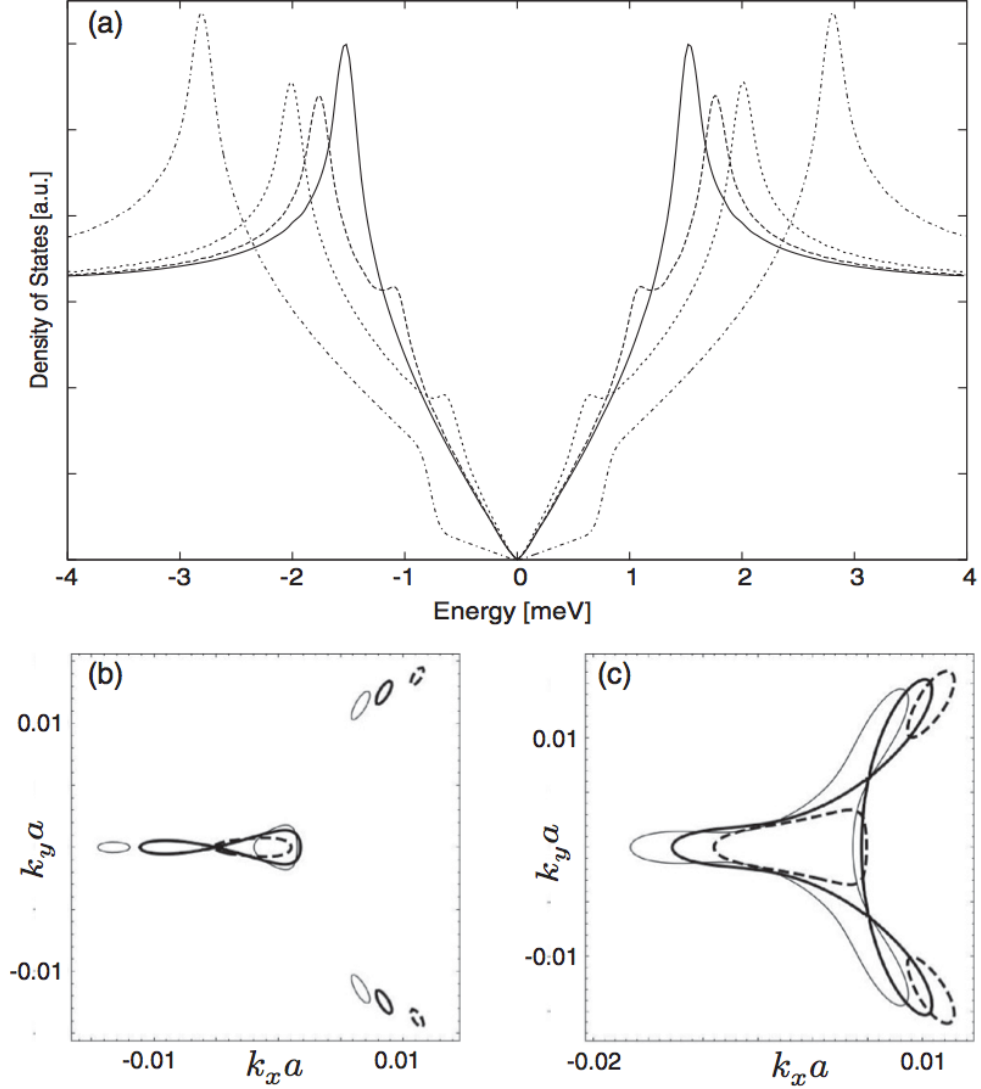


Figure 3.4: The electronic DOS and Fermi surface at a fixed electron density for different values of strain β along $\theta = 0$. As in Fig. 3.3 we choose $\eta_{A1,B2} = \eta_{A1,A2} = \eta_{B1,B2} = 1$. a) Electronic DOS as a function of energy for $\beta = 0$ (thick line), $\beta = 10^{-3}$ (dashed line), $\beta = 2 \times 10^{-3}$ (dotted line), and $\beta = 5 \times 10^{-3}$ (dot-dashed line). The peaks in the DOS at the various Lifshitz transitions are clearly visible, as well as the linear dependence on energy in the low-energy regime due to the massless Dirac cones. The dot-dashed line shows a steplike feature at ϵ_m associated with the local parabolic minimum in the dispersion [see Fig. 3(a3)]. b) Electron doping corresponding to $\epsilon_F = 0.8 \text{ meV} < \epsilon^*$. The thin line is for $\beta = 0$. The thick line shows the Fermi surface at the Lifshitz transition ($\epsilon_F = \epsilon_{L2}$) for $\beta \approx 1.2 \cdot 10^{-3}$, while the dashed line shows $\beta \approx 3 \cdot 10^{-3}$. c) Electron doping corresponding to $\epsilon_F = 2.2 \text{ meV} > \epsilon^*$. The thin, thick and dashed lines correspond to $\beta = 0$, $\beta \approx 1.6 \cdot 10^{-3}$ and $\beta \approx 3 \cdot 10^{-3}$, respectively. The Lifshitz transition here occurs at $\epsilon_F = \epsilon_{L1}$.

in terms of an interaction-induced spontaneous symmetry breaking leading to a nematic phase characterised by two massless Dirac cones at low-energy. [51, 52]. The latter scenario has been discussed in a measurement on suspended bilayer graphene with extremely high mobility.[53]

As highlighted in Fig. 3.3, panels b1) to b4), the structure of the Fermi surface at a given density is thus affected by strain, due to the fusion of the Dirac cones. As a consequence, the nature of the Lifshitz transitions is sensitive to mechanical deformations. A controllable increase of the amount of strain in the bilayer graphene membrane could drive the Lifshitz transition at the Fermi level with observable consequences on the electronic DOS, as illustrated in Fig. 3.4. This effect could be directly detected in compressibility measurements as a function of density while keeping the strain constant or at a fixed density while tuning the strain. The modulation of the DOS at the Fermi level could also produce signatures in the transport properties in the linear regime as long as the relevant diffusion coefficient is smooth across the Lifshitz transition.

3.6 Conclusion

In summary we have introduced an overview of the electromechanical properties of graphene, included all the important concepts that we will continue to use throughout this thesis. We started with a brief introduction to elasticity theory for two dimensional membranes and used this formalism to develop the theory of fictitious gauge fields in both monolayer and bilayer graphene. It has been shown that fictitious gauge fields can have dramatic effect on the electronic spectrum, particularly in the case of the electronic spectrum of trigonally warped bilayer graphene. The role of fictitious gauge fields created by mechanical deformations will be a dominant theme of this work for the rest of this thesis.

Bibliography

- [1] K. S. Kim, Y. Zhao, H. Jang, S. Y. Lee, J. M. Kim, K. S. Kim, J.-H. Ahn, P. Kim, J.-Y. Choi, and B. H. Hong, “Large-scale pattern growth of graphene films for stretchable transparent electrodes,” *Nature*, vol. 457, pp. 706–710, 02 2009.
- [2] J. K. Wassei and R. B. Kaner, “Graphene, a promising transparent conductor,” *Materials Today*, vol. 13, pp. 52–59, 3 2010.
- [3] S. Bae, H. Kim, Y. Lee, X. Xu, J.-S. Park, Y. Zheng, J. Balakrishnan, T. Lei, H. Ri Kim, Y. I. Song, Y.-J. Kim, K. S. Kim, B. Ozyilmaz, J.-H. Ahn, B. H. Hong, and S. Iijima, “Roll-to-roll production of 30-inch graphene films for transparent electrodes,” *Nat Nano*, vol. 5, pp. 574–578, 08 2010.
- [4] A. Fasolino, J. H. Los, and M. I. Katsnelson, “Intrinsic ripples in graphene,” *Nat Mater*, vol. 6, pp. 858–861, 11 2007.
- [5] V. Geringer, M. Liebmann, T. Echtermeyer, S. Runte, M. Schmidt, R. Rückamp, M. C. Lemme, and M. Morgenstern, “Intrinsic and extrinsic corrugation of monolayer graphene deposited on sio₂,” *Physical Review Letters*, vol. 102, pp. 076102–, 02 2009.
- [6] J. S. Bunch, A. M. van der Zande, S. S. Verbridge, I. W. Frank, D. M. Tanenbaum, J. M. Parpia, H. G. Craighead, and P. L. McEuen, “Electromechanical resonators from graphene sheets,” *Science*, vol. 315, no. 5811, pp. 490–493, 2007.
- [7] J. C. Meyer, A. K. Geim, M. I. Katsnelson, K. S. Novoselov, T. J. Booth, and S. Roth, “The structure of suspended graphene sheets,” *Nature*, vol. 446, pp. 60–63, 03 2007.

- [8] K. I. Bolotin, K. J. Sikes, Z. Jiang, M. Klima, G. Fudenberg, J. Hone, P. Kim, and H. L. Stormer, "Ultrahigh electron mobility in suspended graphene," *Solid State Communications*, vol. 146, pp. 351–355, 6 2008.
- [9] M. A. H. Vozmediano, M. I. Katsnelson, and F. Guinea, "Gauge fields in graphene," *Physics Reports*, vol. 496, pp. 109–148, 11 2010.
- [10] L. M. Woods and G. D. Mahan, "Electron-phonon effects in graphene and armchair (10,10) single-wall carbon nanotubes," *Physical Review B*, vol. 61, pp. 10651–10663, 04 2000.
- [11] H. Suzuura and T. Ando, "Phonons and electron-phonon scattering in carbon nanotubes," *Physical Review B*, vol. 65, pp. 235412–, 05 2002.
- [12] E. Mariani, L. I. Glazman, A. Kamenev, and F. von Oppen, "Zero-bias anomaly in the tunneling density of states of graphene," *Physical Review B*, vol. 76, pp. 165402–, 10 2007.
- [13] E. Mariani and F. von Oppen, "Flexural phonons in free-standing graphene," *Physical Review Letters*, vol. 100, pp. 076801–, 02 2008.
- [14] M. M. Fogler, F. Guinea, and M. I. Katsnelson, "Pseudomagnetic fields and ballistic transport in a suspended graphene sheet," *Physical Review Letters*, vol. 101, pp. 226804–, 11 2008.
- [15] V. M. Pereira and A. H. Castro Neto, "Strain engineering of graphene's electronic structure," *Physical Review Letters*, vol. 103, pp. 046801–, 07 2009.
- [16] M. Katsnelson and A. Geim, "Electron scattering on microscopic corrugations in graphene," *Philosophical Transactions of the Royal Society A: Mathematical, Physical and Engineering Sciences*, vol. 366, no. 1863, pp. 195–204, 2008.
- [17] F. Guinea, M. I. Katsnelson, and M. A. H. Vozmediano, "Midgap states and charge inhomogeneities in corrugated graphene," *Physical Review B*, vol. 77, pp. 075422–, 02 2008.
- [18] F. de Juan, A. Cortijo, M. A. H. Vozmediano, and A. Cano, "Aharonov-bohm interferences from local deformations in graphene," *Nat Phys*, vol. 7, pp. 810–815, 10 2011.
- [19] F. Guinea, M. I. Katsnelson, and A. K. Geim, "Energy gaps and a zero-field quantum hall effect in graphene by strain engineering," *Nat Phys*, vol. 6, pp. 30–33, 01 2010.

- [20] N. Levy, S. A. Burke, K. L. Meaker, M. Panlasigui, A. Zettl, F. Guinea, A. H. C. Neto, and M. F. Crommie, “Strain-induced pseudo-magnetic fields greater than 300 tesla in graphene nanobubbles,” *Science*, vol. 329, no. 5991, pp. 544–547, 2010.
- [21] S. V. Morozov, K. S. Novoselov, M. I. Katsnelson, F. Schedin, L. A. Ponomarenko, D. Jiang, and A. K. Geim, “Strong suppression of weak localization in graphene,” *Physical Review Letters*, vol. 97, pp. 016801–, 07 2006.
- [22] A. F. Morpurgo and F. Guinea, “Intervalley scattering, long-range disorder, and effective time-reversal symmetry breaking in graphene,” *Physical Review Letters*, vol. 97, pp. 196804–, 11 2006.
- [23] E. McCann, K. Kechedzhi, V. I. Fal’ko, H. Suzuura, T. Ando, and B. L. Altshuler, “Weak-localization magnetoresistance and valley symmetry in graphene,” *Physical Review Letters*, vol. 97, pp. 146805–, 10 2006.
- [24] F. V. Tikhonenko, D. W. Horsell, R. V. Gorbachev, and A. K. Savchenko, “Weak localization in graphene flakes,” *Physical Review Letters*, vol. 100, pp. 056802–, 02 2008.
- [25] L. D. Landau and E. M. Lifshitz, *Theory of Elasticity*. Pergamon, New York, 1986.
- [26] K. N. Kudin, G. E. Scuseria, and B. I. Yakobson, “C₂f, bn, and c nanoshell elasticity from ab initio computations,” *Physical Review B*, vol. 64, pp. 235406–, 11 2001.
- [27] C. Lee, X. Wei, J. W. Kysar, and J. Hone, “Measurement of the elastic properties and intrinsic strength of monolayer graphene,” *Science*, vol. 321, no. 5887, pp. 385–388, 2008.
- [28] K. V. Zakharchenko, M. I. Katsnelson, and A. Fasolino, “Finite temperature lattice properties of graphene beyond the quasiharmonic approximation,” *Physical Review Letters*, vol. 102, pp. 046808–, 01 2009.
- [29] R. E. Peierls, “Quelques proprietes typiques des corps solides,” *Ann. I. H. Poincare*, vol. 5, pp. 177–222, 1935.
- [30] L. D. Landau, “Zur theorie der phasenumwandlungen ii,” *Phys. Z. Sowjetunion*, vol. 11, pp. 26–35, 1937.

- [31] N. D. Mermin, “Crystalline order in two dimensions,” *Physical Review*, vol. 176, pp. 250–254, 12 1968.
- [32] D. R. Nelson and L. Peliti, “Fluctuations in membranes with crystalline and hexatic order,” *J. Phys. (Paris)*, vol. 48, pp. 1085–1092, 1987.
- [33] M. Paczuski, M. Kardar, and D. R. Nelson, “Landau theory of the crumpling transition,” *Physical Review Letters*, vol. 60, pp. 2638–2640, 06 1988.
- [34] D. R. Nelson, T. Piran, and S. Weinberg, *Statistical Mechanics of Membranes and Surfaces*. World Scientific, Singapore, 1989.
- [35] K.-i. Sasaki, Y. Kawazoe, and R. Saito, “Local energy gap in deformed carbon nanotubes,” *Progress of Theoretical Physics*, vol. 113, no. 3, pp. 463–480, 2005.
- [36] E. H. Hwang and S. Das Sarma, “Dielectric function, screening, and plasmons in two-dimensional graphene,” *Physical Review B*, vol. 75, pp. 205418–, 05 2007.
- [37] E. Mariani and F. von Oppen, “Temperature-dependent resistivity of suspended graphene,” *Physical Review B*, vol. 82, pp. 195403–, 11 2010.
- [38] F. von Oppen, F. Guinea, and E. Mariani, “Synthetic electric fields and phonon damping in carbon nanotubes and graphene,” *Physical Review B*, vol. 80, pp. 075420–, 08 2009.
- [39] V. M. Pereira, A. H. Castro Neto, and N. M. R. Peres, “Tight-binding approach to uniaxial strain in graphene,” *Physical Review B*, vol. 80, pp. 045401–, 07 2009.
- [40] F. M. D. Pellegrino, G. G. N. Angilella, and R. Pucci, “Strain effect on the optical conductivity of graphene,” *Physical Review B*, vol. 81, pp. 035411–, 01 2010.
- [41] S.-M. Choi, S.-H. Jhi, and Y.-W. Son, “Effects of strain on electronic properties of graphene,” *Physical Review B*, vol. 81, pp. 081407–, 02 2010.
- [42] F. Guinea, A. K. Geim, M. I. Katsnelson, and K. S. Novoselov, “Generating quantizing pseudomagnetic fields by bending graphene ribbons,” *Physical Review B*, vol. 81, pp. 035408–, 01 2010.
- [43] D. A. Abanin and D. A. Pesin, “Interaction-induced topological insulator states in strained graphene,” *Physical Review Letters*, vol. 109, pp. 066802–, 08 2012.

- [44] E. Cappelluti and G. Profeta, “Hopping-resolved electron-phonon coupling in bilayer graphene,” *Physical Review B*, vol. 85, pp. 205436–, 05 2012.
- [45] E. McCann and V. I. Fal’ko, “Landau-level degeneracy and quantum hall effect in a graphite bilayer,” *Physical Review Letters*, vol. 96, pp. 086805–, 03 2006.
- [46] J. R. Schrieffer and P. A. Wolff, “Relation between the anderson and kondo hamiltonians,” *Physical Review*, vol. 149, pp. 491–492, 09 1966.
- [47] Y.-W. Son, S.-M. Choi, Y. P. Hong, S. Woo, and S.-H. Jhi, “Electronic topological transition in sliding bilayer graphene,” *Physical Review B*, vol. 84, pp. 155410–, 10 2011.
- [48] M. Mucha-Kruczyński, I. L. Aleiner, and V. I. Fal’ko, “Strained bilayer graphene: Band structure topology and landau level spectrum,” *Physical Review B*, vol. 84, pp. 041404–, 07 2011.
- [49] R. T. Weitz, M. T. Allen, B. E. Feldman, J. Martin, and A. Yacoby, “Broken-symmetry states in doubly gated suspended bilayer graphene,” *Science*, vol. 330, no. 6005, pp. 812–816, 2010.
- [50] J. Martin, B. E. Feldman, R. T. Weitz, M. T. Allen, and A. Yacoby, “Local compressibility measurements of correlated states in suspended bilayer graphene,” *Physical Review Letters*, vol. 105, pp. 256806–, 12 2010.
- [51] O. Vafek and K. Yang, “Many-body instability of coulomb interacting bilayer graphene: Renormalization group approach,” *Physical Review B*, vol. 81, pp. 041401–, 01 2010.
- [52] Y. Lemonik, I. L. Aleiner, C. Toke, and V. I. Fal’ko, “Spontaneous symmetry breaking and lifshitz transition in bilayer graphene,” *Physical Review B*, vol. 82, pp. 201408–, 11 2010.
- [53] A. S. Mayorov, D. C. Elias, M. Mucha-Kruczynski, R. V. Gorbachev, T. Tudorovskiy, A. Zhukov, S. V. Morozov, M. I. Katsnelson, V. I. Fal’ko, A. K. Geim, and K. S. Novoselov, “Interaction-driven spectrum reconstruction in bilayer graphene,” *Science*, vol. 333, no. 6044, pp. 860–863, 2011.

4

Conductance and Shot Noise In Strained Bilayer Graphene

4.1 Introduction

While the first tight-binding analysis of the single particle electronic dispersion suggested the presence of chiral massive Dirac quasiparticles,[1] successive theoretical[2, 3, 4, 5, 6, 7, 8, 9, 10] and experimental[11, 12, 13] studies have shown how trigonal warping, strain and many-body interactions induce dramatic qualitative changes in the low energy spectrum and in the nature of current carriers. In the previous chapter we saw a discussion focusing on the effect of strain in the low energy band structure of bilayer graphene. Motivated by the recent development of ballistic bilayer graphene devices and by their unique low energy band structure, in this chapter we investigate the conductance and Fano factor of bilayer graphene, including trigonal warping, in the absence and presence of external strain.

The fundamental nature of current carriers in graphene devices can be effectively probed by

means of electronic transport measurements. In particular electrical conductors exhibit a shot noise in the current due to the quantisation of charge.[14] A useful tool to characterise this phenomenon is the Fano factor F which is the ratio between the powers associated with shot noise and mean current. The Fano factor of ballistic graphene at the Dirac point has been theoretically predicted to be $F = 1/3$ for the massless Dirac spectrum of monolayers[15] as well as in bilayers, with an approximate parabolic dispersion.[16] The value of $F = 1/3$ is the same as in classical disordered conductors. This coincidence is remarkable as the analysis of graphene systems leading to this result considered only perfectly ballistic devices. As a consequence, the ballistic electron transport in graphene devices in the regimes where the Fano factor is approximately $1/3$ is called *pseudo-diffusive*. This result is understood as due to the dominant contribution to the transport at the Dirac point from evanescent modes. Experiments have observed $F = 1/3$ at the Dirac point in both monolayer[17, 18] and bilayer[19] graphene, but the behaviour as a function of carrier density seems to depend strongly on the amount of disorder present in the sample.[20, 21] Recent advances in fabricating high mobility bilayer graphene samples in suspended devices or on boron nitride substrates allow for the investigation of the physics of ballistic transport at small energy scales.[11, 12, 13] In this regime it is thus crucial to address the detailed structure of the electronic spectrum and its consequences on transport and shot noise measurements. This is the focus of the present chapter.

The low energy physics of bilayer graphene is dominated by the effect of trigonal warping, leading to a reconstruction of the spectrum close to zero energy. The rich structure formed by trigonal warping at low energies in bilayer graphene can be completely reconstructed by the application of strain.[5, 6, 8] Uniaxial strain causes the position of the Dirac points to drift in momentum space. As the applied strain increases, the two Dirac points lying closest to the axis of applied strain will meet and coalesce, leaving a reconstructed electronic spectrum of two Dirac cones and lower rotational symmetry. Due to the small momentum scale which separates the four massless Dirac cones of the trigonally warped electronic spectrum, relatively small strains of the order $u \approx 10^{-3}$ are sufficient to cause dramatic modifications to the electronic spectrum. This suggests that the band structure of conventional suspended bilayer graphene devices can be heavily influenced by the amount of strain that is naturally present in the sample. An analogous reconstruction of the low energy electronic spectrum is also predicted to occur due to electron-electron interactions which can lead to a spontaneous transition to a nematic phase.[9, 10] However, as the

energy scale at which the Lifshitz transition occurs is rather small ($\epsilon_L = 1.6\text{meV}$), the effect of trigonal warping can only be seen in very clean samples with mobilities of at least $\mu \approx 10^4 \text{ cm}^2\text{V}^{-1}\text{s}^{-1}$, as reported recently.[12]

The results for the conductance of samples in the absence of strain show that the Lifshitz transition induced by trigonal warping causes distinct signatures compared to the model with a simple parabolic electronic spectrum. In addition, the anomalies related to the Lifshitz transition persist under large applied strain, in agreement with those predicted in a work by Gradinar et al.[22] The effect of trigonal warping and of strain on the shot noise has never been addressed so far. Here we show that bilayer graphene with trigonal warping still possesses a Fano factor of $F = 1/3$ at the Dirac point, but the energy interval over which the pseudo-diffusive transport is observed is orders of magnitude larger than in the absence of trigonal warping and the application of strain in the sample increases this energy range further.

The structure of the chapter is as follows: In section 4.2 we present the electronic properties of bilayer graphene in presence of trigonal warping. Section 4.3 introduces the theory of uniaxial strain in bilayer graphene. In section 4.4 we discuss the scattering matrix approach employed to address the ballistic transport of the system. In section 4.5 we present our results on the transmission probability, on the conductance and on the Fano factor, and discuss the effect of strain on the ballistic transport and conclude.

4.2 Model of Bilayer Graphene

For clarity here we reintroduce the Hamiltonian and band structure for trigonal warped bilayer graphene. The electronic spectrum is presented in Fig 4.1 showing the influence of the γ_3 hopping term which creates trigonal warping, most clearly seen in low energy spectrum in Fig 4.1.b. The inclusion of the γ_3 term reduces the rotational symmetry of the electronic spectrum, therefore the crystallographic orientation of the sample will have an effect on transport. Since during sample fabrication there is no way to control the crystallographic orientation, we shall study different orientations of the electronic spectrum in a rectangular device, parameterised by the angle θ between the trigonally warped spectrum and the x -axis of the sample (along which uniaxial strain will act).

The spectrum describing the two low energy bands of bilayer graphene with trigonal warping has been obtained in the energy range $|\epsilon| \ll \gamma_1$ [2, 3] and has been presented in section 2.3,

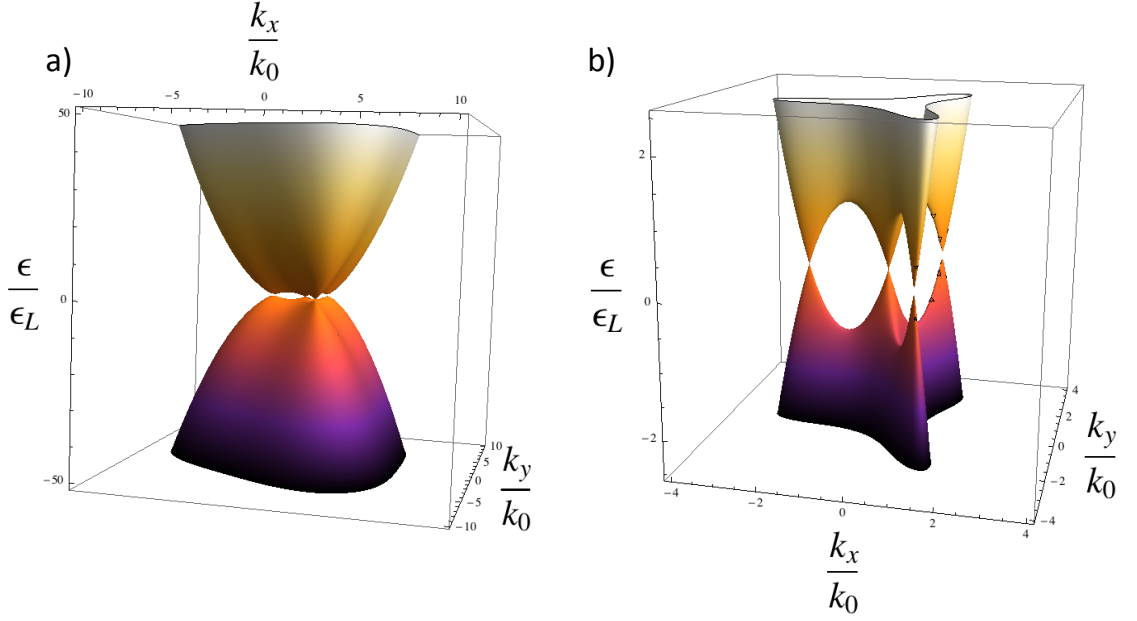


Figure 4.1: Electronic spectrum of trigonally warped bilayer graphene. Panel a) shows the modification to the parabolic spectrum at low energies due to trigonal warping. Panel b) highlights the low energy sector revealing the structure of four massless Dirac cones. The energy ϵ is given in units of $\epsilon_L = mv_3^2/2$ and the wavevectors k_x and k_y in units of $k_0 = mv_3/\hbar$.

where the effective Hamiltonian in the 2×2 A1-B2 space takes the form

$$H^{(+)} = \frac{\hbar^2}{2m} \begin{pmatrix} 0 & (k^\dagger)^2 \\ k^2 & 0 \end{pmatrix} + v_3 \hbar \begin{pmatrix} 0 & k \\ k^\dagger & 0 \end{pmatrix} + V(x) \cdot \mathbf{1}. \quad (4.1)$$

Here we consider the $\tau = +1$ valley and use the complex representation of the 2D wavevector $k = (k_x + ik_y)e^{i\theta} = |k|e^{i(\phi+\theta)}$ (with $\tan \phi = k_y/k_x$), the effective electron mass $m = \gamma_1/2v^2 = 0.054 m_e$ (with m_e the free electron mass), the inter-layer group velocity $v_3 = 3a\gamma_3/2\hbar = 10^5$ m/s and $V(x)$ represents an external scalar potential, with $\mathbf{1}$ the 2×2 unit matrix. In the regions where the scalar potential is uniform ($V(x) = V$) the electronic spectrum obtained by diagonalising the Hamiltonian above fulfils the condition

$$(\epsilon - V)^2 = \frac{\hbar^4}{4m^2}|k|^4 + v_3^2 \hbar^2 |k|^2 + \frac{v_3 \hbar^3}{m} |k|^3 \cos(3\phi + 3\theta). \quad (4.2)$$

The locations of the four electron pockets of vanishing size at $\epsilon = 0$ and $V(x) = 0$ are thus $|k| = 0$ for the central cone and $|k| = 2mv_3/\hbar$ and $\phi = -\theta + (2n + 1)\pi/3$ for the outer cones, where $n = 0, 1, 2$. The four massless cones merge with a Lifshitz transition at the critical energy $\epsilon_L = mv_3^2/2 \approx 1.6$ meV with an associated van Hove singularity in the single particle density of

states.[8]

4.3 Uniaxial Strain in Bilayer Graphene

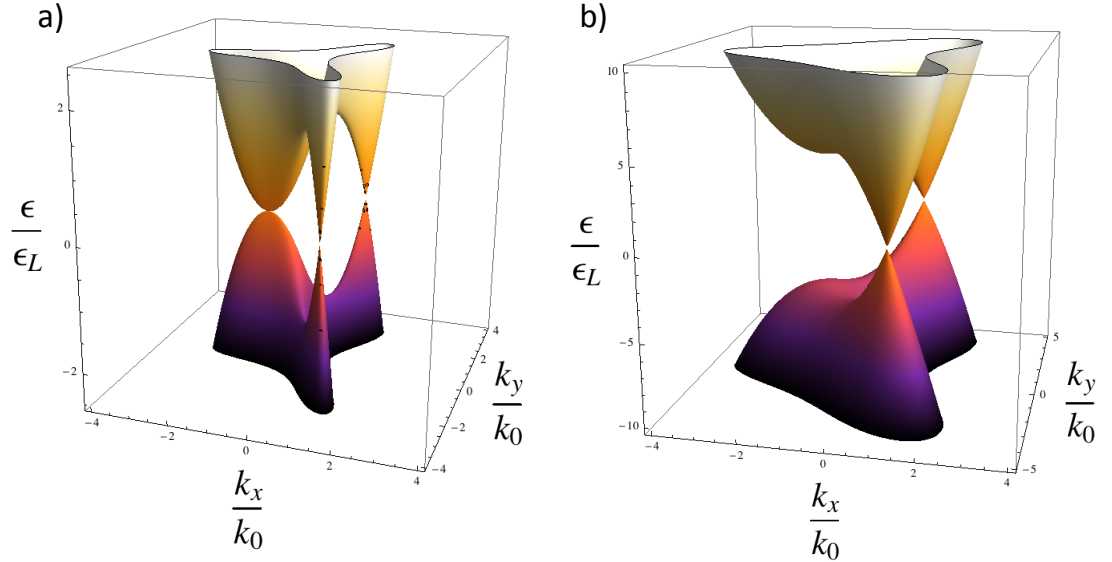


Figure 4.2: Electronic spectrum of trigonally warped bilayer graphene under uniaxial strain along the x -axis (with $\theta = 0$). Panel a) shows the modification to the electronic spectrum at the critical strain ($\tilde{\alpha} = 1$) at which two cones merge. Panel b) shows the modification to the electronic dispersion at $\tilde{\alpha} = 5$ with a reconstructed spectrum at low-energy characterised by two massless Dirac cones. The energy ϵ is given in units of $\epsilon_L = mv_3^2/2$ and the wavevectors k_x and k_y in units of $k_0 = mv_3/\hbar$.

As we have seen in section 3.4 mechanical deformations of the graphene lattice couple to the electronic properties in two ways; by the deformation potential and via a fictitious gauge field.[23, 24, 25, 26] Previously we derived the full form of the fictitious gauge fields due to any arbitrary elastic deformation in bilayer graphene.[8] In this chapter using what was presented in section 3.4, we will consider the specific case of uniaxial strain on a rectangular sample of length L_x and width L_y . A sketch of the sample setup is shown in Fig. 4.3. The uniaxial strain creates a uniform gauge field across the sample, proportional to the extension of the sample δL_x . In this study we will only consider uniaxial strain in the x -direction as it is the strain configuration that is most easily realisable in experiments, in particular in suspended graphene devices due to the tension induced at the contacts between the sample and the source and drain leads. The resulting

modification in the energy of the in-plane (t) and skew interlayer hopping terms (γ_3) are

$$\alpha_0 = \frac{3a}{4} \frac{\partial t}{\partial a} \frac{\delta L_x}{L_x} \quad (4.3)$$

$$\alpha_3 = \frac{3a^2}{4\tilde{c}} \frac{\partial \gamma_3}{\partial \tilde{c}} \frac{\delta L_x}{L_x} \quad (4.4)$$

where $\tilde{c} = (a^2 + c^2)^{1/2}$ is the skew distance between atoms belonging to different sublattices in different layers. The numerical values of the partial derivatives have been calculated as $\partial t/\partial a = -4.41 \text{ eV/\AA} \simeq -2.53 t/a$ and $\partial \gamma_3/\partial \tilde{c} = -0.54 \text{ eV/\AA} \simeq -6.7 \gamma_3/\tilde{c}$. [27]

In addition to the corrections to the hopping terms, local contraction and dilations in area also induce a scalar deformation potential, shifting the energy at which the Dirac point is located. For uniaxial strain in the x -direction the deformation potential takes the form

$$D^{(s)} = g \frac{\delta L_x}{L_x} \quad (4.5)$$

where g is a coupling constant, which takes the unscreened value $g \simeq 20 \text{ eV}$. [23]

We can now construct the effective low energy Hamiltonian for uniaxially strained, trigonally warped bilayer graphene in the $\tau = +1$ valley

$$H^{(+)} = \frac{\hbar^2}{2m} \begin{pmatrix} 0 & (k^\dagger)^2 \\ k^2 & 0 \end{pmatrix} + \hbar v_3 \begin{pmatrix} 0 & k \\ k^\dagger & 0 \end{pmatrix} + \begin{pmatrix} D^{(s)} & \alpha \\ \alpha^\dagger & D^{(s)} \end{pmatrix} + V \cdot \mathbf{1}.$$

Here we performed the convenient gauge transformation $\psi \rightarrow \exp(i\alpha_0 x/\hbar v) \psi$ which downloads the corrections α_j on the trigonal warping term alone, and we introduced $\alpha = \alpha_3 - \alpha_0$. Diagonalising the effective Hamiltonian above leads to the strained electronic dispersion which fulfils the condition

$$(\tilde{\epsilon} - \tilde{D}^{(s)} - \tilde{V})^2 = |\tilde{k}|^4 + 4|\tilde{k}|^3 \cos[3(\phi + \theta)] + 2|\tilde{k}|^2(2 + \tilde{\alpha} \cos[2(\phi + \theta)]) + 4|\tilde{k}|\tilde{\alpha} \cos(\phi + \theta) + \tilde{\alpha}^2. \quad (4.6)$$

In this expression we have introduced dimensionless units, rescaling energies (ϵ , α , $D^{(s)}$ and V) by the unstrained Lifshitz transition energy ϵ_L (e.g. $\tilde{\epsilon} = \epsilon/\epsilon_L$ and similarly for $\tilde{\alpha}$, $\tilde{D}^{(s)}$ and $\tilde{V}(x)$) and wave vectors by the characteristic wave vector scale associated with the appearance of the outer massless Dirac cones due to trigonal warping ($\tilde{k} = k/k_0$, with $k_0 = mv_3/\hbar$). The Hamiltonian and dispersion above will now be used to calculate the ballistic conductance and the Fano factor across

strained bilayer devices within the scattering matrix approach.

4.4 Scattering Matrix

To study the transport properties of bilayer graphene in the ballistic regime we need to construct the scattering matrix for the problem. We consider a pristine, neutral sample of width L_y with highly electron doped bilayer graphene leads. This setup is modelled by the step-like potential

$$V(x) = \begin{cases} 0 & \text{if } 0 < x < L_x \\ V_{\text{lead}} \ll -\epsilon_L & \text{if } x < 0, x > L_x \end{cases} \quad (4.7)$$

as sketched in Fig. 4.3a. Taking $V_{\text{lead}} \ll -\epsilon_L$ means that the Fermi surface will always be singly connected in the leads. We assume that the potential step between the leads and the sample is smooth on the scale of the lattice spacing but sharper than the Fermi wavelength, which allows to model it as a step-like function while neglecting inter-valley scattering. Our setup allows for the consideration of both n-n-n and n-p-n junctions by modulating the carrier density in the sample which we model as the central region, which can be controlled in experiments by an external back-gate. As far as deformations are concerned, we model the device as having no strain in the leads, due to the clamping at the contacts, while the uniaxial strain is only present in the central region of the sample. The related deformation potential will thus shift the neutrality point in the sample by the amount $D^{(s)}$, as will be evident in the analysis of ballistic transport.

In order to treat the system within the low-energy two-bands model, we consider carrier densities such that the higher split band at energy γ_1 is never occupied in the leads and thus limit our attention to the energy interval $|\epsilon| < \gamma_1 - |V_{\text{lead}}|$. While treating the scattering problem of Dirac fermions across the potential barrier $V(x)$, translational invariance in the y -direction leads to conservation of the transverse wavevector k_y , yielding an electronic wavefunction of the form $\Psi(x, y) = \psi(x)e^{ik_y y}$. Our aim is to calculate the transmission probability $T(k_y)$ which can be deduced from the transmission coefficient $t(k_y)$ (or the reflection coefficient $r(k_y)$) via the relation $T(k_y) = t^\dagger(k_y)t(k_y) = 1 - r^\dagger(k_y)r(k_y)$.

In order to calculate $t(k_y)$ we consider the scattering through the device by constructing the electronic wavefunction $\psi(x)$ in the three regions (source-sample-drain) as a linear combination of plane wave states. The corresponding longitudinal wavevectors are obtained by solving Eq. 4.6,

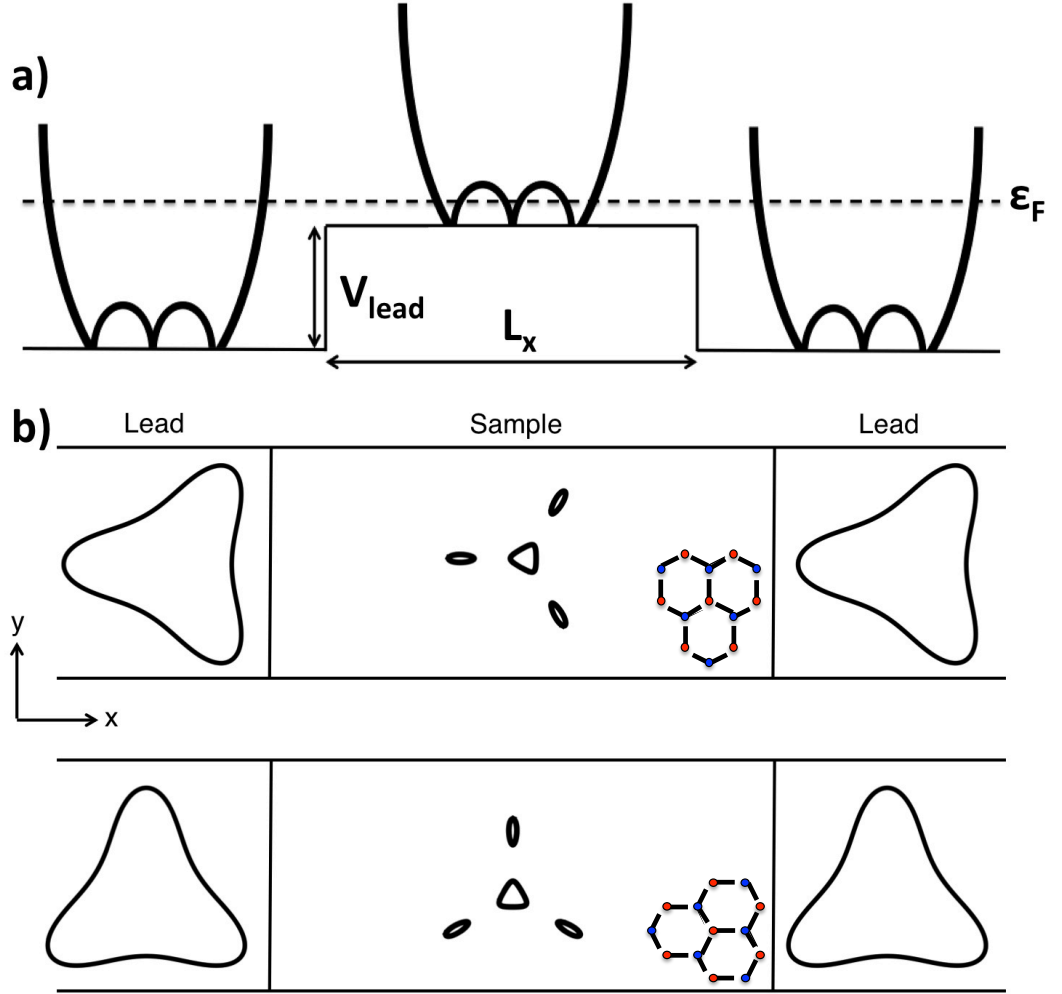


Figure 4.3: Schematic of the bilayer graphene device setup. Panel a) shows the electrostatic potential across the leads and the sample. Panel b) shows a top down view of the device with the two crystallographic orientations considered in this study (top $\theta = 0$, bottom $\theta = \pi/2$) with a sketch of the crystal lattice in each orientation shown.

yielding four solutions for each given k_y , which we label $k_x^{(n)}$ in the leads and $q_x^{(n)}$ in the sample, where $n = 1, 2, 3, 4$. Due to the complexity of the trigonally warped spectrum the values of $k_x^{(n)}$ and $q_x^{(n)}$ have to be found numerically. The four solutions can correspond to either propagating or evanescent modes. When solving Eq. 4.6, wherever the Fermi surface is connected (e.g. in either lead or in the sample at energies $|\epsilon| > |\epsilon_L|$ in the unstrained case $\tilde{\alpha} = 0$), we find two real propagating modes and two evanescent ones. In contrast, the electronic spectrum below the Lifshitz transition (if $|\epsilon| < |\epsilon_L|$) has a more complicated structure. If the given k_y intersects a single Dirac cone in the Fermi surface of the sample then the four modes behave as before, but for some values of k_y zero or two Dirac cones may be intersected, yielding four evanescent modes or four

real propagating modes, respectively.

The wavefunctions inside and outside the barrier, are thus given by:

i) in the source lead ($x < 0$)

$$\psi_1(x) = \phi_1 e^{ik_x^{(1)}x} + r\phi_2 e^{ik_x^{(2)}x} + \beta_1\phi_4 e^{ik_x^{(4)}x} \quad (4.8)$$

ii) in the sample ($0 < x < L_x$)

$$\psi_2(x) = \sum_{n=1}^4 \alpha_n \varphi_n e^{iq_x^{(n)}x} \quad (4.9)$$

iii) in the drain lead ($x > L_x$)

$$\psi_3(x) = t\phi_1 e^{ik_x^{(1)}x} + \beta_2\phi_3 e^{ik_x^{(3)}x} \quad (4.10)$$

where $k_x^{(1)}$ ($k_x^{(2)}$) identifies as a forward (backward) travelling wave. The shrinking (growing) evanescent wave is identified by the complex wavevector $k_x^{(3)}$ ($k_x^{(4)}$). Finally, the spinors associated with the electronic wavefunctions are given by

$$\begin{aligned} \phi_n &= \begin{pmatrix} 1 \\ s\xi^{(n)} \end{pmatrix} = \begin{pmatrix} 1 \\ s \frac{\tilde{k}^{(n)2} + 2\tilde{k}^{(n)\dagger}}{|\tilde{\epsilon} - \tilde{V}_{\text{lead}}|} \end{pmatrix} \\ \varphi_n &= \begin{pmatrix} 1 \\ s'\chi^{(n)} \end{pmatrix} = \begin{pmatrix} 1 \\ s' \frac{\tilde{q}^{(n)2} + 2\tilde{q}^{(n)\dagger} + \tilde{a}^\dagger}{|\tilde{\epsilon} - \tilde{D}^{(s)}|} \end{pmatrix} \end{aligned} \quad (4.11)$$

where $\tilde{k}^{(n)} = k^{(n)}/k_0$ and $\tilde{q}^{(n)} = q^{(n)}/k_0$, with $k^{(n)} = (k_x^{(n)} + ik_y)$, $q^{(n)} = (q_x^{(n)} + ik_y)$, $s = \text{sgn}(\epsilon - V_{\text{lead}})$ and $s' = \text{sgn}(\epsilon - D^{(s)})$. We now impose the continuity of the wavefunction Ψ and of $d\Psi/dx$ at the barrier boundaries ($x = 0$, $x = L_x$) and write the resulting set of linear equations in the form

$$\mathcal{A} = \mathcal{M}\mathcal{B} \quad (4.12)$$

where \mathcal{M} is the matrix

$$\mathcal{M} = \begin{pmatrix}
-1 & -1 & 1 & 1 & 1 & 1 & 0 & 0 \\
-s\xi^{(2)} & -s\xi^{(4)} & s'\chi^{(1)} & s'\chi^{(2)} & s'\chi^{(3)} & s'\chi^{(4)} & 0 & 0 \\
-ik_x^{(2)} & -ik_x^{(4)} & iq_x^{(1)} & iq_x^{(2)} & iq_x^{(3)} & iq_x^{(4)} & 0 & 0 \\
-isk_x^{(2)}\xi^{(2)} & -isk_x^{(4)}\xi^{(4)} & is'q_x^{(1)}\chi^{(1)} & is'q_x^{(2)}\chi^{(2)} & is'q_x^{(3)}\chi^{(3)} & is'q_x^{(4)}\chi^{(4)} & 0 & 0 \\
0 & 0 & e^{iq_x^{(1)}L} & e^{iq_x^{(2)}L} & e^{iq_x^{(3)}L} & e^{iq_x^{(4)}L} & -e^{ik_x^{(1)}L} & -e^{ik_x^{(3)}L} \\
0 & 0 & s'\chi^{(1)}e^{iq_x^{(1)}L} & s'\chi^{(2)}e^{iq_x^{(2)}L} & s'\chi^{(3)}e^{iq_x^{(3)}L} & s'\chi^{(4)}e^{iq_x^{(4)}L} & -s\xi^{(1)}e^{ik_x^{(1)}L} & -s\xi^{(3)}e^{ik_x^{(3)}L} \\
0 & 0 & iq_x^{(1)}e^{iq_x^{(1)}L} & iq_x^{(2)}e^{iq_x^{(2)}L} & iq_x^{(3)}e^{iq_x^{(3)}L} & iq_x^{(4)}e^{iq_x^{(4)}L} & -ik_x^{(1)}e^{ik_x^{(1)}L} & -ik_x^{(3)}e^{ik_x^{(3)}L} \\
0 & 0 & is'q_x^{(1)}\chi^{(1)}e^{iq_x^{(1)}L} & is'q_x^{(2)}\chi^{(2)}e^{iq_x^{(2)}L} & is'q_x^{(3)}\chi^{(3)}e^{iq_x^{(3)}L} & is'q_x^{(4)}\chi^{(4)}e^{iq_x^{(4)}L} & -isk_x^{(1)}\xi^{(1)}e^{ik_x^{(1)}L} & -isk_x^{(3)}\xi^{(3)}e^{ik_x^{(3)}L}
\end{pmatrix} \quad (4.13)$$

and \mathcal{A} is given by the vector

$$\mathcal{A} = \left(1, s\chi^{(1)}, ik_x^{(1)}, isk_x^{(1)}\chi^{(1)}, 0, 0, 0, 0 \right)^T \quad (4.14)$$

and finally \mathcal{B} contains all the amplitudes of the electronic wave functions including the transmission coefficient t ,

$$\mathcal{B} = \left(r, \beta_1, \alpha_1, \alpha_2, \alpha_3, \alpha_4, t, \beta_2 \right)^T \quad (4.15)$$

where $\xi^{(n)}$ and $\chi^{(n)}$ are defined in Eq 4.11. We can then solve the resulting set of linear equations for \mathcal{B} to find the transmission coefficient t at each value of k_y and calculate the corresponding transmission probability $T(k_y)$. Once the transmission probability has been deduced, we employ the Landauer formalism to study the conductance and Fano factor of bilayer graphene with trigonal warping. We choose the sample to have a geometry where $L_y \gg L_x$. This choice has been shown to make the microscopic details of the edges immaterial in the calculation of the ballistic conductance.[15] This assumption is thus important to address the universal properties of ballistic transport in bilayer graphene, especially since the two investigated crystallographic orientations ($\theta = 0$ and $\theta = \pi/2$) have different microscopic edges.

Due to the finite width of the sample, k_y is quantized as $k_y^{(n)} = n\pi/L_y$ where $n = \pm 1, \pm 2, \dots$. The conductance and Fano factor are then given by

$$G = \frac{4e^2}{h} \sum_{n=-N}^N T(k_y^{(n)}) \quad (4.16)$$

$$F = \frac{\sum_{n=-N}^N T(k_y^{(n)})[1 - T(k_y^{(n)})]}{\sum_{n=-N}^N T(k_y^{(n)})}, \quad (4.17)$$

where the prefactor 4 in the Landauer conductance formula is due to the spin and valley degeneracy, and the summation is performed over all transverse modes $k_y^{(n)}$ up to the Fermi wavevector in the leads k_F , yielding $N = \text{int}(k_F L_y / \pi)$.

4.5 Results and discussion

The transmission probability due to the low energy electronic spectrum of trigonally warped bilayer graphene in the absence and presence of strain is presented in Fig. 4.4 for the two different crystallographic orientations $\theta = 0$ and $\theta = \pi/2$. Several Fabry-Perot resonances appear in the transmission, associated with the interference between reflected plane waves in the sample. The

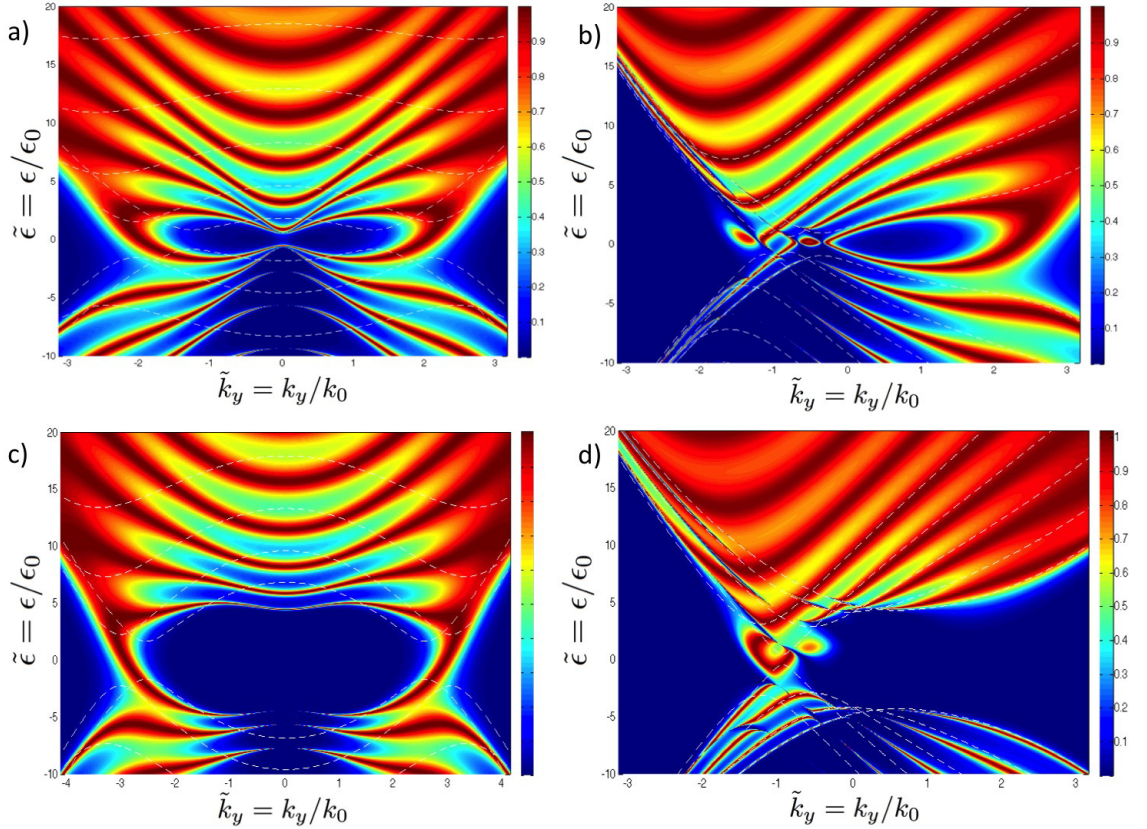


Figure 4.4: Transmission probability as a function of the transverse wavevector and energy across a sample of length $L_x = 100$ nm with highly electron doped leads ($V_{\text{lead}} = -50 \epsilon_L$). Panel a) shows the transmission in the absence of strain ($\tilde{\alpha} = 0$) for the crystal orientation $\theta = 0$, while in panel b) $\tilde{\alpha} = 0$ and $\theta = \pi/2$. Panel c) shows the transmission in presence of strain, with $\tilde{\alpha} = 5$ and $\theta = 0$, while in panel d) $\tilde{\alpha} = 5$ and $\theta = \pi/2$. In all plots the white dashed lines indicate the first few approximate Fabry-Perot resonances obtained from the electronic spectrum in Eq. (4.6) by quantising the longitudinal wavevector as $k_x = n\pi/L_x$, with n an integer.

transmission plots in the absence of strain in Fig. 4.4a ($\theta = 0$) and Fig. 4.4b ($\theta = \pi/2$) show sig-

natures of the Lifshitz transition at $\tilde{\epsilon} = \pm 1$. We can identify a n-n-n region for energies $\tilde{\epsilon} > 0$ and a n-p-n region for energies $\tilde{\epsilon} < 0$. In the latter regime, at normal incidence ($\tilde{k}_y = 0$) we observe perfect reflection for $\tilde{\epsilon} < -1$ (a characteristic signature of suppressed Klein tunnelling in bilayers) and finite transmission below the Lifshitz transition. Close to the neutrality point perfect transmission can be seen near the values of \tilde{k}_y corresponding to the positions of isolated Dirac cones. In contrast, the values of \tilde{k}_y that intersect two cones are associated with a suppressed, though finite, transmission. This phenomenon is mostly pronounced at crystallographic orientations where the central Dirac cone, with Berry phase $-\pi$, lies along the same \tilde{k}_y as one of the outer Dirac cones, with Berry phase π , a configuration that occurs at $\theta = n\pi/3$ where $n = 0, 1, \dots, 5$. This effect can be seen e.g. in Fig. 4.4a (i.e. for $\theta = 0$) at $\tilde{k}_y = 0$ for $|\epsilon| < |\epsilon_L|$, and is attributed to the opposite winding of the pseudo spins around the two Dirac cones involved.

Fig. 4.4c ($\theta = 0$) and Fig. 4.4d ($\theta = \pi/2$) show the effect on the transmission probability of a uniaxial strain characterised by $\tilde{\alpha} = 5$. This is identified as the "large strain regime" as $\tilde{\alpha}$ is much larger than the critical value $\tilde{\alpha} = 1$ needed for two Dirac cones to merge in the case when the deformation is applied along a direction $\phi = \pi(2n + 1)/3$ (in the current work we consider $\phi = 0$). The annihilation of Dirac cones beyond a critical strain and the associated deformation-induced Lifshitz transition produce the disappearance of transmission resonances at low energy. This is particularly evident in the $\theta = \pi/2$ case where the resonance around $\tilde{k}_y \simeq 2.3$ at $\tilde{\epsilon} = 0$ disappears altogether. In contrast, the transmission pattern at the neutrality point for the orientation $\theta = 0$ shows less dramatic qualitative changes under strain, due to the destructive interference already occurring at $\tilde{k}_y = 0$ in the strain-free regime. In addition, strain induces a significant increase in the range of energies where transmission is suppressed around $\tilde{\epsilon} = 0$. Both these effects will contribute to qualitative and quantitative changes in the conductance, Eq. (4.16), between different crystallographic orientations. It has to be pointed out that the value $\tilde{\alpha} = 5$ corresponds to a relatively small uniaxial strain of $\delta L_x/L_x \approx 4 \cdot 10^{-3}$. It is thus likely that a significant fraction of suspended graphene devices will effectively operate in this "large strain regime", with strain being induced by the natural tension present in the samples due to the source and drain contacts.

The location $\epsilon_{\text{res}}^{(n)}(k_y)$ of Fabry-Perot resonances has been successfully approximated in the case of purely parabolic dispersion by quantising the longitudinal wavevector as $k_x = n\pi/L_x$ (with n an integer) into the electronic band structure.[16] Performing the same analysis here, with the dispersion deduced from Eq. (4.6), we deduce the resonances indicated as white dashed lines in

Fig. 4.4. Due to the complexity of the trigonally warped spectrum at low energy, this approximation cannot capture all the fine details of the calculated transmission resonances for every crystallographic orientation, though the agreement in the $\theta = \pi/2$ case is rather good. However, the approximated resonance lines correctly reproduce the qualitative features and the relevant energy scales involved in the transmission pattern of Fig. 4.4.

In Fig. 4.5 we present the results for the conductivity $\sigma = GL_x/L_y$ and Fano factor of trigonally warped bilayer graphene, deduced from the transmission probability above. The asymmetric behaviour in energy of the conductivity and noise plots has been reported previously,[16] and stems from the relatively small doping in the leads with respect to the A1-B2 hopping energy scale γ_1 .

We first discuss results in the absence of strain. In this case, Fig. 4.5a shows the conductivity as a function of energy (and thus also of doping level) for two different crystallographic orientations ($\theta = 0$, blue line and $\theta = \pi/2$ orange line). Our analysis confirms the finite conductivity σ_{min} at the neutrality point in ballistic graphene devices. Different theoretical studies have proposed a variety of values for σ_{min} , depending on the details of the electronic spectrum, among which $\sigma_0 = 4e^2/\pi h$ [28] in monolayers with a linear dispersion, $2\sigma_0$ [16, 29] for bilayers with a simplified parabolic spectrum and $6\sigma_0$ for unstrained bilayers with the inclusion of trigonal warping.[3, 30, 31] Our calculation shows a minimal conductivity $\sigma_{min} \approx 6.4\sigma_0$ for $\theta = 0$, which differs slightly from that reported by other authors. This is understood to be due to the use of the two-bands low energy Hamiltonian, as the transmission at $\tilde{\epsilon} = 0$ is sensitive to the form of the modes in the leads.[16] The result $\sigma_{min} = 6\sigma_0$ would be retrieved in the limit $V_{lead} \rightarrow -\infty$.

Two sharp peaks in the conductivity are visible at energies close to the Lifshitz transition ($\tilde{\epsilon} = \pm 1$). Similar non-monotonic features have been reported in a recent work in which a Lifshitz transition was induced by strain into an otherwise purely parabolic spectrum.[22] Our analysis shows that the inclusion of trigonal warping implies that a Lifshitz transition is always present in the electronic spectrum, leading to sharp peaks in the conductivity even at zero applied strain. In addition, step-like features equally spaced in energy appear at higher doping. The peaks and steps in conductivity are associated with local extremal points in the transmission resonances depicted in Fig. 4.4. These can be interpreted in terms of the approximated resonances $\epsilon_{res}^{(n)}(k_y)$. A close inspection reveals that the lowest sub-bands with $n = 1$ and $n = 2$ exhibit almost degenerate local

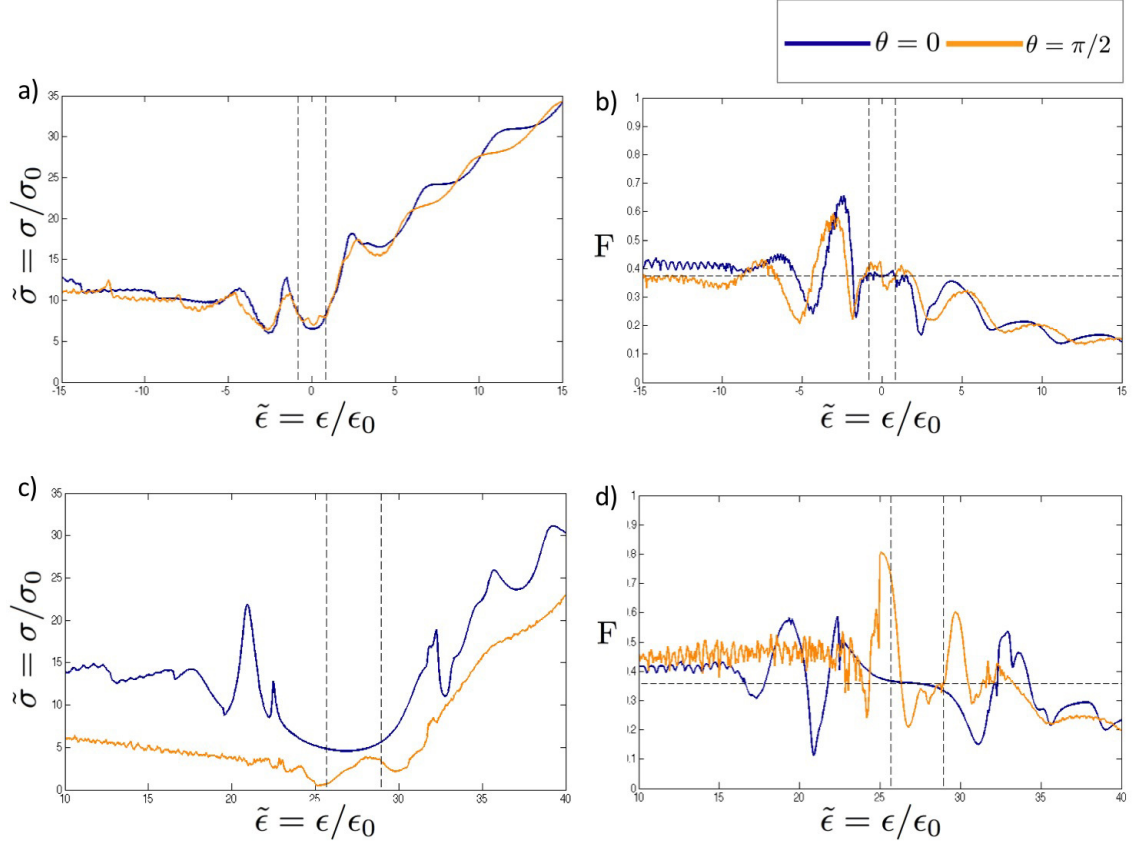


Figure 4.5: Conductivity and Fano factor as a function of energy for strained and unstrained trigonally warped bilayer graphene. Here the potential in the leads is set to $V_{\text{lead}} = -50 \epsilon_L$, with sample geometry $L_x = 100 \text{ nm}$ and $L_y = 1 \mu\text{m}$. Here $\sigma_0 = 4e^2/\pi h$ and $\epsilon_0 = 1.6\text{meV}$. Each plot shows two different crystal orientations, $\theta = 0$ (blue) and $\theta = \pi/2$ (orange). Panel a) shows the conductivity for unstrained bilayer graphene and panel b) the corresponding Fano factor. Panel c) shows the conductivity for strained bilayer graphene with $\tilde{\alpha} = 5$ and panel d) the corresponding Fano factor. In all plots the two vertical dashed lines indicate the position of the minimum of the lowest resonant sub-band $\epsilon_{\text{res}}^{(1)}(k_y)$. Additionally, the horizontal dashed lines in the Fano factor plots indicate the value of F at the Dirac point in the $\theta = 0$ case.

extremal points with $\partial\epsilon_{\text{res}}^{(n)}(k_y)/\partial k_y = 0$ for $\tilde{\epsilon} \sim 1$. These lead to a broad transmission resonance over a large range of k_y , yielding van Hove singularities in the corresponding effective 1D density of states, which ultimately result in sharp local maxima of the conductance as given by Eq. (4.16).

Experimental studies so far succeeded in detecting the minimal conductivity of σ_0 only in ballistic monolayer graphene devices[18, 32] but have failed to support the theoretical predictions for bilayer samples. This discrepancy is expected to be due to smooth long range disorder present in real graphene devices as well as from possible phase transitions in the correlated ground state, opening small gaps in the spectrum at very low temperatures.[33] Due to these difficulties, we thus focus on the shot noise, which has been shown to be a reliable tool to characterise the universal

properties of charge carriers even in the low bias region, with a good agreement between theory and experiment in monolayer graphene.[17, 18]

In Fig. 4.5b we present the Fano factor as a function of energy for the two different crystallographic orientations $\theta = 0$ and $\theta = \pi/2$. Even in presence of trigonal warping in the electronic spectrum, the Fano factor at the neutrality point $\tilde{\epsilon} = 0$ preserves a pseudo-diffusive value of $F \simeq 0.37$. This value is slightly larger than the Fano factor of $F = 1/3$ predicted in graphene monolayers[15] and in bilayers with a simplified parabolic dispersion.[16, 29] As discussed before for the minimal conductivity, the result $F = 1/3$ would be recovered in the limit $V_{\text{lead}} \rightarrow \infty$.

The main difference introduced by trigonal warping relates to the energy range over which the Fano factor takes an approximately constant pseudo-diffusive value near the Dirac point. In fact, this range is significantly broader than in the case when considering only the parabolic electronic spectrum. This energy interval is governed by the position in energy of the lowest extremal points for the first resonance in the transmission, and is given by $\Delta\epsilon = 2\epsilon_{\text{res}}^{(1)}$ where $\epsilon_{\text{res}}^{(n)}$ is the minimum of the n -th resonance $\epsilon_{\text{res}}^{(n)}(k_y)$. The position of the first resonance in the transmission of bilayer graphene with a parabolic electronic spectrum has been estimated by Snyman et al.[16] as $\epsilon_{\text{res}}^{(1),\text{para}}(k_y = 0) = \pi^2 \hbar^2 v^2 / \gamma_1 L_x^2$ and for monolayers as $\epsilon_{\text{res}}^{(1),\text{mono}}(k_y = 0) = \pi \hbar v / L_x$. [15] According to these estimates, the energy interval characterised by pseudo-diffusive transport in a bilayer is smaller than in a monolayer by a factor $\pi \hbar v / \gamma_1 L_x$ (which is very small in any ballistic sample). This fact would make it virtually impossible to detect experimentally the pseudo-diffusive regime and the oscillations in the Fano factor in bilayer devices.

The reconstruction of the electronic spectrum due to trigonal warping however dramatically increases the pseudo-diffusive energy range, with important consequences on the feasibility of the experimental observation of the predicted features in the Fano factor. In fact, performing a similar analysis as above in bilayer graphene with trigonal warping we look for the minima of the first sub-band $\epsilon_{\text{res}}^{(1)}(k_y)$. As shown in Fig. 4.4 these do not appear at $k_y = 0$ but are loosely associated with the outer Dirac cones. Solving for the energy minima of the $n = 1$ sub-bands gives $\epsilon_{\text{res}}^{(1)} \approx \pm 0.83 \epsilon_L$ (for $\theta = 0$) in a realistic device with $L_x = 100$ nm. These values are marked on Fig. 4.5 by dashed vertical lines. Although the analytical expression for $\epsilon_{\text{res}}^{(1)}$ is complicated by the complex nature of the trigonally warped electronic spectrum, we can estimate it by quantising the longitudinal wavevector in the outer elliptical Dirac cones, yielding a characteristic energy scale $\Delta\epsilon^{\text{trig}} \sim \pi \hbar v_3 / L_x$. Thus, the comparison between the energy scale at which the first resonance

occurs in the parabolic spectrum and in the trigonally warped case gives

$$\frac{\Delta\epsilon^{trig}}{\Delta\epsilon^{para}} \approx 10^2 \frac{L_x}{\mu m} . \quad (4.18)$$

As a consequence, the inclusion of trigonal warping increases by orders of magnitude the width of the energy interval showing pseudo-diffusive transport around the Dirac point. This fact is crucial for the experimental observability of the predicted features in ballistic transport through high-quality bilayer graphene devices.

In presence of deformations, the effects associated with the reconstruction of the electronic spectrum at low energy are even more pronounced. Not only does strain induce the annihilation of massless cones (cf. Fig. 4.2) and the disappearance of transmission resonances, but it also dramatically increases the Lifshitz transition energy, and thus the range over which transmission is suppressed around the neutrality point, as shown in Fig. 4.4. The two remaining massless Dirac cones at high strain exhibit an increased, strain-dependent, group velocity. As a consequence, the energy range associated with the pseudo-diffusive transport regime is expected to increase with increasing strain.

Fig. 4.5c shows the conductivity of trigonally warped, strained bilayer graphene with $\tilde{\alpha} = 5$. As elastic distortions are only present in the sample, the deformation potential shifts the position of the neutrality point which, for $\tilde{\alpha} = 5$ occurs at $\tilde{\epsilon} \simeq 27.3$. The shift of the Dirac point in the sample with respect to the leads creates an additional potential barrier, as recently reported in molecular graphene systems.[34] In this "large strain regime" our results for the ballistic conductivity essentially reproduce those of Gradinar et al.[22] including a non-monotonic dependence on the energy due to the Lifshitz transition in the electronic spectrum. The reconstruction of the electronic spectrum creating a structure of two Dirac cones can suppress transmission resonances (cf. Fig. 4.4) leading to a slight decrease of the minimal conductivity.[31] This is most noticeable in the $\theta = \pi/2$ orientation, where σ_{min} drops to about $2.7 \sigma_0$, while the corresponding value for $\theta = 0$ is much less affected.

The Fano factor for strained trigonally warped bilayer graphene is shown in Fig. 4.5d. It is evident that, around the shifted neutrality point, the energy range characterised by the pseudo-diffusive value of $F \simeq 1/3$ has increased. Indeed, for $\tilde{\alpha} = 5$ the minimum of the $n = 1$ resonant sub-band increases to $\epsilon_{res}^{(1)} = 1.64 \epsilon_L$ (for $\theta = 0$), which is approximately twice as large as in the

unstrained case. To understand this increase we shall look at the effect of strain on the group velocity $v_s(\alpha)$ of the low energy massless Dirac cones well below the Lifshitz transition energy. This will allow for an estimation of the energy scale of the first resonance as $\epsilon_{\text{res}}^{(1)} \sim \pi\hbar v_s(\alpha)/L_x$. In the relevant highly strained regime ($\tilde{\alpha} \gg 1$) α dominates over the energy scale associated with trigonal warping, and the problem reduces to that of bilayer graphene with a parabolic spectrum in presence of strain. In this regime the positions of the two Dirac cones are given by the complex wave vectors $q_0 = \pm i\sqrt{2m\alpha}/\hbar$. Expanding the Hamiltonian around the new positions of the Dirac cones (i.e. $k = q_0 + \delta k$) we obtain

$$H_{\text{eff}} = \pm i\hbar \sqrt{\frac{2\alpha}{m}} \begin{pmatrix} 0 & \delta k^\dagger \\ \delta k & 0 \end{pmatrix}, \quad (4.19)$$

yielding the renormalised group velocity $v_s(\alpha) = \sqrt{2\alpha/m}$ which is much larger than v_3 in the regime $\tilde{\alpha} \gg 1$. As a consequence, strain further increases the energy range exhibiting the pseudo-diffusive value of the Fano factor $F \simeq 1/3$ around the neutrality point to the renormalised value $\Delta\epsilon_s^{\text{trig}} = \Delta\epsilon^{\text{trig}} \sqrt{\tilde{\alpha}}$. Given the amount of strain normally present in suspended graphene samples, we thus expect that the vast majority of realistic devices should show pseudo-diffusive transport over an energy range much larger than that expected for unstrained trigonally warped bilayer graphene, and orders of magnitude larger than theoretically predicted with the simplified parabolic electronic dispersion. Due to these estimates, it is likely that trigonal warping and strain in ballistic bilayer graphene devices are the crucial ingredients enabling the experimental detection of $F \simeq 1/3$ and the resolution of its oscillations in energy in the vicinity of the neutrality point. Our analysis highlights the effects of the coupling between electrons and deformations on the quantum transport through high-quality graphene devices, in analogy with those recently reported in other carbon-based nano-electromechanical systems.[35, 36, 37, 38, 39, 40, 41]

4.6 Conclusion

In summary the presence of a Lifshitz transition in the electronic spectrum results in anomalies which are clearly visible in the conductivity, and whose position in energy grows with the amount of strain in the sample. Regarding the shot noise the spectrum reconstruction due to trigonal warping at low energy does not affect the pseudo-diffusive result $F = 1/3$ at the neutrality point.

However, the inclusion of trigonal warping dramatically increases the energy range in which the pseudo-diffusive result holds with respect to previous theoretical predictions in which this contribution has been neglected. Strain leads to a further reconstruction of the spectrum at low energy and to an increase in the Lifshitz transition energy. This ultimately leads to an additional increase of the characteristic energy range associated with the pseudo-diffusive transport in the vicinity of the neutrality point and with the oscillations in the conductivity and in the Fano factor. As a result, strain will ultimately help the experimental observability of these transport signatures in high-quality samples.

Bibliography

- [1] J. Nilsson, A. H. Castro Neto, N. M. R. Peres, and F. Guinea, “Electron-electron interactions and the phase diagram of a graphene bilayer,” *Physical Review B*, vol. 73, pp. 214418–, 06 2006.
- [2] E. McCann and V. I. Fal’ko, “Landau-level degeneracy and quantum hall effect in a graphite bilayer,” *Physical Review Letters*, vol. 96, pp. 086805–, 03 2006.
- [3] M. Koshino and T. Ando, “Transport in bilayer graphene: Calculations within a self-consistent born approximation,” *Physical Review B*, vol. 73, pp. 245403–, 06 2006.
- [4] K. Kechedzhi, V. I. Fal’ko, E. McCann, and B. L. Altshuler, “Influence of trigonal warping on interference effects in bilayer graphene,” *Physical Review Letters*, vol. 98, pp. 176806–, 04 2007.
- [5] Y.-W. Son, S.-M. Choi, Y. P. Hong, S. Woo, and S.-H. Jhi, “Electronic topological transition in sliding bilayer graphene,” *Physical Review B*, vol. 84, pp. 155410–, 10 2011.
- [6] M. Mucha-Kruczyński, I. L. Aleiner, and V. I. Fal’ko, “Strained bilayer graphene: Band structure topology and landau level spectrum,” *Physical Review B*, vol. 84, pp. 041404–, 07 2011.
- [7] B. Verberck, B. Partoens, F. M. Peeters, and B. Trauzettel, “Strain-induced band gaps in bilayer graphene,” *Physical Review B*, vol. 85, pp. 125403–, 03 2012.
- [8] E. Mariani, A. J. Pearce, and F. von Oppen, “Fictitious gauge fields in bilayer graphene,” *Physical Review B*, vol. 86, pp. 165448–, 10 2012.

- [9] O. Vafek and K. Yang, “Many-body instability of coulomb interacting bilayer graphene: Renormalization group approach,” *Physical Review B*, vol. 81, pp. 041401–, 01 2010.
- [10] Y. Lemonik, I. L. Aleiner, C. Toke, and V. I. Fal’ko, “Spontaneous symmetry breaking and lifshitz transition in bilayer graphene,” *Physical Review B*, vol. 82, pp. 201408–, 11 2010.
- [11] B. E. Feldman, J. Martin, and A. Yacoby, “Broken-symmetry states and divergent resistance in suspended bilayer graphene,” *Nat Phys*, vol. 5, pp. 889–893, 12 2009.
- [12] A. S. Mayorov, D. C. Elias, M. Mucha-Kruczynski, R. V. Gorbachev, T. Tudorovskiy, A. Zhukov, S. V. Morozov, M. I. Katsnelson, V. I. Fal’ko, A. K. Geim, and K. S. Novoselov, “Interaction-driven spectrum reconstruction in bilayer graphene,” *Science*, vol. 333, no. 6044, pp. 860–863, 2011.
- [13] J. Velasco, L. Jing, W. Bao, Y. Lee, P. Kratz, V. Aji, M. Bockrath, C. Lau, C. Varma, R. Stillwell, D. Smirnov, F. Zhang, J. Jung, and A. MacDonald, “Transport spectroscopy of symmetry-broken insulating states in bilayer graphene,” *Nat Nano*, vol. 7, pp. 156–160, 03 2012.
- [14] Y. M. Blanter and M. Büttiker, “Shot noise in mesoscopic conductors,” *Physics Reports*, vol. 336, pp. 1–166, 9 2000.
- [15] J. Tworzydło, B. Trauzettel, M. Titov, A. Rycerz, and C. W. J. Beenakker, “Sub-poissonian shot noise in graphene,” *Physical Review Letters*, vol. 96, pp. 246802–, 06 2006.
- [16] I. Snymán and C. W. J. Beenakker, “Ballistic transmission through a graphene bilayer,” *Physical Review B*, vol. 75, pp. 045322–, 01 2007.
- [17] L. DiCarlo, J. R. Williams, Y. Zhang, D. T. McClure, and C. M. Marcus, “Shot noise in graphene,” *Physical Review Letters*, vol. 100, pp. 156801–, 04 2008.
- [18] R. Danneau, F. Wu, M. F. Craciun, S. Russo, M. Y. Tomi, J. Salmilehto, A. F. Morpurgo, and P. J. Hakonen, “Shot noise in ballistic graphene,” *Physical Review Letters*, vol. 100, pp. 196802–, 05 2008.
- [19] A. Fay, R. Danneau, J. K. Viljas, F. Wu, M. Y. Tomi, J. Wengler, M. Wiesner, and P. J. Hakonen, “Shot noise and conductivity at high bias in bilayer graphene: Signatures of electron-optical phonon coupling,” *Physical Review B*, vol. 84, pp. 245427–, 12 2011.

- [20] P. San-Jose, E. Prada, and D. S. Golubev, “Universal scaling of current fluctuations in disordered graphene,” *Physical Review B*, vol. 76, pp. 195445–, 11 2007.
- [21] C. H. Lewenkopf, E. R. Mucciolo, and A. H. Castro Neto, “Numerical studies of conductivity and fano factor in disordered graphene,” *Physical Review B*, vol. 77, pp. 081410–, 02 2008.
- [22] D. A. Gradinar, H. Schomerus, and V. I. Fal’ko, “Conductance anomaly near the lifshitz transition in strained bilayer graphene,” *Physical Review B*, vol. 85, pp. 165429–, 04 2012.
- [23] H. Suzuura and T. Ando, “Phonons and electron-phonon scattering in carbon nanotubes,” *Physical Review B*, vol. 65, pp. 235412–, 05 2002.
- [24] E. Mariani and F. von Oppen, “Flexural phonons in free-standing graphene,” *Physical Review Letters*, vol. 100, pp. 076801–, 02 2008.
- [25] E. Mariani and F. von Oppen, “Electron-vibron coupling in suspended carbon nanotube quantum dots,” *Physical Review B*, vol. 80, pp. 155411–, 10 2009.
- [26] E. Mariani and F. von Oppen, “Temperature-dependent resistivity of suspended graphene,” *Physical Review B*, vol. 82, pp. 195403–, 11 2010.
- [27] E. Cappelluti and G. Profeta, “Hopping-resolved electron-phonon coupling in bilayer graphene,” *Physical Review B*, vol. 85, pp. 205436–, 05 2012.
- [28] M. I. Katsnelson, “Zitterbewegung, chirality, and minimal conductivity in graphene,” *Eur. Phys. J.*, vol. 51, no. 2, pp. 157–160, 2006.
- [29] M. I. Katsnelson, “Minimal conductivity in bilayer graphene,” *Eur. Phys. J.*, vol. 52, no. 2, pp. 151–153, 2006.
- [30] J. Cserti, A. Csordás, and G. Dávid, “Role of the trigonal warping on the minimal conductivity of bilayer graphene,” *Physical Review Letters*, vol. 99, pp. 066802–, 08 2007.
- [31] G. Dávid, P. Rakytá, L. Oroszlány, and J. Cserti, “Effect of the band structure topology on the minimal conductivity for bilayer graphene with symmetry breaking,” *Physical Review B*, vol. 85, pp. 041402–, 01 2012.
- [32] F. Miao, S. Wijeratne, Y. Zhang, U. C. Coskun, W. Bao, and C. N. Lau, “Phase-coherent transport in graphene quantum billiards,” *Science*, vol. 317, no. 5844, pp. 1530–1533, 2007.

- [33] W. Bao, J. Velasco, F. Zhang, L. Jing, B. Standley, D. Smirnov, M. Bockrath, A. H. MacDonald, and C. N. Lau, "Evidence for a spontaneous gapped state in ultraclean bilayer graphene," *Proceedings of the National Academy of Sciences*, vol. 109, no. 27, pp. 10802–10805, 2012.
- [34] K. K. Gomes, W. Mar, W. Ko, F. Guinea, and H. C. Manoharan, "Designer dirac fermions and topological phases in molecular graphene," *Nature*, vol. 483, pp. 306–310, 03 2012.
- [35] J. Koch and F. von Oppen, "Franck-condon blockade and giant fano factors in transport through single molecules," *Physical Review Letters*, vol. 94, pp. 206804–, 05 2005.
- [36] S. Sapmaz, P. Jarillo-Herrero, Y. M. Blanter, C. Dekker, and H. S. J. van der Zant, "Tunneling in suspended carbon nanotubes assisted by longitudinal phonons," *Physical Review Letters*, vol. 96, pp. 026801–, 01 2006.
- [37] R. Leturcq, C. Stampfer, K. Inderbitzin, L. Durrer, C. Hierold, E. Mariani, M. G. Schultz, F. von Oppen, and K. Ensslin, "Franck-condon blockade in suspended carbon nanotube quantum dots," *Nat Phys*, vol. 5, pp. 327–331, 05 2009.
- [38] G. Weick, F. Pistolesi, E. Mariani, and F. von Oppen, "Discontinuous euler instability in nanoelectromechanical systems," *Physical Review B*, vol. 81, pp. 121409–, 03 2010.
- [39] F. Cavaliere, E. Mariani, R. Leturcq, C. Stampfer, and M. Sassetti, "Asymmetric franck-condon factors in suspended carbon nanotube quantum dots," *Physical Review B*, vol. 81, pp. 201303–, 05 2010.
- [40] G. Piovano, F. Cavaliere, E. Paladino, and M. Sassetti, "Coherent properties of nanoelectromechanical systems," *Physical Review B*, vol. 83, pp. 245311–, 06 2011.
- [41] G. Dolcetto, F. Cavaliere, D. Ferraro, and M. Sassetti, "Generating and controlling spin-polarized currents induced by a quantum spin hall antidot," *Physical Review B*, vol. 87, pp. 085425–, 02 2013.

5

Electron-Vibron Coupling in MoS₂

Since the isolation of single layer graphene[1, 2] there has been interest in isolating other layered materials in their two-dimensional form. The transition-metal dichalcogenides (e.g. MoS₂, MoSe₂, WS₂) are layered materials which can be mechanically exfoliated into atomically thin monolayer sheets. These materials have gained recent interest as while their multilayer form is an indirect semiconductor in the monolayer there is a crossover to a direct semiconductor with a band gap in the optical frequency range.[3, 4]

As monolayer transition-metal dichalcogenides consist of a semiconducting membrane, there is much interest to use them to compensate for the low on-off ratios found in graphene, due to its metallic nature and lack of a band gap. They also open up the possibility of exploring both strain engineering and mechanical resonators in a new class of 2D materials. Already MoS₂ has gained particular interest for optical[5, 6] and electronic devices.[7, 8] Indeed, MoS₂ field effect transistors have been experimental realised and possess room temperature mobilities of $200 \text{ cm}^2 \text{ V}^{-1} \text{ s}^{-1}$. [9]

Electronic transport measurements of MoS₂ devices have shown that at low carrier densities and low temperatures transport is mediated by localised impurity states.[10] In this transport regime which is dominated by localised impurity states we enter the regime of Coulomb blockade and conductance resonances, as the localised impurity states act as quantum dots. In the Coulomb blockade regime interactions between electrons suppress the current through the localised quantum dot like state when it is occupied by an electron, this leads to distinctive diamond structure in maps of the conductance over the source drain V_{sd} and back gate voltages V_{bg} . Vibrational effects have been shown to have a strong effect on electronic transport in the Coulomb blockade regime.[11, 12, 13, 14, 15] Tunnelling of electrons through suspended quantum dots has been shown to excite quantised vibrational modes, called vibrons. Electron-vibron coupling leads to vibrational sidebands in the Coulomb blockade regime[11] and in case of strong coupling can lead to the Franck-Condon blockade.[16, 17] In carbon nanotubes electrons have been shown to couple to radial breathing modes[11] and longitudinal stretching modes.[12, 13, 15, 17] Localised electronic states seen in suspended MoS₂ may provide a new arena for observing electron-vibron effects, bypassing the need for complicated electrostatically defined quantum dots.

In this chapter we will focus on MoS₂ as it the most studied of the transition-metal dichalcogenides and its electronic and mechanical properties are the most well understood. It must be stressed that the results presented here are also applicable to any of the transition-metal dichalcogenides, as the form of fictitious gauge fields is governed by the structure of the crystal lattice which is common to all these atomically thin materials. Although the specific parameters of the effective theory describing other transition-metal dichalcogenides will be different to values presented within this work, there will be a qualitative agreement.

MoS₂ possesses impressive elastic properties with a Young's modulus of 0.3TPa, approximately one third of that possessed by graphene.[18, 19] So far no signatures of vibrational effects have been reported in transport experiments and the investigation of the vibrational properties of MoS₂ have been focused on Raman spectroscopy studies,[20] studies of electron-phonon coupling[21, 22] and recently monolayer resonator devices have been reported.[23]

Presently the effects of uniaxial and biaxial strain on monolayer MoS₂ have been studied by density functional theory methods[24, 25, 26, 27, 28] and photoluminescence experiments[29, 30] showing a strain driven crossover from a direct band gap to an indirect band gap. For a complete study of the physics arising from the coupling between electronic and mechanical degrees of free-

dom it is necessary to identify the fictitious gauge fields associated with any arbitrary deformation in transition-metal dichalcogenides, and this will be the main focus of this chapter.

The fictitious gauge fields presented in this chapter may act as a starting point for studying the effect of mechanical deformations on the electronic properties, such as the electron-phonon coupling,[31] the pseudo-magnetic fields which have been predicted and observed in graphene[32, 33] and the modifications of electronic transport properties of mechanical resonators fabricated on MoS_2 .

In this chapter we will focus on the effects of electron-vibron coupling in suspended MoS_2 . Firstly we calculate the dimensionless electron-vibron coupling constants for each vibron mode finding that the longitudinal stretching mode contributes to the dominant coupling. We find that the effect of electron-vibron coupling is highly sample specific and reaches maximum values which are usually smaller than those observed in carbon-based nanostructures.[34] The weakening of the effect as compared to carbon nanostructures is primarily attributed to the larger mass density of the MoS_2 . The small electron-vibron coupling constant suggests that electron-vibron coupling will not typically have a large effect on electronic transport in MoS_2 in most samples and transport regimes.

The structure of this chapter will be as follows. In Section I. we introduce the electronic properties of MoS_2 , using a tight binding model for the continuum states and also considering the highly sample specific localised electronic states. Section II. introduces the elastic theory of long-wavelength phonons in MoS_2 . In Section III. we derive the fictitious gauge fields which arise in MoS_2 under arbitrary elastic deformations. Finally using elements from all previous sections, in Section IV. we derive the electron-vibron coupling constants for all vibron modes of interest for electronic transport and conclude and summarise.

5.1 Electronic Structure of MoS_2

The electronic structure of MoS_2 has been studied by several authors,[35, 36] predominantly by DFT techniques, although low energy Hamiltonians have been suggested based on symmetry arguments[37] and more recently on a tight binding approach.[38, 39]

MoS_2 is comprised of three layers, two (top and bottom) layers of Sulfur and the central layer of Molybdenum. We identify them by the layer index $l = 1$ for the lower Sulfur layer, $l = 2$

for the Molybdenum layer and $l = 3$ for the upper Sulfur layer. The top and bottom Sulfur layers are arranged in a triangular lattice with lattice spacing $d = 3.193 \text{ \AA}$, with the Sulfur atoms on differing layers lying directly atop each other. The central layer consists of an identical triangular lattice of Molybdenum atoms rotated by π with respect to the Sulfur ones. Each layer is separated from its neighbour by an interlayer distance $c = 1.505 \text{ \AA}$.

The planar structure of the three combined layers forms a honeycomb lattice comprising two sublattices (labelled A and B), where the A sublattice is made of Molybdenum atoms and the B sublattice is conversely made of Sulfur atoms, as shown in Fig. 5.1. This gives MoS_2 a planar structure similar to that of graphene but with a broken inversion symmetry due to the different atomic species that make up the two sublattices. The planar vectors connecting the A and B lattice sites are $\mathbf{e}_1 = a(0, -1)$, $\mathbf{e}_2 = a/2(\sqrt{3}, 1)$ and $\mathbf{e}_3 = a/2(-\sqrt{3}, 1)$, where $a = 1.84 \text{ \AA}$. As a consequence, the interatomic distance between each Molybdenum atom and its nearest Sulfur atom is $\tilde{c} = \sqrt{a^2 + c^2} = 2.37 \text{ \AA}$.

The next nearest neighbours are atoms of the same species and on the same sublattice connected by the six vectors $\boldsymbol{\delta}_{1,2} = \pm(\mathbf{e}_1 - \mathbf{e}_3) = \pm a(\sqrt{3}/2, -3/2)$, $\boldsymbol{\delta}_{3,4} = \pm(\mathbf{e}_1 - \mathbf{e}_2) = \pm a(-\sqrt{3}/2, -3/2)$ and $\boldsymbol{\delta}_{5,6} = \pm(\mathbf{e}_2 - \mathbf{e}_3) = \pm a(\sqrt{3}, 0)$.

For our tight-binding analysis of the electronic structure of MoS_2 we consider all hopping terms between nearest neighbour and next nearest neighbour electron orbitals which yields the

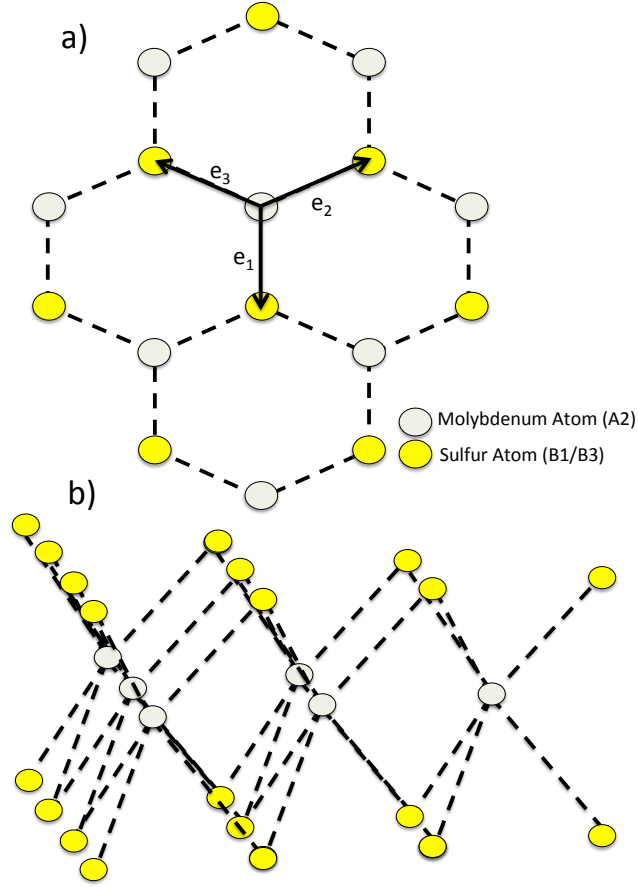


Figure 5.1: The atomic structure of perfect MoS_2 . Panel a) shows a top down view of the honeycomb lattice with the vectors \mathbf{e}_j ($j = 1, 2, 3$) which connect the A and B sublattices. Panel b) shows a side view of the lattice showing the three layered structure.

Hamiltonian

$$\begin{aligned}
 H = & -t_{A2,B1} \sum_{\mathbf{R}_{A2}} \sum_{j=1}^3 |\mathbf{R}_{A2}\rangle \langle \mathbf{R}_{A2} + \mathbf{e}_j - c\hat{\mathbf{z}}| \\
 & -t_{A2,B3} \sum_{\mathbf{R}_{A2}} \sum_{j=1}^3 |\mathbf{R}_{A2}\rangle \langle \mathbf{R}_{A2} + \mathbf{e}_j + c\hat{\mathbf{z}}| \\
 & -t_{B1,B3} \sum_{\mathbf{R}_{B1}} \sum_{j=1}^6 |\mathbf{R}_{B1}\rangle \langle \mathbf{R}_{B1} + \boldsymbol{\delta}_j + 2c\hat{\mathbf{z}}| \\
 & -t_{B1,B3}^{(\perp)} \sum_{\mathbf{R}_{B1}} |\mathbf{R}_{B1}\rangle \langle \mathbf{R}_{B1} + 2c\hat{\mathbf{z}}| \\
 & -t_{B1,B1} \sum_{\mathbf{R}_{B1}} \sum_{j=1}^6 |\mathbf{R}_{B1}\rangle \langle \mathbf{R}_{B1} + \boldsymbol{\delta}_j| \\
 & -t_{A2,A2} \sum_{\mathbf{R}_{A2}} \sum_{j=1}^6 |\mathbf{R}_{A2}\rangle \langle \mathbf{R}_{A2} + \boldsymbol{\delta}_j| \\
 & -t_{B3,B3} \sum_{\mathbf{R}_{B3}} \sum_{j=1}^6 |\mathbf{R}_{B3}\rangle \langle \mathbf{R}_{B3} + \boldsymbol{\delta}_j| + h.c.
 \end{aligned} \tag{5.1}$$

where \mathbf{R}_{sl} is the position of an atom in the sublattice s and layer l , and $|\mathbf{R}_{sl}\rangle$ is the ket associated with the corresponding localised orbital. Here we used the identities $\mathbf{R}_{B1} = \mathbf{R}_{A2} + \mathbf{e}_j - c\hat{\mathbf{z}}$, $\mathbf{R}_{B3} = \mathbf{R}_{A2} + \mathbf{e}_j + c\hat{\mathbf{z}}$, $\mathbf{R}_{B3} = \mathbf{R}_{B1} + 2c\hat{\mathbf{z}}$ for the vertical interlayer hopping terms between layer 1 and 3, and $\mathbf{R}_{B3} = \mathbf{R}_{B1} + \delta_j + 2c\hat{\mathbf{z}}$ for the corresponding skew interlayer terms, and finally for the next nearest neighbour hopping terms $\mathbf{R}_s = \mathbf{R}_{s'} + \delta_j$. In the tight binding approximation $t_{sl,s'l'}$ is the energy scale for electrons hopping from the two neighbouring sites \mathbf{R}_{sl} and $\mathbf{R}_{s'l'}$.

In MoS_2 only a few of these parameters have been obtained by DFT calculations with $t_{A2,B1} = t_{A2,B3} \equiv t \simeq 1.1\text{eV}$, [35] while we label the other hopping parameters as $t_{B1,B3}^{(\perp)} \equiv \gamma$, $t_{B1,B3} \equiv \gamma'$, $t_{B1,B1} \equiv t_{B3,B3} \equiv t'_s$ and $t_{A2,A2} \equiv t'_{Mo}$. Their true values are still unknown but we will show that they may be parameterised by the size of the band gap and the low energy band structure.

In analogy to graphene electronic eigenstates in MoS_2 are described by Bloch states of the form

$$|\psi_{\mathbf{k}}\rangle = \sum_{\mathbf{R}_{B1}} u_{\mathbf{k}}^{(B1)} e^{i\mathbf{k}\cdot\mathbf{R}_{B1}} |\mathbf{R}_{B1}\rangle + \sum_{\mathbf{R}_{A2}} u_{\mathbf{k}}^{(A2)} e^{i\mathbf{k}\cdot\mathbf{R}_{A2}} |\mathbf{R}_{A2}\rangle + \sum_{\mathbf{R}_{B3}} u_{\mathbf{k}}^{(B3)} e^{i\mathbf{k}\cdot\mathbf{R}_{B3}} |\mathbf{R}_{B3}\rangle \quad (5.2)$$

where $u_{\mathbf{k}}^{(sl)}$ is the amplitude of the wavefunction in the sublattice s and layer l at wavevector \mathbf{k} . Therefore in the 3×3 space of the Bloch amplitudes ($u_{\mathbf{k}}^{(B1)}$, $u_{\mathbf{k}}^{(A2)}$, $u_{\mathbf{k}}^{(B3)}$) the Hamiltonian takes the matrix form

$$H = \begin{pmatrix} t'_s |f_{\mathbf{k}}|^2 & -t f_{\mathbf{k}}^* & -\gamma + \gamma' |f_{\mathbf{k}}|^2 \\ -t f_{\mathbf{k}} & t'_{Mo} |f_{\mathbf{k}}|^2 & -t f_{\mathbf{k}} \\ -\gamma + \gamma' |f_{\mathbf{k}}|^2 & -t f_{\mathbf{k}}^* & t'_s |f_{\mathbf{k}}|^2 \end{pmatrix} \quad (5.3)$$

where $f_{\mathbf{k}} = \sum_{j=1}^3 \exp[i\mathbf{k}\cdot\mathbf{e}_j]$. It is convenient to consider symmetric $|\mathbf{R}_{BS}\rangle = (1/\sqrt{2})(|\mathbf{R}_{B1}\rangle + |\mathbf{R}_{B3}\rangle)$ and anti-symmetric $|\mathbf{R}_{BA}\rangle = (1/\sqrt{2})(|\mathbf{R}_{B1}\rangle - |\mathbf{R}_{B3}\rangle)$ combinations of the orbitals localized on the Sulfur atoms.

Due to the honeycomb structure of the lattice MoS_2 will yield Dirac points at \mathbf{K} points of the Brillouin Zone in analogy to graphene, therefore we expand around the two \mathbf{K}_{τ} points in the first Brillouin zone (where $\mathbf{K}_{\tau} = \tau(4\pi/3\sqrt{3}a, 0)$ and $\tau = \pm 1$ is the valley index). In the new basis of the Bloch amplitudes ($u_{\mathbf{k}}^{(BS)}$, $u_{\mathbf{k}}^{(A2)}$, $u_{\mathbf{k}}^{(BA)}$) the matrix Hamiltonian becomes

$$H^{(\tau)} = \begin{pmatrix} -\gamma + 3\gamma' + 3t'_s - \frac{\hbar^2|\mathbf{k}|^2}{2\mu^{(-)}} & v\hbar k^{\dagger} - \frac{\hbar^2 k^2}{2m} & 0 \\ v\hbar k - \frac{\hbar^2 k^{\dagger 2}}{2m} & 3t'_{Mo} - \frac{\hbar^2|\mathbf{k}|^2}{2m_{Mo}} & 0 \\ 0 & 0 & \gamma - 3\gamma' + 3t'_s - \frac{\hbar^2|\mathbf{k}|^2}{2\mu^{(+)}} \end{pmatrix} \quad (5.4)$$

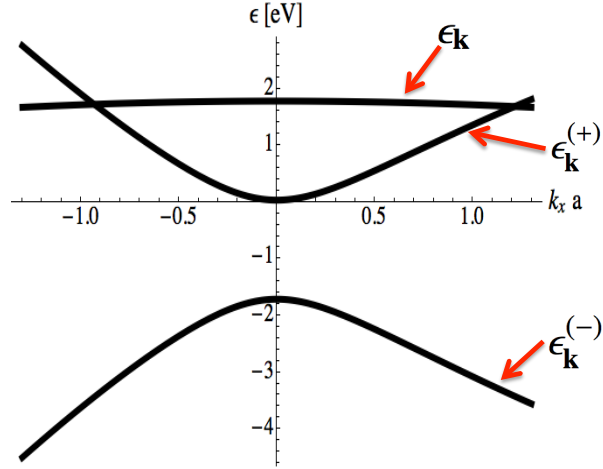


Figure 5.2: The electronic dispersion of MoS₂. Showing a cut along $k_y = 0$ of the three band electronic dispersion of MoS₂ given in Eq. 5.5 with the three bands labeled. The numerical values of the next nearest neighbour hopping energies is unknown therefore for illustrative purposes we have taken them to be $t'_s = t'_{Mo} = 0.01t$ and $\gamma' = 0.01\gamma$, this relationship used between tight binding parameters is of the same order as found in graphene.

where $k = \tau k_x + ik_y$. Here the Fermi velocity is $v = 3at / \sqrt{2}\hbar \approx 4 \times 10^5 \text{ms}^{-1}$ and the mass correction is $m = 4\sqrt{2}\hbar^2/3a^2t \approx 37m_e$. The mass correction which arises from next nearest neighbour hopping between Molybdenum atoms is $m_{Mo} = 2\hbar^2/9a^2t'_{Mo}$ and the reduced mass correction from the next nearest neighbour hopping between Sulfur atoms is $\mu^{(\pm)} = m_s m_\gamma / (m_s \pm m_\gamma)$ where $m_\gamma = 2\hbar^2/9a^2\gamma'$ and $m_s = 2\hbar^2/9a^2t'_s$. Notice that the top left 2×2 block in the space $(u_{\mathbf{k}}^{(BS)}, u_{\mathbf{k}}^{(A2)})$ in Eq 5.4 is equivalent to the Hamiltonian for gapped graphene with the inclusion of terms arising from next nearest neighbour hopping.

We can now diagonalise Eq. 5.4, which yields an electronic spectrum of three bands with dispersion

$$\begin{aligned}
\epsilon_{\mathbf{k}} &= 3t'_s + \gamma - 3\gamma' - \frac{\hbar^2|\mathbf{k}|^2}{2\mu^{(+)}} \\
\epsilon_{\mathbf{k}}^{(\pm)} &= -\frac{\Delta}{2} - \frac{\hbar^2|\mathbf{k}|^2}{4\mu^{(-)}} - \frac{\hbar^2|\mathbf{k}|^2}{4m_{Mo}} \pm \left[\left(\frac{\gamma - 3t'_s - 3\gamma' - 3t'_{Mo}}{2} + \frac{\hbar^2|\mathbf{k}|^2}{4\mu^{(-)}} + \frac{\hbar^2|\mathbf{k}|^2}{4m_{Mo}} \right)^2 \right. \\
&\quad \left. - 3t'_{Mo}(3t'_s - \gamma + 3\gamma') + \frac{\hbar^4|\mathbf{k}|^4}{4m^2} - \frac{\hbar^4|\mathbf{k}|^4}{4\mu^{(-)}m_{Mo}} + \frac{\hbar^3v}{m}|\mathbf{k}|^3 \cos 3\phi + v^2\hbar^2|\mathbf{k}|^2 \right. \\
&\quad \left. + (3t'_s - \gamma + 3\gamma')\frac{\hbar^2|\mathbf{k}|^2}{2m_{Mo}} + \frac{3t'_s\hbar^2|\mathbf{k}|^2}{2\mu^{(-)}} \right]^{\frac{1}{2}}, \tag{5.5}
\end{aligned}$$

where $\tan \phi = k_y/k_x$ and we have introduced $\Delta = \gamma - 3\gamma' + 3t'_{Mo} - 3t'_s$.

These bands are shown in Fig 5.3.a and from the Hamiltonian matrix in Eq. 5.4 we find that the band associated with anti-symmetric charge occupation of the sulfur orbitals (shown on the first line of Eq. 5.5) is only dispersive at second order in the crystal momentum while the other two bands (shown on the final lines of Eq. 5.5) form the conduction and valence bands. There is a direct band gap of energy $\Delta = \gamma - 3\gamma' + 3t'_{Mo} - 3t'_s$ between the conduction and valence band, which has been experimentally observed to be 1.8eV.[4] The band associated with anti-symmetric charge occupation of the sulfur orbitals does not couple with either of the conduction or valence band and exists at a large energy. As such it does not play a significant role in transport experiments.

We include up to the second leading term in crystal momentum of the nearest neighbour hopping and next nearest neighbour hopping as this is the minimum requirement for all three bands to be dispersive and reach an agreement with DFT results. Due to the inclusion of the second leading term the band structure also shows trigonal warping which some authors have found to be significant in DFT calculations.[38]

The charge carriers in the conduction and valence bands are Dirac fermions and therefore possess a Berry phase φ_B , although due to the gapped dispersion it will be energy dependent, ranging from $\varphi_B = 0$ at the tip of the bands (at $|k| = 0$) and approaching $\varphi_B \simeq \pi$ at large energies.

It is worth noting here that we have not taken into account the explicit broken inversion symmetry from the different on site energies of the sublattices, as the band gap in the electronic spectrum of this Hamiltonian stems purely out of the hopping terms connecting orbitals localised around Sulfur atoms on differing layers.

This three band model shows all the qualitative features of the Hamiltonian suggested by Xiao *et al*[37] by symmetry arguments. We may show the agreement between the tight binding model presented here and the Hamiltonian suggested by symmetry by considering only the 2×2 block of Eq 5.4 in the space of $(u_{\mathbf{k}}^{(BS)}, u_{\mathbf{k}}^{(A2)})$ while neglecting the flat band, taking into account only the leading order terms and redefining zero energy to be exactly in the middle of the band gap. At this point it is convenient to introduce a spin orbit coupling term which is not captured in our tight binding analysis, as this has been shown to be important for describing the electronic structure of MoS₂. This arises in a honeycomb lattice with broken inversion symmetry and breaks the spin degeneracy along $\Gamma - K$ high symmetry line of the Brillouin zone and is of a significant size due to the Molybdenum atoms d-orbitals. Taking all of these features into account we may

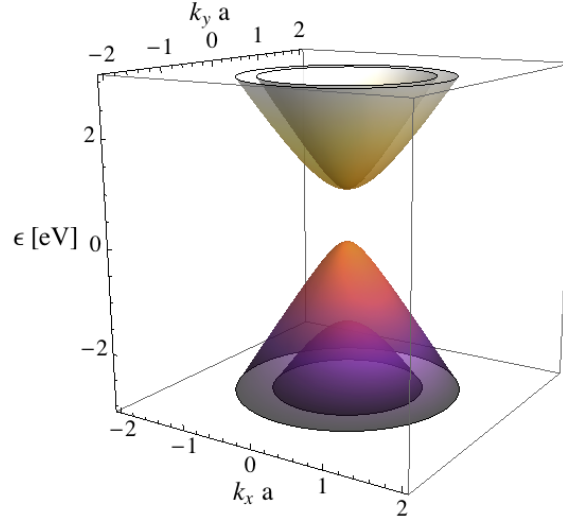


Figure 5.3: Showing the low energy electronic dispersion of MoS₂ given in Eq. 5.6 which is an effective theory for the bands labeled $\epsilon_{\mathbf{k}}^{(+)}$ and $\epsilon_{\mathbf{k}}^{(-)}$ while treating the effects of spin orbit coupling while neglecting the band labeled $\epsilon_{\mathbf{k}}$. This effective theory gives four bands due to the spin splitting and shows a large spin splitting in the valence band.

write an effective low energy Hamiltonian as

$$H^{(\tau)} = v\hbar(\tau_z\sigma_xk_x + \sigma_yk_y) - \frac{\Delta}{2}\sigma_z + \lambda\tau_zs_z\frac{(\mathbf{1} + \sigma_z)}{2} \quad (5.6)$$

where $\lambda = 80\text{meV}$ is the spin splitting caused by the spin orbit interaction and σ_i , τ_i and s_i the Pauli matrices in the sublattice, valley and spin space respectively. The electronic dispersion found from diagonalisation the matrix Hamiltonian is shown in Eq 5.6.b this highlights the large spin splitting in the valence band and the much smaller spin splitting in the conduction band which is spin degenerate at $k = 0$. Also note that in Eq 5.6 the spin orbit coupling term couples to the valley degree of freedom τ , this is a consequence of the broken inversion symmetry of the lattice and creates spin splitting in the valence bands which is equal and opposite for each spin in each valley.

This tight binding analysis allows us to capture the essential properties of the continuum of electronic states in perfect MoS₂. Experiments however revealed a rather low mobility of MoS₂ samples,[7, 8] which signals the importance of disorder and inhomogeneities in the understanding of the electronic properties of these atomically thin materials. In fact electronic transport, especially at low carrier concentrations, is dominated by localised states that can be successfully described by quantum-dot-like wavefunctions whose typical size and location is highly sample-

specific. We thus model a state localised at the bottom of the conduction band, in the regime $v\hbar|\mathbf{k}| \ll \Delta$, with the wavefunction

$$\psi_{\tilde{n},\tilde{m}}(x,y) = \langle x,y|\tilde{n},\tilde{m}\rangle = \frac{2}{\sqrt{L_{xd}L_{yd}}} \begin{pmatrix} 1 \\ 0 \end{pmatrix} \sin\left(\frac{\tilde{n}\pi(x-x_0)}{L_{xd}}\right) \sin\left(\frac{\tilde{m}\pi(y-y_0)}{L_{yd}}\right) \quad (5.7)$$

in the region $x \in [x_0, x_0 + L_{xd}]$ and $y \in [y_0, y_0 + L_{yd}]$ and zero elsewhere. This state covers the area $L_{xd}L_{yd}$ in the vicinity of the point (x_0, y_0) . In this wavefunction we assumed disorder potentials that vary smoothly on the scale of the lattice spacing a , which allows to decouple the valleys and to consider only one \mathbf{K} point.

5.2 Vibrational Properties of MoS₂

In order to study the vibrational properties of MoS₂ membranes we work within the framework of elasticity theory and describe any in plane deformation by a two dimensional vector field $\mathbf{u}^{(l)}(\mathbf{r})$, while out of plane deformations are described by a scalar field $h^{(l)}(\mathbf{r})$. A generic atom at position \mathbf{r} is thus shifted to $\mathbf{r} + \mathbf{u}^{(l)}(\mathbf{r}) + \hat{\mathbf{z}}h^{(l)}(\mathbf{r})$. In both cases l refers to the layer index, as distortions in each of the three layers of MoS₂ are considered.

We consider the elastic Lagrangian density

$$\mathcal{L} = \sum_{l=1}^3 \mathcal{L}^{(l)} + \mathcal{L}_{\text{coup}}^{(1-2)} + \mathcal{L}_{\text{coup}}^{(2-3)} \quad (5.8)$$

where, in analogy with the treatment of graphene, the Lagrangian density of layer l is

$$\mathcal{L}^{(l)} = \frac{1}{2}\rho \left(\dot{\mathbf{u}}^{(l)2} + \dot{h}^{(l)2} \right) - 2\mu u_{ij}^{(l)2} - \lambda u_{kk}^{(l)2} - \kappa \left(\nabla^2 h^{(l)} \right)^2 - \Gamma \left(\nabla h^{(l)} \right)^2. \quad (5.9)$$

Here $\rho = 3.1 \times 10^{-6} \text{kg m}^{-2}$ is the mass density, μ and λ are the Lamé coefficients which characterise the in-plane rigidity of the lattice, κ is the bending rigidity and Γ is a parameter describing the sample specific tension in the device due to clamping. We model the interlayer

coupling by harmonic confinement between adjacent layers, as described by the two terms

$$\mathcal{L}_{\text{coup}}^{(1-2)} = -\rho \frac{\Omega_{\text{in}}^{(1-2)2}}{2} (\mathbf{u}^{(1)} - \mathbf{u}^{(2)})^2 - \rho \frac{\Omega_{\text{out}}^{(1-2)2}}{2} (h^{(1)} - h^{(2)})^2 \quad (5.10)$$

$$\mathcal{L}_{\text{coup}}^{(2-3)} = -\rho \frac{\Omega_{\text{in}}^{(2-3)2}}{2} (\mathbf{u}^{(2)} - \mathbf{u}^{(3)})^2 - \rho \frac{\Omega_{\text{out}}^{(2-3)2}}{2} (h^{(2)} - h^{(3)})^2 \quad (5.11)$$

where $\Omega_{\text{in}}^{(1-2)}$ and $\Omega_{\text{in}}^{(2-3)}$ are the frequencies associated with in plane sliding between their respective layers and $\Omega_{\text{out}}^{(1-2)}$ and $\Omega_{\text{out}}^{(2-3)}$ are the corresponding ones for out of plane displacements. We assume $\Omega_{\text{in}}^{(1-2)} = \Omega_{\text{in}}^{(2-3)} = \Omega_{\text{in}}$ and $\Omega_{\text{out}}^{(1-2)} = \Omega_{\text{out}}^{(2-3)} = \Omega_{\text{out}}$.

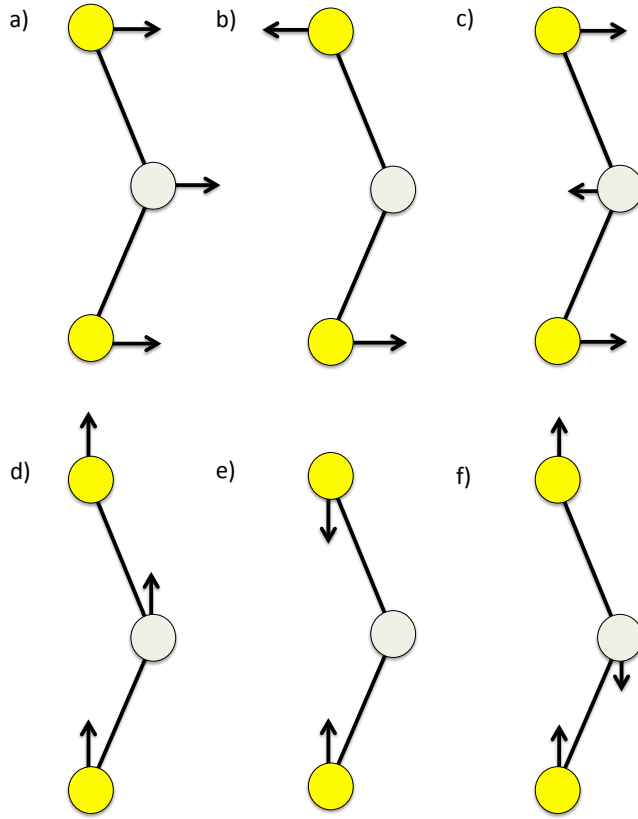


Figure 5.4: The six vibrational eigenmodes of MoS_2 . Panel a) In plane symmetric motion which we label $\mathbf{u}^{(s)}$. Panel b) the first of the in plane anti-symmetric modes labelled $\mathbf{u}^{(a1)}$, which represents shear motion of the two Sulfur layers. Panel c) the second of the in plane anti-symmetric modes labelled $\mathbf{u}^{(a2)}$, which represents the shear motion of the two Sulfur layers with respect to the Molybdenum layer. Panel d) Out of plane symmetric motion, labelled $h^{(s)}$. Panel e) the first of the out of plane anti-symmetric modes labelled $h^{(a1)}$, which represents the shear motion of the two Sulfur layers. Panel f) the second of the out of plane anti-symmetric modes labelled $h^{(a2)}$, which represents the shear motion of the two Sulfur layers with respect to the Molybdenum layer.

The three-layered structure of MoS_2 yields three in-plane normal modes, described by the

deformations

$$\mathbf{u}^{(s)}(\mathbf{r}) = \frac{1}{3} [\mathbf{u}^{(1)}(\mathbf{r}) + \mathbf{u}^{(2)}(\mathbf{r}) + \mathbf{u}^{(3)}(\mathbf{r})] \quad (5.12)$$

$$\mathbf{u}^{(a1)}(\mathbf{r}) = \frac{1}{2} [\mathbf{u}^{(3)}(\mathbf{r}) - \mathbf{u}^{(1)}(\mathbf{r})] \quad (5.13)$$

$$\mathbf{u}^{(a2)}(\mathbf{r}) = \frac{1}{3} [\mathbf{u}^{(1)}(\mathbf{r}) - 2\mathbf{u}^{(2)}(\mathbf{r}) + \mathbf{u}^{(3)}(\mathbf{r})], \quad (5.14)$$

and similarly three out of plane modes

$$h^{(s)}(\mathbf{r}) = \frac{1}{3} [h^{(1)}(\mathbf{r}) + h^{(2)}(\mathbf{r}) + h^{(3)}(\mathbf{r})] \quad (5.15)$$

$$h^{(a1)}(\mathbf{r}) = \frac{1}{2} [h^{(3)}(\mathbf{r}) - h^{(1)}(\mathbf{r})] \quad (5.16)$$

$$h^{(a2)}(\mathbf{r}) = \frac{1}{3} [h^{(1)}(\mathbf{r}) - 2h^{(2)}(\mathbf{r}) + h^{(3)}(\mathbf{r})]. \quad (5.17)$$

Both sets of normal modes are shown in Fig. 5.4. Studies of the Raman spectra of single layer MoS_2 have identified the $\mathbf{u}^{(a2)}$ and $h^{(a2)}$ shear channels as the E_{2g} Raman mode ($\sim 384\text{cm}^{-1}$) and the $h^{(a1)}$ breathing mode as the A_{1g} Raman mode ($\sim 400\text{cm}^{-1}$). [20, 25] The Euler-Lagrange equations are solved for the elastic Lagrangian density above in terms of the new deformations channels $\mathbf{u}^{(\nu)}(\mathbf{r}) = \sum_{\mathbf{q}} \mathbf{u}_{\mathbf{q}}^{(\nu)} \exp[i\mathbf{q} \cdot \mathbf{r}]$ and $h^{(\nu)}(\mathbf{r}) = \sum_{\mathbf{q}} h_{\mathbf{q}}^{(\nu)} \exp[i\mathbf{q} \cdot \mathbf{r}]$ where $\nu = s, a1, a2$ and $\mathbf{u}_{\mathbf{q}}^{(\nu)}$ and $h_{\mathbf{q}}^{(\nu)}$ are the Fourier components of the eigenmodes in the wavevector space. The eigenmodes can be decomposed into longitudinal and transverse channels as $u_{\mathbf{q}}^{(\nu,L)} = \mathbf{u}_{\mathbf{q}}^{(\nu)} \cdot \hat{\mathbf{q}}$ and $u_{\mathbf{q}}^{(\nu,T)} = \mathbf{u}_{\mathbf{q}}^{(\nu)} \cdot \hat{\mathbf{q}}_{\perp}$ where $\hat{\mathbf{q}} = \mathbf{q}/|\mathbf{q}|$ and $\hat{\mathbf{q}}_{\perp} = \hat{z} \times \hat{\mathbf{q}}$. This yields nine branches to the phonon dispersion of MoS_2 , three gapless symmetric branches (two in plane and one flexural) and six gapped antisymmetric branches (four in plane and two flexural). The phonon dispersions for the longitudinal, transverse and flexural (F) modes are

$$\omega_{\mathbf{q}}^{(\nu,L)} = \left[\frac{2\mu + \lambda}{\rho} q^2 + \Omega_{\text{in}} (\delta_{\nu,a1} + 3\delta_{\nu,a2}) \right]^{1/2} \quad (5.18)$$

$$\omega_{\mathbf{q}}^{(\nu,T)} = \left[\frac{2\mu q^2}{\rho} + \Omega_{\text{in}} (\delta_{\nu,a1} + 3\delta_{\nu,a2}) \right]^{1/2} \quad (5.19)$$

$$\omega_{\mathbf{q}}^{(\nu,F)} = \left[\frac{\kappa q^4 + \Gamma q^2}{\rho} + \Omega_{\text{out}} (\delta_{\nu,a1} + 3\delta_{\nu,a2}) \right]^{1/2} \quad (5.20)$$

Both symmetric in-plane dispersions are linear in wavevector and the flexural dispersion is quadratic in the absence of tension. Tension in the sample stiffens the flexural dispersion and leads to the appearance of a new wavevector scale $q_* = \sqrt{\Gamma/\kappa}$ below which the dispersion is linear.

Previous authors have studied the phononic dispersions in monolayer MoS_2 by ab-initio techniques[21, 22]. The work of Kaasbjerg *et al.* gives the values of the energy gap for the $u^{(a2)}$ as $\hbar\omega_{\mathbf{q}=0}^{(a2)} = 48$ meV and for $h^{(a1)}$ as $\hbar\omega_{\mathbf{q}=0}^{(a1)} = 50$ meV. These works allow us to fix the interlayer coupling frequencies in our analytical treatment which captures the essential physical properties of long-wavelength phonons in the membrane. In particular we correctly deduce that the a2 gapped mode is higher in energy than the a1.

5.3 Fictitious Gauge Fields In MoS_2

A generic deformation of the lattice leads to a displacement of the positions of the atomic sites, which translates into two kinds of corrections to the electronic Hamiltonian.

Firstly, the modifications of the bond lengths between neighbouring atoms causes the hopping energy scale to undergo the change $t_{sl,s'l'} \rightarrow t_{sl,s'l'} + \delta t_{sl,s'l'}$. This change in the hopping energies leads to new off diagonal terms in the electronic Hamiltonian which act to modify the electronic momenta like fictitious gauge fields. The corrections to the electronic Hamiltonian are of the form $\delta t_{sl,s'l'} = (\partial t_{sl,s'l'} / \partial l_{sl,s'l'}) \delta l_{sl,s'l'}$ where $\delta l_{sl,s'l'}$ denotes the variation of bond length. As the precise value of the derivatives $\partial t_{sl,s'l'} / \partial l_{sl,s'l'}$ in transition-metal dichalcogenides is not currently known in the literature, we assume $\partial t_{sl,s'l'} / \partial l_{sl,s'l'} \approx -\eta_{sl,s'l'} (t_{sl,s'l'} / l_{sl,s'l'})$ with the numerical prefactor $\eta_{sl,s'l'}$ of order 1 (we will assume this reference value in the following). Secondly, dilations in the local area of the lattice induce local changes in the electronic density with correspond to a diagonal scalar potential in the Hamiltonian matrix, called the deformation potential.

Translating the above changes in the tight-binding analysis, and reducing the problem to the 2×2 matrix form in the $(u_{\mathbf{k}}^{(BS)}, u_{\mathbf{k}}^{(A2)})$ electronic subspace, we deduce the deformation induced corrections to the electronic Hamiltonian in the two valleys ($\tau \pm 1$)

$$\delta H^{(\tau)} = \begin{pmatrix} \frac{1}{\sqrt{2}} \mathcal{F}_\gamma + \sqrt{2} D^{(s)} + \frac{1}{\sqrt{2}} D^{(a2)} & \mathcal{F}^{(\tau)\dagger} \\ \mathcal{F}^{(\tau)} & D^{(s)} - D^{(a2)} \end{pmatrix} \quad (5.21)$$

where we define

$$\begin{aligned}
\mathcal{F}^{(\tau)} = & \frac{3a}{\sqrt{2}\tilde{c}} \frac{\partial t}{\partial \tilde{c}} \left[\frac{3}{2} (u_y^{(a2)} - i\tau u_x^{(a2)}) + \frac{a}{4} (2u_{xx}^{(s)} - 2u_{yy}^{(s)} + i\tau 4u_{xy}^{(s)}) \right. \\
& + \frac{c}{2} (\partial_y h^{(a1)} - i\tau \partial_x h^{(a1)}) + \frac{3a}{16} ((\partial_x u_x^{(a1)})^2 + (\partial_y u_y^{(a1)})^2 + (\partial_y u_x^{(a1)})^2 + (\partial_x u_y^{(a1)})^2 \\
& - 2i\tau \partial_y u_x^{(a1)} \partial_x u_x^{(a1)} - 2i\tau \partial_y u_x^{(a1)} \partial_y u_y^{(a1)}) \\
& \left. + \frac{3a}{64} ((\partial_y h^{(a2)})^2 - (\partial_x h^{(a2)})^2 - i2\tau \partial_x h^{(a2)} \partial_y h^{(a2)}) \right] \quad (5.22)
\end{aligned}$$

with the strain tensor

$$u_{ij}^{(\nu)} = \frac{1}{2} (\partial_i u_j^{(\nu)} + \partial_j u_i^{(\nu)} + \partial_i h^{(\nu)} \partial_j h^{(\nu)}), \quad (5.23)$$

and

$$\mathcal{F}_\gamma = -\frac{\partial \gamma}{\partial c} \left[\frac{1}{c} \mathbf{u}^{(a1)2} + h^{(a1)} \right]. \quad (5.24)$$

The term $\mathcal{F}^{(\tau)}$ arises from changes in skewed bond lengths between Molybdenum atoms in the central layer ($l = 2$) and Sulfur atoms on the outer layers ($l = 1$ and $l = 3$) while the \mathcal{F}_γ is due to changes in the vertical bond length between Sulphur atoms on the bottom layer ($l = 1$) and the top layer ($l = 3$). In Eq. 5.22 we include only the terms lowest order in $\mathbf{u}(\mathbf{r})$ and $h(\mathbf{r})$ with the lowest derivative arising for each type of deformation (the full expression including all terms to second order is presented in appendix A). Due to the mirror symmetry with respect to the plane of the membrane, lattice deformations of the type $h^{(s)}(\mathbf{r})$, $h^{(a2)}(\mathbf{r})$ and $\mathbf{u}^{(a1)}(\mathbf{r})$ only couple at second order in the corrections to the skew hopping $\mathcal{F}^{(\tau)}$ in Eq. 5.22, although deformations of the type $\mathbf{u}^{(a1)}(\mathbf{r})$ do affect the vertical bond lengths and therefore arise in Eq 5.24 at first order.

The deformation potential terms take the form

$$D^{(\nu)} = g_2 \text{Tr}[u_{ij}^{(\nu)}] \quad (5.25)$$

where $\nu = s, a1, a2$, and with the coupling constant $g_2 = 2.8 \text{ eV}$. [22] Unlike the off diagonal gauge field coupling the deformation potential is affected by electronic screening, which acts to reduce g_2 from its unscreened value. [40]

The fictitious gauge fields that arise from strain can lead to a wealth of effects on the electronic transport properties of MoS₂ devices. One of the simplest strain configurations to consider is uniaxial strain, for example along the x -direction. This deformation corresponds to

$u^{(s)} = x(\delta L/L)\hat{x}$ leading to a constant $D^{(s)}$ which can be reabsorbed into a global shift of the zero point energy. The corresponding uniform gauge field leads to a shift in the position of the \mathbf{K} points in momentum space, which is equal and opposite in the two valleys.

Theoretical studies[24, 25, 26] predicted a crossover from a direct to an indirect bandgap in monolayer MoS₂ under the application of uniaxial strain and very recent experimental photoluminescence works have confirmed these predictions.[29, 30] This crossover occurs with increasing strain as the valence band maximum at the Γ point increases in energy, leading to an abrupt transition to the indirect band gap at a critical value of strain. However, as we focus on the effective theory near the \mathbf{K} points we will not address this transition.

The most dramatic effect of strain-induced gauge fields is the possibility to create fictitious magnetic fields in the sample. The form of the gauge fields allows this in MoS₂, in analogy with the case of graphene where a trigonal strain pattern leads to a uniform pseudomagnetic field as discussed in chapter 3.[32, 33] In contrast to monolayer graphene the anti-symmetric uniaxial deformations of the type $u^{(a2)} = x(\delta L/L)\hat{x}$ would also create a pseudomagnetic field, although the creation of a homogeneous strain of this kind could be difficult to implement in experiments.

5.4 Electron-Vibron Coupling Constants

In this section we will turn our attention to the interactions between electrons and vibrons in MoS₂ and calculate the value of the dimensionless electron-vibron coupling constants. Recent experimental studies have shown that at low carrier densities localised impurity states dominate the electronic transport in MoS₂ transistors, leading to variable range hopping at high temperatures and to resonant tunnelling between these localised states at low temperatures ($T < 30K$).[10] At these low temperatures we enter the Coulomb blockade regime. Here we introduce the important physics of this transport regime and the role the vibrational properties of the MoS₂ membrane can play.

When transport is mediated by a strongly localised electronic state the role of interactions becomes important. The single particle electronic spectrum of a localised quantum dot-like state will comprise of discrete spin degenerate levels due to size quantisation effects. Once we consider multiple electrons residing within the localised state the strong Coulomb interactions arising from the close proximity of the particles will modify this spectrum lifting the degeneracy. This creates

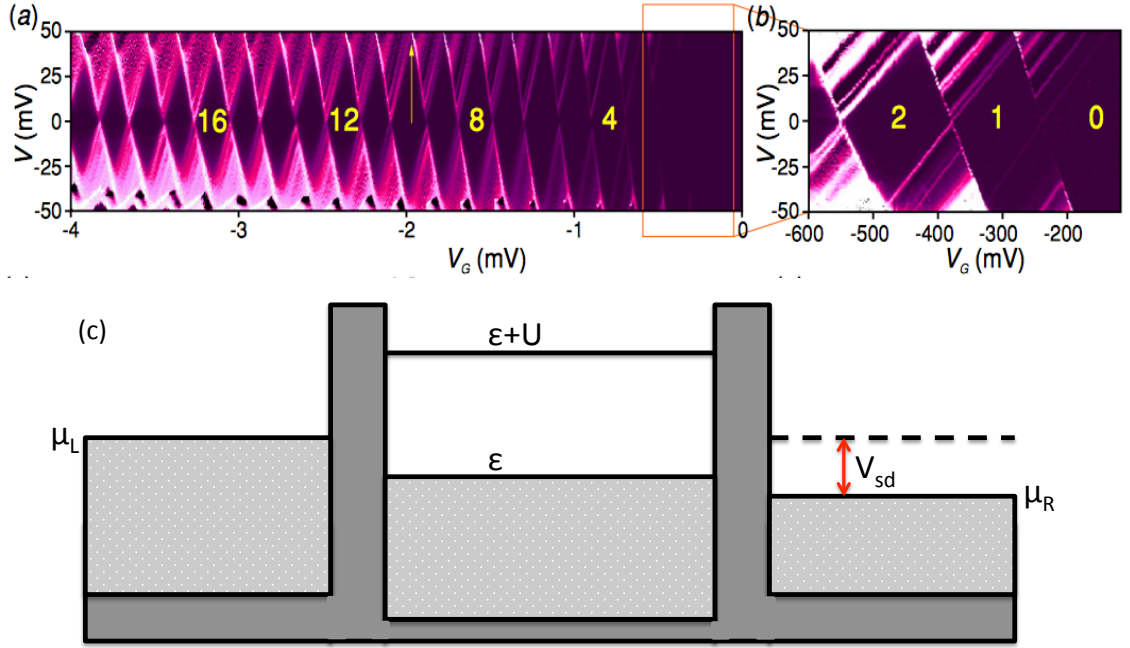


Figure 5.5: Panel a) shows a plot differential conductance dI/dV of source-drain bias V vs back-gate voltage V_G which clearly shows Coulomb diamonds in a carbon nanotube quantum dot. Measurements are taken at $T = 4K$, and taken over negative V_G . In the black diamond-shaped regions, the number of holes is fixed by the Coulomb blockade. Panel b) shows a zoom taken at $0.3K$ on the diamonds corresponding to 0,1,2 holes within the quantum dot, the white lines running parallel to the edge of the diamond correspond to discrete excited states. Panel c) shows a sketch of the setup of the quantum dot, with the light grey regions indicating the filled electron states in both the right and left leads and in the quantum dot itself. Notice the higher energy state in the dot at $\epsilon + U$ due to the Coulomb interaction. The dark grey regions indicate the potential barriers that separate the quantum dot from the leads. Adapted from Sapmaz et al, Semiconductor Science and Technology 11, 21 (2006) [41]

an energy cost for the dot to be more than individually occupied. For example in a localised state which at the single particle level forms a single spin degenerate energy level at energy ϵ , the first electron in the state will be at the energy ϵ whereas the second electron will sit at a higher energy $\epsilon + U$ lifting the spin degeneracy, where U is due to the Coulomb interaction and is known as the charging energy. To analyse electronic transport through this state we can imagine connecting the state to two reservoirs of electrons, one playing the role of the left lead (source) and one the right lead (drain), an example of this setup is shown in Fig. 5.5.c. An electron may tunnel from one of these reservoirs into the localised state where it may remain for a time. For a second electron to tunnel into the localised state while it is occupied it must pay an energy cost U , leading to a suppression in the conductance through the dot at low source-drain bias. This effect is known as Coulomb blockade. This suppression may be overcome if the source-drain bias V_{sd}

is larger than U/e . Controlling the source-drain bias V_{sd} and the back gate voltage V_{bg} locally applied to the localised state allows for the conductance to be mapped out over a wide range of potential differences. In the Coulomb blockade this mapping creates striking diamond patterns in a plot of back gate voltage V_{bg} vs source-drain bias V_{sd} an example of which is shown in Fig 5.5.a and Fig 5.5.b in differential conductance dI_{sd}/dV_{sd} . Additionally, to experimentally observe the Coulomb blockade regime the temperature must be low enough for thermal excitation to be neglected $k_bT \ll U$.

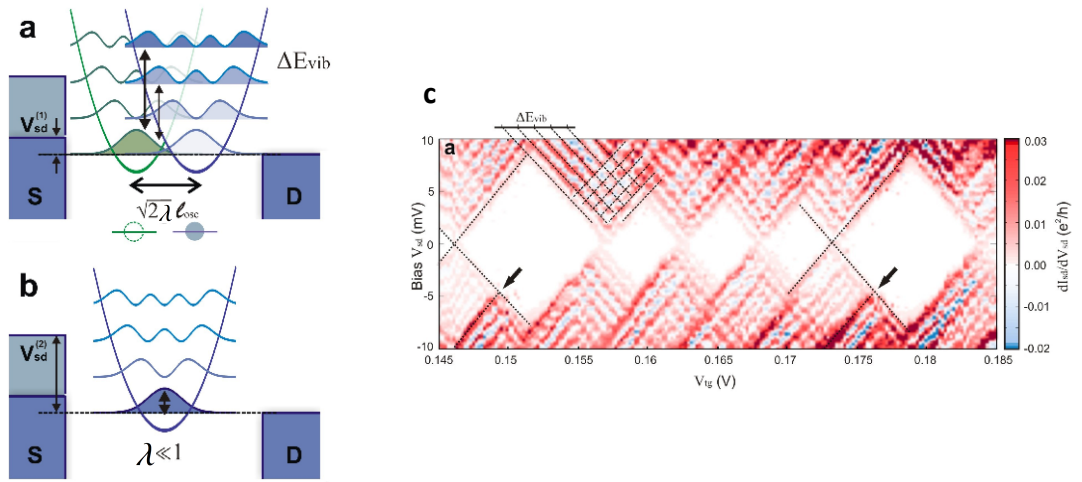


Figure 5.6: Panel a) shows a diagram of vibronic oscillator states, showing the shift of equilibrium coordinate of the vibronic wave function occurring in a tunnelling process due to electron-vibron coupling. This also shows how low energy states are affected to a greater degree than higher energy states due to size of the wave function. Panel b) shows the same picture but for small electron-vibron coupling, this small coupling gives a small shift in the equilibrium coordinate of the vibronic wave function leading to a greater overlap of the vibronic wave function. Panel c) shows the differential conductance dI_{sd}/dV_{sd} of a suspended carbon nanotube quantum dot. We see periodic features in the conductance which are attributed to vibrational sidebands from excited vibronic states (shown in dashed lines) and also the suppression of the low bias conductance due to the Franck-Condon blockade. Adapted from Leturcq et al, Nature Physics 5, 327 - 331 (2009).

So far in this discussion we have not considered vibrational effects, which plays two main roles. Firstly an electron tunnelling into the localised state may excite or absorb a quantised vibrational mode, called a vibron. This mechanism introduces new pathways for electrons into the localised state, and will lead to new peaks in the conductance at intervals of the energy of the vibronic modes which run parallel to the edges of Coulomb diamonds observed in the V_{bg} , V_{sd} diagrams. This effect can be seen in Fig 5.6.c in the periodic pattern in the conducting regions. Secondly, the strong coupling of electrons with vibrons can induce a suppression of the conduc-

tance at low bias, an effect known as Franck-Condon blockade, which can be understood as follows. The probability of the electronic tunnelling process into the localised state is proportional to the square of the overlap between the vibronic wave functions before and after tunnelling. When tunnelling into the localised state, the electron shifts the equilibrium coordinate of the vibron oscillator by an amount proportional to the electron-vibron coupling λ . This shift is demonstrated in Fig 5.6.a. For low lying states the overlap of vibronic wave functions due to the equilibrium displacement leads to an exponential suppression of the tunnelling probability. In contrast, higher energy states are less sensitive as their wave functions are spread out. This effect creates a low bias suppression of conductance in systems with strong electron-vibron coupling leading large shifts in the equilibrium coordinate of the vibron oscillator.

In order to analyse the transport regime described above, and to assess the influence of deformations on transport in MoS₂, we employ the Anderson-Holstein model describing the coupling between localised (quantum dot-like) electronic states and quantised vibrational modes, called vibrons. We shall focus on vibron modes which couple linearly with electrons, as these modes will give the strongest couplings and are the relevant one to induce the Franck-Condon blockade regime. The corresponding Hamiltonian is

$$H = H_D + H_{\text{vib}} + H_{\text{lead}} + H_T \quad (5.26)$$

where

$$\begin{aligned} H_D &= \sum_{\sigma=\uparrow,\downarrow} \sum_{\nu,\mathbf{q}} \left[\epsilon_D + \lambda_{\mathbf{q}}^{(\nu)} \hbar \omega_{\mathbf{q}}^{(\nu)} (b_{\mathbf{q}}^{(\nu)\dagger} + b_{\mathbf{q}}^{(\nu)}) \right] n_{\sigma} + U n_{\uparrow} n_{\downarrow} \\ H_{\text{vib}} &= \sum_{\nu,\mathbf{q}} \hbar \omega_{\mathbf{q}}^{(\nu)} b_{\mathbf{q}}^{(\nu)\dagger} b_{\mathbf{q}}^{(\nu)} \\ H_{\text{lead}} &= \sum_{\alpha=L,R} \sum_{\mathbf{k},\sigma} \epsilon_{\mathbf{k},\sigma} c_{\alpha,\mathbf{k},\sigma}^{\dagger} c_{\alpha,\mathbf{k},\sigma} \\ H_T &= \sum_{\alpha=L,R} \sum_{\mathbf{k},\sigma} t_{\alpha,\mathbf{k}} c_{\alpha,\mathbf{k},\sigma}^{\dagger} d_{\sigma} + h.c. \end{aligned} \quad (5.27)$$

Here H_D and H_{vib} represent the purely electronic and vibronic Hamiltonians, including the electron-vibron interaction, whereas H_{lead} and H_T describe the electronic degrees of freedom in the right/left (R/L) leads (with $c_{\alpha,\mathbf{k},\sigma}$ the related annihilator of electrons with wavevector \mathbf{k} and spin σ in the lead α) and the tunnelling between the leads and the localised state, respectively. In Eq. (5.27) $n_{\sigma} = d_{\sigma}^{\dagger} d_{\sigma}$ is the electron number operator for the localised state (with d_{σ} the annihilation opera-

tor for an electron with spin σ) and $b_{\mathbf{q}}^{(\nu)}$ is the bosonic annihilator for a vibron of type $\nu = s, a1, a2$ with wavevector \mathbf{q} .

To compute the dimensionless electron-vibron coupling constant $\lambda_{\mathbf{q}}$, we introduce the vibronic displacement operator $\zeta_{\mathbf{q}} = (b_{\mathbf{q}}^{(\nu)\dagger} + b_{\mathbf{q}}^{(\nu)})l_{\text{osc},q}^{(\nu)}/\sqrt{2}$ with $l_{\text{osc},q}^{(\nu)} = \sqrt{\hbar/M\omega_{\mathbf{q}}^{(\nu)}}$ and where $M = \rho L_x L_y$ is the oscillator mass.. This allows the dot Hamiltonian to be rewritten as

$$H_D = \sum_{\sigma=\uparrow,\downarrow} \sum_{\nu,\mathbf{q}} \left[\epsilon_D + \lambda_{\mathbf{q}}^{(\nu)} \hbar \omega_{\mathbf{q}}^{(\nu)} \frac{\sqrt{2}\zeta_{\mathbf{q}}}{l_{\text{osc},q}^{(\nu)}} \right] n_{\sigma} + U n_{\uparrow} n_{\downarrow}. \quad (5.28)$$

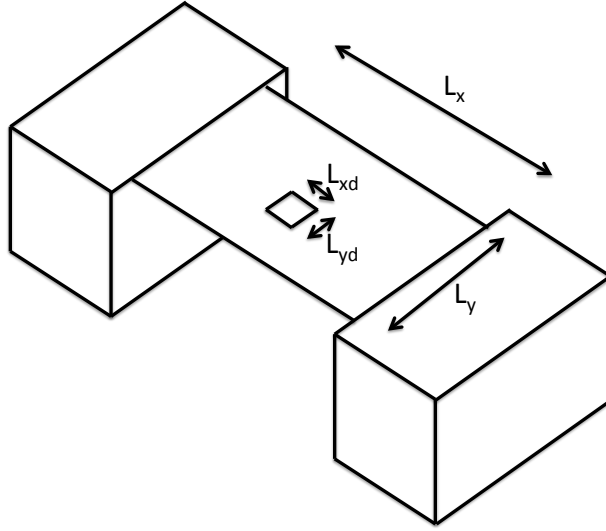


Figure 5.7: The setup and geometry of a suspended MoS₂ device. The central region shows a suspended sample of width L_y and length L_x which contains a localised state confined within a box with with a with of L_{yd} and a length L_{xd} .

We define the electron-vibron coupling constant $\lambda_{\mathbf{q}}^{(\nu)}$ as the energy shift of a localized electronic state induced by a static vibron displacement $\zeta_{\mathbf{q}} = l_{\text{osc},q}^{(\nu)}/\sqrt{2}$ in units of $\hbar\omega_{\mathbf{q}}^{(\nu)}$. The shift can be calculated within first order perturbation theory as $\Delta\epsilon(\zeta) = \langle \tilde{n}, \tilde{m} | V_{\text{el-ph}} | \tilde{n}, \tilde{m} \rangle$ where the state $|\tilde{n}, \tilde{m}\rangle$ is defined in Eq 5.7 and the matrix equation in Eq 5.21 is used for $V_{\text{el-ph}}$. Therefore the electron-vibron coupling constant is

$$\lambda_{\mathbf{q}}^{(\nu)} = \frac{\Delta\epsilon^{(\nu)}(\zeta_{\mathbf{q}} = l_{\text{osc},q}^{(\nu)}/\sqrt{2})}{\hbar\omega_{\mathbf{q}}^{(\nu)}}. \quad (5.29)$$

To calculate $\lambda_{\mathbf{q}}^{(\nu)}$ for the different vibron channels ν we use Eq 5.21 for $V_{\text{el-ph}}$ taking only terms of the vibron type ν under consideration and consider a suspended MoS₂ device with a length L_x and

width L_y , clamped at $x = 0$ and $x = L_x$, shown in Fig 5.7. Due to the symmetry of the problem, we approximate the deformations of the membrane to vanish in the y -direction and we consider vibrons with a quantised wavevector $q_n = n\pi/L_x$ along the x -direction, this approximation assumes MoS₂ has a negligible Poisson ratio and is therefore most valid for short wide samples. Within the sample, the localised state occupies the region defined by $x \in [x_0; x_0+L_{xd}]$ and $y \in [y_0; y_0+L_{yd}]$.

The Stretching mode $u^{(s)}$ - The longitudinal stretching of the suspended MoS₂ includes both variations of area and modulations in the bond lengths. The associated stretching distortion is given by $u_x^{(s)} = \zeta_{\mathbf{q}} \sin(\frac{n\pi x}{L_x})$ and $u_y^{(s)} = 0$, yielding the electron-phonon coupling matrix

$$V_{\text{el-ph}} = \begin{pmatrix} \sqrt{2}g_2\partial_x u_x^{(s)} & g_1\partial_x u_x^{(s)} \\ g_1\partial_x u_x^{(s)} & \sqrt{2}g_2\partial_x u_x^{(s)} \end{pmatrix}. \quad (5.30)$$

This coupling includes all linear contributions from both the gauge field and the deformation potential, with $g_1 = 3a^2/2 \sqrt{2}\tilde{c}(\partial t/\partial \tilde{c}) \approx 0.7$ eV and $g_2 = 2.8$ eV. The resulting electronic energy shift is

$$\Delta\epsilon(\zeta_{\mathbf{q}}) = \frac{4\zeta_{\mathbf{q}}n\pi}{\sqrt{2}L_xL_{xd}}g_2\mathcal{I}_{n,\tilde{n}}^{(1)} \quad (5.31)$$

where $\mathcal{I}_{n,\tilde{n}}^{(1)}$ is given by

$$\mathcal{I}_{n,\tilde{n}}^{(1)} = \int_{x_0}^{x_0+L_{xd}} dx \cos\left(\frac{n\pi x}{L_x}\right) \sin^2\left(\frac{\tilde{n}\pi(x-x_0)}{L_{xd}}\right). \quad (5.32)$$

From this expression it is evident that the rigid shift corresponding to the $n = 0$ mode yields a vanishing energy correction, as this would involve no strain in the device. As a consequence we consider only the $n \geq 1$ modes. This coupling is due to the deformation potential, strongly depends on the particular location of the localised states in the electronic dispersion. To evaluate this integral it is useful to consider the two opposite regimes of the clean and the dirty devices. In the clean regime the dot size is the same as the sample, and it would be realistic for a suspended high-mobility MoS₂ device at large carrier density. In this regime we set $x_0 = 0$ and $L_{xd} = L_x$, yielding $\mathcal{I}_{n,\tilde{n}}^{(1)} = -L_x\delta_{n,2\tilde{n}}/4$. As a consequence, this regime gives rise to strong selection rules for the electron-vibron coupling.

In the dirty regime we assume $L_{xd} \ll L_x$ and $L_{yd} \ll L_y$ in this regime we find the integral

to be

$$\mathcal{I}_{n,\tilde{n}}^{(1)} = \frac{L_{xd}}{2} \cos\left(\frac{n\pi x_0}{L_x}\right). \quad (5.33)$$

This shows a sample specific electron-vibron coupling which strongly depends on the position of the localized state, as the sharply localised electronic wave function samples the local strain in the device. If we consider the dot position which gives maximum coupling and use $\omega_{\mathbf{q}}^{(s)} = \nu q$ with $\nu = 6.7 \times 10^3 \text{ ms}^{-1}$, [22] we obtain

$$\lambda_n^{(s),max} = \frac{0.026}{\sqrt{n L_y [\mu m]}}. \quad (5.34)$$

As a result, the coupling constant $\lambda^{(s)}$ will be usually small for large samples, and it could only reach values of the order of unity for sample widths of order of nanometers. The smaller size of the coupling constant as compared to the case of quantum dots in suspended carbon nanotubes is partially due to the larger mass of MoS₂ devices which leads to a suppression of the oscillator length. This tendency is only partly compensated by the larger density of states of vibron modes in MoS₂ as compared to carbon nanotubes. Indeed, if we directly compare the size of the electron-vibron coupling to the longitudinal stretching in both carbon nanotube from Mariani et al[34] and our result for MoS₂ we find $\lambda_{\text{MoS}_2}^{(s)}/\lambda_{\text{CNT}}^{(s)} = 0.27$, from this we may conclude that while the coupling is larger in carbon nanotubes they are comparable and the width of the device plays the largest role in determining the maximum values of $\lambda_n^{(s),max}$ that can be experimentally realised.

The Shear mode $u^{(a2)}$ - the longitudinal shear motion of the Sulfur and Molybdenum layers moving in antiphase involves both modulations of the bond lengths and variations of area. The shear mode deformation is given by $u_x^{(a2)} = \zeta_{\mathbf{q}} \sin(\frac{n\pi x}{L_x})$ and $u_y^{(a2)} = 0$, yielding the electron-phonon coupling matrix

$$V_{\text{el-ph}} = \begin{pmatrix} \frac{1}{\sqrt{2}} g_2 \partial_x u_x^{(a2)} & -\frac{3g_1}{a} i\tau u_x^{(a2)} \\ \frac{3g_1}{a} i\tau u_x^{(a2)} & \frac{1}{\sqrt{2}} g_2 \partial_x u_x^{(a2)} \end{pmatrix} \quad (5.35)$$

where we have used the same definitions of g_1 and g_2 as in the previous section. The corresponding electronic energy shift is

$$\Delta\epsilon(\zeta_{\mathbf{q}}) = \frac{\sqrt{2}\zeta_{\mathbf{q}}n\pi}{L_x L_{xd}} g_2 \mathcal{I}_{n,\tilde{n}}^{(1)}. \quad (5.36)$$

This expression is very similar to that created by the longitudinal stretching mode, with the major exception being that the shear mode is gapped. As a consequence, the high energy cost to ex-

cite shear vibron modes at long wavelengths leads to a dramatic reduction in the electron-vibron coupling constant, which reaches the maximum value

$$\lambda_n^{(a2),max} = \frac{6.2 \times 10^{-8}}{\sqrt{n} L_y[\mu m]}. \quad (5.37)$$

The very small electron vibron coupling implies that shear modes will not result into major vibronic effects in transport measurements through localised states in MoS₂.

The Breathing mode $h^{(a1)}$ - The final vibron that leads to a linear coupling with electrons is the antisymmetric out-of-plane mode $h^{(a1)}$, i.e. the out of plane breathing mode. In this case we have to consider the effect of modulations of the bond lengths whereas the variations of area enter the electron-phonon coupling matrix only at second order and are thus not considered. The electron phonon coupling matrix for this mode is

$$V_{\text{el-ph}} = \begin{pmatrix} -\frac{1}{\sqrt{2}}g_\gamma h^{(a1)} & -g_1 i\tau \frac{c}{a} \partial_x h^{(a1)} \\ g_1 i\tau \frac{c}{a} \partial_x h^{(a1)} & 0 \end{pmatrix} \quad (5.38)$$

where $g_\gamma = (\partial\gamma/\partial c) \approx 1.1 \text{ eV}\text{\AA}^{-1}$. Depending on the details of the boundary conditions, in this case one could also consider the $n = 0$ mode, corresponding to a uniform out-of-plane distortion. Evaluating the energy shift associated with the corresponding deformation $h^{(a1)} = \zeta_{\mathbf{q}}$ we find $\Delta\epsilon = -g_\gamma \zeta_{\mathbf{q}} / \sqrt{2}$, which yields the electron-vibron coupling constant

$$\lambda_{n=0}^{(a1),max} = \frac{8 \times 10^{-5}}{\sqrt{L_x[\mu m] L_y[\mu m]}}. \quad (5.39)$$

The smallness of this coupling is primarily due to the gapped nature of the vibron breathing modes, and implies very small vibronic effects in realistic MoS₂ devices. The $n \geq 1$ breathing modes, associated with distortions of the form $h^{(a1)} = \zeta_{\mathbf{q}} \sin(n\pi x/L_x)$ yield a sample dependent electron-vibron constant which is even lower than for the $n = 0$ mode, due to the slight increase in the energy of the vibron modes at finite wavevectors.

5.5 Conclusion

In this chapter, we have presented a model of the electronic band structure of MoS₂ and then derived the form of the fictitious gauge fields which arise for any arbitrary deformation of the

MoS₂ lattice. These fictitious gauge fields form the starting point for discussing the large variety of effects that deformations of the lattice can cause on the electronic properties of MoS₂. As a first use of this formalism we studied the strength of the electron-vibron coupling to understand vibrational effects on electronic transport through localised impurity states.

Our results show small dimensionless electron-vibron coupling constants which are highly sample specific. The strongest coupling arises from longitudinal stretching modes, but this coupling is still weak for any realistic width of the device. These results are consistent with the lack of observations of vibrational sidebands in current MoS₂ devices. High quality devices in which the quantum dot extends across the entire device will greatly enhance the electron-vibron effects, as within this clean limit the strong selection rules will lead to vibrational sidebands being visible within the Coulomb diamonds measured in a device. Unfortunately currently available MoS₂ samples still show rather high levels of disorder.

One fruitful way to increase the electron-vibron coupling constant will be to consider devices close to the mechanical buckling instability, which will lead to a softening of the vibron modes,[42, 43] but this is outside the scope of the current work.

Monolayer transition-metal dichalcogenides provide a new avenue for electronic devices exploiting mechanical degrees of freedom which offers many differences from graphene, most notably a gapped electronic spectrum. This work provides the full form of the fictitious gauge fields which can inform future work in this area.

Bibliography

- [1] K. S. Novoselov, A. K. Geim, S. V. Morozov, D. Jiang, Y. Zhang, S. V. Dubonos, I. V. Grigorieva, and A. A. Firsov, “Electric field effect in atomically thin carbon films,” *Science*, vol. 306, no. 5696, pp. 666–669, 2004.
- [2] K. S. Novoselov, A. K. Geim, S. V. Morozov, D. Jiang, M. I. Katsnelson, I. V. Grigorieva, S. V. Dubonos, and A. A. Firsov, “Two-dimensional gas of massless dirac fermions in graphene,” *Nature*, vol. 438, pp. 197–200, 11 2005.
- [3] A. Splendiani, L. Sun, Y. Zhang, T. Li, J. Kim, C.-Y. Chim, G. Galli, and F. Wang, “Emerging photoluminescence in monolayer mos₂,” *Nano Letters*, vol. 10, pp. 1271–1275, 2014/01/24 2010.
- [4] K. F. Mak, C. Lee, J. Hone, J. Shan, and T. F. Heinz, “Atomically thin mos₂: A new direct-gap semiconductor,” *Physical Review Letters*, vol. 105, pp. 136805–, 09 2010.
- [5] H. Zeng, J. Dai, W. Yao, D. Xiao, and X. Cui, “Valley polarization in mos₂ monolayers by optical pumping,” *Nat Nano*, vol. 7, pp. 490–493, 08 2012.
- [6] K. F. Mak, K. He, J. Shan, and T. F. Heinz, “Control of valley polarization in monolayer mos₂ by optical helicity,” *Nat Nano*, vol. 7, pp. 494–498, 08 2012.
- [7] A. Ayari, E. Cobas, O. Ogundadegbe, and M. S. Fuhrer, “Realization and electrical characterization of ultrathin crystals of layered transition-metal dichalcogenides,” *Journal of Applied Physics*, vol. 101, no. 1, pp. –, 2007.
- [8] H. Wang, L. Yu, Y.-H. Lee, Y. Shi, A. Hsu, M. L. Chin, L.-J. Li, M. Dubey, J. Kong, and T. Palacios, “Integrated circuits based on bilayer mos₂ transistors,” *Nano Letters*, vol. 12, pp. 4674–4680, 2014/01/24 2012.

- [9] Radisavljevic B., Radenovic A., Brivio J., Giacometti V., and Kis A., “Single-layer mos₂ transistors,” *Nat Nano*, vol. 6, pp. 147–150, 03 2011.
- [10] S. Ghatak, A. N. Pal, and A. Ghosh, “Nature of electronic states in atomically thin mos₂ field-effect transistors,” *ACS Nano*, vol. 5, pp. 7707–7712, 2014/01/24 2011.
- [11] B. J. LeRoy, S. G. Lemay, J. Kong, and C. Dekker, “Electrical generation and absorption of phonons in carbon nanotubes,” *Nature*, vol. 432, pp. 371–374, 11 2004.
- [12] S. Sapmaz, P. Jarillo-Herrero, Y. M. Blanter, C. Dekker, and H. S. J. van der Zant, “Tunneling in suspended carbon nanotubes assisted by longitudinal phonons,” *Physical Review Letters*, vol. 96, pp. 026801–, 01 2006.
- [13] A. K. Hüttel, M. Poot, B. Witkamp, and H. S. J. van der Zant, “Nanoelectromechanics of suspended carbon nanotubes,” *New Journal of Physics*, vol. 10, no. 9, p. 095003, 2008.
- [14] F. Kuemmeth, S. Ilani, D. C. Ralph, and P. L. McEuen, “Coupling of spin and orbital motion of electrons in carbon nanotubes,” *Nature*, vol. 452, pp. 448–452, 03 2008.
- [15] A. K. Hüttel, B. Witkamp, M. Leijnse, M. R. Wegewijs, and H. S. J. van der Zant, “Pumping of vibrational excitations in the coulomb-blockade regime in a suspended carbon nanotube,” *Physical Review Letters*, vol. 102, pp. 225501–, 06 2009.
- [16] J. Koch, F. von Oppen, and A. V. Andreev, “Theory of the franck-condon blockade regime,” *Physical Review B*, vol. 74, pp. 205438–, 11 2006.
- [17] R. Leturcq, C. Stampfer, K. Inderbitzin, L. Durrer, C. Hierold, E. Mariani, M. G. Schultz, F. von Oppen, and K. Ensslin, “Franck-condon blockade in suspended carbon nanotube quantum dots,” *Nat Phys*, vol. 5, pp. 327–331, 05 2009.
- [18] S. Bertolazzi, J. Brivio, and A. Kis, “Stretching and breaking of ultrathin mos₂,” *ACS Nano*, vol. 5, pp. 9703–9709, 2014/01/24 2011.
- [19] A. Castellanos-Gomez, M. Poot, G. A. Steele, H. S. J. van der Zant, N. Agrait, and G. Rubio-Bollinger, “Elastic properties of freely suspended mos₂ nanosheets,” *Advanced Materials*, vol. 24, no. 6, pp. 772–775, 2012.

- [20] C. Lee, H. Yan, L. E. Brus, T. F. Heinz, J. Hone, and S. Ryu, "Anomalous lattice vibrations of single- and few-layer mos₂," *ACS Nano*, vol. 4, pp. 2695–2700, 2014/01/24 2010.
- [21] A. Molina-Sánchez and L. Wirtz, "Phonons in single-layer and few-layer mos₂ and ws₂," *Physical Review B*, vol. 84, pp. 155413–, 10 2011.
- [22] K. Kaasbjerg, K. S. Thygesen, and K. W. Jacobsen, "Phonon-limited mobility in mos₂ from first principles," *Physical Review B*, vol. 85, pp. 115317–, 03 2012.
- [23] A. Castellanos-Gomez, R. van Leeuwen, M. Buscema, H. S. J. van der Zant, G. A. Steele, and W. J. Venstra, "Mechanical resonators: Single-layer mos₂ mechanical resonators (adv. mater. 46/2013)," *Advanced Materials*, vol. 25, no. 46, pp. 6636–6636, 2013.
- [24] H. Pan and Y.-W. Zhang, "Tuning the electronic and magnetic properties of mos₂ nanoribbons by strain engineering," *The Journal of Physical Chemistry C*, vol. 116, pp. 11752–11757, 2014/01/24 2012.
- [25] P. Lu, X. Wu, W. Guo, and X. C. Zeng, "Strain-dependent electronic and magnetic properties of mos₂ monolayer, bilayer, nanoribbons and nanotubes," *Physical Chemistry Chemical Physics*, vol. 14, no. 37, pp. 13035–13040, 2012.
- [26] Q. Yue, J. Kang, Z. Shao, X. Zhang, S. Chang, G. Wang, S. Qin, and J. Li, "Mechanical and electronic properties of monolayer mos₂ under elastic strain," *Physics Letters A*, vol. 376, pp. 1166–1170, 2 2012.
- [27] H. Peelaers and C. G. Van de Walle, "Effects of strain on band structure and effective masses in mos₂," *Physical Review B*, vol. 86, pp. 241401–, 12 2012.
- [28] M. Ghorbani-Asl, S. Borini, A. Kuc, and T. Heine, "Strain-dependent modulation of conductivity in single-layer transition-metal dichalcogenides," *Physical Review B*, vol. 87, pp. 235434–, 06 2013.
- [29] K. He, C. Poole, K. F. Mak, and J. Shan, "Experimental demonstration of continuous electronic structure tuning via strain in atomically thin mos₂," *Nano Letters*, vol. 13, pp. 2931–2936, 2014/01/24 2013.

- [30] H. J. Conley, B. Wang, J. I. Ziegler, R. F. Haglund, S. T. Pantelides, and K. I. Bolotin, “Bandgap engineering of strained monolayer and bilayer mos₂,” *Nano Letters*, vol. 13, pp. 3626–3630, 2014/01/24 2013.
- [31] E. Mariani and F. von Oppen, “Flexural phonons in free-standing graphene,” *Physical Review Letters*, vol. 100, pp. 076801–, 02 2008.
- [32] F. Guinea, M. I. Katsnelson, and A. K. Geim, “Energy gaps and a zero-field quantum hall effect in graphene by strain engineering,” *Nat Phys*, vol. 6, pp. 30–33, 01 2010.
- [33] N. Levy, S. A. Burke, K. L. Meaker, M. Panlasigui, A. Zettl, F. Guinea, A. H. C. Neto, and M. F. Crommie, “Strain-induced pseudo-magnetic fields greater than 300 tesla in graphene nanobubbles,” *Science*, vol. 329, no. 5991, pp. 544–547, 2010.
- [34] E. Mariani and F. von Oppen, “Electron-vibron coupling in suspended carbon nanotube quantum dots,” *Physical Review B*, vol. 80, pp. 155411–, 10 2009.
- [35] Z. Y. Zhu, Y. C. Cheng, and U. Schwingenschlögl, “Giant spin-orbit-induced spin splitting in two-dimensional transition-metal dichalcogenide semiconductors,” *Physical Review B*, vol. 84, pp. 153402–, 10 2011.
- [36] S. Lebègue and O. Eriksson, “Electronic structure of two-dimensional crystals from ab-initio theory,” *Physical Review B*, vol. 79, pp. 115409–, 03 2009.
- [37] D. Xiao, G.-B. Liu, W. Feng, X. Xu, and W. Yao, “Coupled spin and valley physics in monolayers of formula mos₂ and other group-vi dichalcogenides,” *Physical Review Letters*, vol. 108, pp. 196802–, 05 2012.
- [38] A. Kormányos, V. Zólyomi, N. D. Drummond, P. Rakyta, G. Burkard, and V. I. Fal’ko, “Monolayer mos₂: Trigonal warping, the valley, and spin-orbit coupling effects,” *Physical Review B*, vol. 88, pp. 045416–, 07 2013.
- [39] E. Cappelluti, R. Roldán, J. A. Silva-Guillén, P. Ordejón, and F. Guinea, “Tight-binding model and direct-gap/indirect-gap transition in single-layer and multilayer mos₂,” *Physical Review B*, vol. 88, pp. 075409–, 08 2013.
- [40] H. Suzuura and T. Ando, “Phonons and electron-phonon scattering in carbon nanotubes,” *Physical Review B*, vol. 65, pp. 235412–, 05 2002.

-
- [41] S. Sapmaz, P. Jarillo-Herrero, L. P. Kouwenhoven, and H. S. J. van der Zant, “Quantum dots in carbon nanotubes,” *Semiconductor Science and Technology*, vol. 21, no. 11, p. S52, 2006.
- [42] G. Weick, F. Pistolesi, E. Mariani, and F. von Oppen, “Discontinuous euler instability in nanoelectromechanical systems,” *Physical Review B*, vol. 81, pp. 121409–, 03 2010.
- [43] G. Weick, F. von Oppen, and F. Pistolesi, “Euler buckling instability and enhanced current blockade in suspended single-electron transistors,” *Physical Review B*, vol. 83, pp. 035420–, 01 2011.

6

Conclusions

In this thesis we have provided a formalism to describe the electromechanical properties of both monolayer and bilayer graphene as well as transition metal dichalcogenides. Within this formalism we may treat the fictitious gauge fields which arise from any arbitrary deformation of the crystal lattice. We find that the low energy electronic spectrum of bilayer graphene is dominated by the effect of trigonal warping creating a complex structure of four Dirac cones in each valley. Due to the small momentum scale separating these Dirac cones we show that the application of very small strains to the lattice dramatically modifies its structure, needing only a uniaxial extension of 0.5% to leave the electronic spectrum reconstructed as two Dirac cones. We find that this strain driven transition creates observable consequences in the conductivity and shot noise of the bilayer graphene in the ballistic transport regime. The conductivity will contain anomalies due to the Lifshitz transition whose position in energy increases at the strain in the device is increased. The characteristic pseudo diffusive Fano factor of $F = 1/3$ remains intact both with the inclusion of trigonal warping and the application of strain, furthermore the application of strain acts to

increase the energy range that the pseudo diffusive value of the Fano factor is observed making strained devices an attractive proposition for observing this physical regime in experiment. Due to the small strain needed to create this effects this will likely be the important regime to consider for all suspended bilayer graphene devices.

Additionally within this formalism we have studied the fictitious gauge field in MoS₂ for arbitrary deformations of the lattice. To do this we introduced effective theories of the electronic and vibrational properties of MoS₂ and then as an application of this formalism we considered the strength of the electron-vibron coupling that will arise in suspended MoS₂ devices. We find that the electron-vibron coupling constants are highly sample specific, with the largest coupling being with the longitudinal stretching mode. While the strength of the coupling of this mode is lower than seen in similar suspended carbon based nanostructures due to the larger atomic masses of the atoms which comprise the lattice, MoS₂ does exhibit electronic transport regimes dominated by localised impurity states.

6.1 Further work

The formalism presented in this thesis for the fictitious gauge fields created by arbitrary deformations of the lattice builds the ground work for a large body of possible extensions of this work. While in chapter 5 we found that electron-vibron coupling in MoS₂ is weaker than what is expected in carbon nanotubes we have not fully addressed the role of spin orbit coupling. The strong spin orbit coupling found in the transition metal dichalcogenides will be the feature that gives them a unique role in electromechanical devices.

One fruitful avenue for future work is nano electromechanical systems, such as nano mechanical resonators which are activated by a capacitive coupling to the back gate. The most interesting scenario in these devices is when they are resonated near their resonant frequency giving rise to strong non-linear mechanical motion. Analysing the effect on the current in a resonantly driven devices would allow for the study of how these mechanical deformations affect the electronic transport through the device, but of even greater interest will be the modification of the mechanical properties of the membrane by electrical current driven through the system. One aspect that was left out of our study of the electron-vibron coupling in MoS₂ was a calculation of the conductance through a sample. This would open up the possibility of looking at the effect of dif-

ferent relaxation times of vibrons. Another related route to studying novel effects in these devices would be to study the driven Anderson-Holstein model using mechanical resonators to drive controllable populations of vibrons in the system and to study their non-equilibrium population. To help explore systems with strong electron-vibron coupling it will be interesting to look at buckling of nano mechanical systems as this is a promising route toward increasing electron-vibron effects due to a softening of the fundamental mode of the device near the mechanical instability to the buckled phase.

The route to the most dramatic effects in electrical transport due to strain is the creation of pseudo magnetic fields, which has not been discussed at much length in this work. It would be interesting to explore this area in more detail, particularly focusing on differences between a pseudo magnetic field and a real magnetic field. In fact a homogenous pseudo magnetic field will have equal but opposite strength in different valleys, as it does not break time reversal symmetry. This leads to different structures in the Landau levels compared to samples in the presence of real magnetic fields. For instance the effect on the valley space of the 8 component spinor due to sublattice, valley and spin degrees of freedom will be distinct from the real magnetic field case, and one might expect electrons in partially filled Landau level too order differently under real or pseudo magnetic fields.

The interplay between real and pseudo magnetic fields in devices will lead to interesting physics. Firstly, if the real magnetic field is equal in magnitude to the strain induced pseudo magnetic field, in one valley the two will add up, leading the system in the quantum Hall regime while in the other valley the two would cancel, producing an ordinary Fermi liquid of Dirac quasiparticles. While the Hall conductivity will not be topologically protected against valley scattering this system will have a broken valley symmetry with promising valleytronic applications. Indeed, more exotic samples could be imagined such that a pseudo magnetic field is created locally, leading to regions only under the influence of the real magnetic field and others feeling the combined real and pseudo magnetic fields. In this setup there will be values for the magnitude of the real and pseudo magnetic field at which interesting physics can arise at the boundary between these regions. For instance differing interactions may drive spin and valley textures which must smoothly turn into one another over the boundary between the strained and non strained region.

7

Appendix A: Full Form of Fictitious Gauges fields in MoS₂ to Second Order

For completeness here we present all the corrections to the electronic Hamiltonian due to arbitrary deformations of the lattice in the three band model used in Eq(5.4). The corrections take the form

$$\delta H^{(\tau)} = \begin{pmatrix} \mathcal{F}_\gamma + D^{(s)} + \frac{1}{2}D^{(a2)} & \mathcal{F}_{\text{BS}}^{(\tau)\dagger} & -D^{(a1)} \\ \mathcal{F}_{\text{BS}}^{(\tau)} & D^{(s)} - D^{(a2)} & \mathcal{F}_{\text{BA}}^{(\tau)} \\ -D^{(a1)} & \mathcal{F}_{\text{BA}}^{(\tau)} & \mathcal{F}_\gamma + D^{(s)} + \frac{1}{2}D^{(a2)} \end{pmatrix} \quad (7.1)$$

We notice that, with the inclusion of these corrections, the anti-symmetric band can couple to the both the other two bands which we focus on in the main text. The gauge fields are

$$\begin{aligned}
\mathcal{F}_{\text{BS}}^{(\tau)} = & \frac{3a}{\bar{c}} \frac{\partial t}{\partial \bar{c}} \left[\frac{3}{2} (u_y^{(a2)} - i\tau u_x^{(a2)}) + \frac{a}{4} (2\partial_x u_x^{(s)} - \frac{1}{2} \partial_x u_x^{(a2)} - 2\partial_y u_y^{(s)} + \frac{1}{2} \partial_y u_y^{(a2)}) \right. \\
& + i\tau (2\partial_x u_y^{(s)} - \frac{1}{2} \partial_x u_y^{(a2)} + 2\partial_y u_x^{(s)} - \frac{1}{2} \partial_y u_x^{(a2)}) + \frac{c}{4} (\partial_y h^{(a1)} - i\tau \partial_x h^{(a1)}) \\
& + \frac{3a}{16} ((\partial_x u_x^{(a1)})^2 + (\partial_y u_y^{(a1)})^2 + (\partial_y u_x^{(a1)})^2 + (\partial_x u_y^{(a1)})^2 - 2i\partial_y u_x^{(a1)} \partial_x u_x^{(a1)} - 2i\partial_y u_x^{(a1)} \partial_y u_y^{(a1)}) \\
& + \frac{3a}{64} (\partial_y u_x^{(a2)} - 4\partial_y u_x^{(s)} - i\partial_x u_x^{(a2)} + 4i\partial_x u_x^{(s)})^2 + \frac{3a}{64} (\partial_y u_y^{(a2)} - 4\partial_y u_y^{(s)} - i\partial_x u_y^{(a2)} + 4i\partial_x u_y^{(s)})^2 \\
& + \frac{3a}{64} (2\partial_y h^{(a1)} + i\partial_y h^{(a2)} - 4i\partial_y h^{(s)} - 2i\partial_x h^{(a1)} + \partial_x h^{(a2)} - 4\partial_x h^{(s)}) (2\partial_y h^{(a1)} - i\partial_y h^{(a2)} + 4i\partial_y h^{(s)} + 2i\partial_x h^{(a1)} \\
& \left. - \partial_x h^{(a2)} + 4\partial_x h^{(s)}) \right] \quad (7.2)
\end{aligned}$$

and

$$\begin{aligned}
\mathcal{F}_{\text{BA}}^{(\tau)} = & \frac{3a}{\bar{c}} \frac{\partial t}{\partial \bar{c}} \left[(2u_y^{(a1)} - i\tau 2u_x^{(a1)}) + \frac{a}{4} (\partial_y u_y^{(a1)} - \partial_x u_x^{(a1)} + i\tau (\partial_y u_x^{(a1)} + \partial_x u_y^{(a1)})) \right. \\
& - \frac{c}{4} (\partial_y h^{(a2)} - i\tau \partial_x h^{(a2)} - 4\partial_y h^{(s)} + i\tau 4\partial_x h^{(s)}) + \frac{3a}{32} (\partial_x u_x^{(a1)} + i\tau \partial_y u_x^{(a1)}) (\partial_y u_x^{(a2)} - i\tau \partial_x u_x^{(a2)} - 4\partial_y u_x^{(s)} + i\tau 4\partial_x u_x^{(s)}) \\
& + \frac{3a}{32} (\partial_x u_y^{(a1)} + i\tau \partial_y u_y^{(a1)}) (\partial_y u_y^{(a2)} - i\tau \partial_x u_y^{(a2)} - 4\partial_y u_y^{(s)} + i\tau 4\partial_x u_y^{(s)}) \\
& \left. + \frac{3a}{16} (\partial_x h^{(a1)} + i\tau \partial_y h^{(a1)}) (\partial_y h^{(a2)} - i\tau \partial_x h^{(a2)} - 4\partial_y h^{(s)} + i\tau 4\partial_x h^{(s)}) \right]. \quad (7.3)
\end{aligned}$$

Additionally,

$$\mathcal{F}_\gamma = \frac{1}{2} \frac{\partial \gamma}{\partial c} \left[\frac{1}{c} \mathbf{u}^{(a1)2} + h^{(a1)} + \frac{1}{c} h^{(a1)2} \right] \quad (7.4)$$

and finally the deformation potentials remain unchanged from the form in the main text

$$D^{(\nu)} = g_2 \text{Tr}[u_{ij}^{(\nu)}] \quad (7.5)$$

where $\nu = s, a1, a2$ and the strain tensor is given by

$$u_{ij}^{(\nu)} = \frac{1}{2} (\partial_i u_j^{(\nu)} + \partial_j u_i^{(\nu)} + \partial_i h^{(\nu)} \partial_j h^{(\nu)}). \quad (7.6)$$